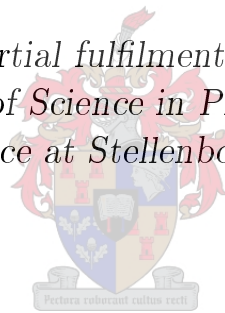# Fluorescence and self-absorption free excitation spectroscopy of carbon monoxide isotopomers in the vacuum ultraviolet

by

André de Bruyn

Thesis presented in partial fulfilment of the requirements for the degree of Master of Science in Physics in the Faculty of Natural Science at Stellenbosch University

Department of Physics
University of Stellenbosch
Private Bag X1, Matieland 7602, South Africa

Supervisors:

Dr. C.M. Steenkamp
Prof. E.G. Rhower
Dr. A. Du Plessis

March 2017

Declaration

By submitting this thesis electronically, I declare that the entirety of the work contained therein is my own, original work, that I am the sole author thereof (save to the extent explicitly otherwise stated), that reproduction and publication thereof by Stellenbosch University will not infringe any third party rights and that I have not previously in its entirety or in part submitted it for obtaining any qualification.

Date: .... March 2017 ....

Abstract

Fluorescence and self-absorption free excitation spectroscopy of carbon monoxide isotopomers in the vacuum ultraviolet

A. de Bruyn

Department of Physics
University of Stellenbosch
Private Bag X1, Matieland 7602, South Africa

Thesis: MSc (Phys)

December 2016

Carbon Monoxide (CO) is the most abundant heteronuclear diatomic molecule in the universe and has been of great interest in the fields of astrophysics and astronomy. CO is additionally, a prototype molecule for theoretical models. By using a supersonic free-jet expansion it is possible to conduct spectroscopy of this molecule under collision-free and low temperature conditions similar to that found in space. The radiation used in this study to conduct spectroscopy is tuneable coherent vacuum ultraviolet (VUV) light which is generated by four-wave sum frequency mixing in a magnesium vapour medium.

For the first time in our laboratory, the fluorescence of CO upon rovibronic excitation has been investigated using a scanning monochromator. Vibrationally resolved fluorescence spectra resulting from population of single rovibronic levels in the $A^1\Pi(v'=3,4)$ bands for $^{12}C^{16}O$ and the $A^1\Pi(v'=3)$ bands for $^{13}C^{16}O$, $^{12}C^{18}O$ were recorded. The theoretical models of Morse and Dunham were applied to calculate vibrational constants of the $X^1\Sigma^+(v''=0)$ state, Franck-Condon factors, r-centroid values and the r-centroid dependence of the electronic transition moments for the $A^1\Pi(v'=3,4) - X^1\Sigma^+(v''=0)$ bands for the different isotopomers.

Using the tuneable coherent VUV light it was possible to record the rotationally resolved excitation spectra for $X^1\Sigma^+(v''=0) - A^1\Pi(v'=3)$ and $X^1\Sigma^+(v''=0) - A^1\Pi(v'=4)$ bands of $^{12}C^{16}O$. In the high-resolution excitation spectra, several forbidden singlet-triplet rovibronic transitions of the $X^1\Sigma^+(v''=0) - a'^3\Sigma^+(v'=14)$ band were recorded.

ii

Two new measuring techniques were developed in this study. The first measuring technique allows for an accurate measurement of the amount of VUV light generated during excitation measurements. The second measuring technique allows for recording of self-absorption free rotationally resolved excitation measurements. These two techniques additionally resulted in a significant improvement in spectral resolution. Using the new measuring techniques it was possible to accurately determine the rotational temperature of the supersonic gas jet. Using the temperature, limiting values for the Mach number, gas flow speed and effective density in the supersonic gas were calculated.

Uittreksel

Fluoressensie en self-absorpsie-vrye opwekking spektroskopie van koolstofmonoksied isotopomere in die vakuum ultraviolet

("Fluorescence and self-absorption free excitation spectroscopy of carbon monoxide isotopomers in the vacuum ultraviolet")

A. de Bruyn

Fisika Departement
Universiteit van Stellenbosch
Privaatsak X1, Matieland 7602, Suid Afrika

Tesis: MSc (Phys)

Desember 2016

Koolstofmonoksied (CO) is die volopste heterokern diatomiese molekuul in die heelal en is van groot belang in die velde van astrofisika en sterrekunde. CO is daarbenewens 'n prototipe molekuul vir teoretiese modelle. Deur die gebruik van vrye supersoniese gasstraal is dit moontlik om spektroskopie van hierdie molekule uit te voer onder botsings vrye en lae temperatuur toestande soortgelyk aan die toestande in die ruimte. Die lig wat in hierdie studie gebruik word om spektroskopie uit te voer is afstembare koherente vakuum ultraviolet (VUV) lig wat gegenereer word deur vier-golf som-frekwensie vermenging in 'n magnesiumdamp medium.

Vir die eerste keer in ons laboratorium, is die fluoressensie van CO na rovibroniese opwekking ondersoek met behulp van 'n skanderende mono-kromator. Vibrasioneel-opgeloste fluoressensie spektra as gevolg van die bevolking van enkel rovibroniese vlakke in die $A^1\Pi(v' = 3, 4)$ bande van $^{12}C^{16}O$ en die $A^1\Pi(v' = 3)$ band van $^{13}C^{16}O$, $^{12}C^{18}O$ is opgeneem. Die teoretiese modelle van Morse en Dunham is toegepas om vibrasie konstantes van die $X^1\Sigma^+(v'' = 0)$ toestand, Franck-Condon faktore, r-swaartepunt waardes en die r-swaartepunt afhanklikheid van die elektroniese oorgangsmoment vir die $A^1\Pi(v' = 3, 4) - X^1\Sigma^+(v'' = 0)$ band van die verskillende isotopomere.

Die gebruik van afstembare koherente VUV lig het dit moontlik gemaak om die rotasioneel-opgeloste opwekkingspektra van die $X^1\Sigma^+(v'' = 0) - A^1\Pi(v' =$

3) en $X^1\Sigma^+(v''=0) - A^1\Pi(v'=4)$ bande van $^{12}C^{16}O$ te meet. In die hoë-resolusie opwekkingspektra is verskeie verbode singlet-triplet rovibroniese oorgange van die $X^1\Sigma^+(v''=0) - a'^3\Sigma^+(v'=14)$ band aangeteken.

Twee nuwe meettegnieke is in hierdie studie ontwikkel. Die eerste meettegniek laat toe dat die hoeveelheid VUV lig wat gegenereer word tydens die opneem van opwekkingspektra akkuraat gemeet word. Die tweede meettegniek maak laat die opname van self-absorpsie-vrye rotasioneel-opgeloste opwekkingspektra toe. Hierdie twee tegnieke het bykomend gelei tot 'n beduidende verbetering in die spektrale resolusie. Die gebruik van die nuwe meettegnieke het dit moontlik gemaak om die rotasionele temperatuur van die supersoniese gasstraal akkuraat te bepaal. Die temperatuur is gebruik om limiet waardes vir die Mach-getal, gas vloei spoed en effektiewe digtheid in die supersoniese gasstraal te bereken.

Acknowledgements

I would like to express my sincere gratitude to the following people and organisations:

Foremost, I would like to express my sincere gratitude to my supervisor Dr. Christine Steenkamp for all her patience, motivation, and support during this study. She always made herself available despite her busy schedule to guide me during challenging and difficult times. She allowed me to be creative and conduct independent research whilst steering me the right direction when needed. Your expertise and immense knowledge in this field have proved invaluable.

I would also like to acknowledge my co-supervisors Prof. Erich Rohwer and Dr. Anton du Plessis, for always being available for counsel during this thesis. Your encouragement, insightful comments, and thought-provoking questions were greatly appreciated.

A big thank you to Mr. Gerhard Louwrens and Mr. Laurence Ashworth whose input and incredible expertise in developing technical equipment needed for this study is greatly appreciated.

The CSIR National Laser Centre through the Rental Pool Programme provided financial support to this Project.

This work is based on the research supported in part by the National Research Foundation of South Africa (Grant specific unique reference number (UID) 85683).

To my colleagues at the Laser Research Institute of Stellenbosch, I would like to thank you for all the valuable discussions and input related to this study.

Thank you to my parents for their unvarying support for which I will forever be grateful. Thank you for all the sacrifices you have made to help me achieve my goals.

I thank God for providing me with strength and guidance to overcome the challenges I faced during this study.

Contents

List of Figures

List of Tables

Chapter 1

Introduction

1.1 Motivation

Carbon Monoxide (CO) is the second most abundant molecule in the universe and important in astrophysics and astronomy. VUV absorption lines of the CO in the interstellar space are observed in the spectra of the starlight which are recorded by satellite-based spectrographs. The data is used to map out gas clouds in the interstellar space and are relevant to models of star evolution. The weak spectral lines of forbidden transitions of $^{12}C^{16}O$ are of high importance to astronomy and astrophysics since these spectral lines do not saturate in astronomical observations [14]. Data on CO is also relevant to molecular physics, and CO is a prototype molecule, for which a numerical model has been developed. However, for a large number of the forbidden transitions experimental spectroscopic data is lacking [12].

The tuneable VUV laser source with narrow spectral bandwidth available in our laboratory allows for the forbidden transitions of CO to be recorded. Previous studies conducted by du Plessis et al. [15] and Dickenson et al. [16] in our laboratory, have successfully investigated and identified new forbidden transitions before the implementation of the current pump laser. The narrow spectral bandwidth of the light (high spectral resolution and high spectral brightness) allows for the detection of the fluorescence from weakly absorbing transitions. In addition, the pulsed nature of the sources makes selective detection of the forbidden transitions possible. Flow-cooling of CO gas in a supersonic jet makes it possible to do spectroscopy in conditions similar to conditions in space: collision-free and at temperatures down to a few Kelvin. The VUV laser source has been upgraded during the last few years using a new pump laser and now provides higher power. A VUV scanning monochromator has been added to the setup. With the addition of this new equipment, forbidden transitions that were previously inaccessible should be detectable. Previous studies conducted in our laboratory, by du Plessis et al. [17] and Steinmann et al. [18], have successfully investigated and measured for the first

1

time accurate wavelengths for rovibronic transitions for the $^{12}C^{17}O$ and $^{12}C^{18}O$ isotopomer species. A rovibronic level refers to a rotational energy level in a vibrational band of an electronic state. A rovibronic transition is a transition between two different rovibronic levels. The scanning monochromator that has been implemented during this study makes it possible for the first time in our laboratory to measure vibrationally resolved fluorescence spectra resulting from the excitation of a specific rovibronic transition of CO isotopomers. Implementation of the monochromator facilitates investigation of the effect of self-absorption, spectral filtering and spatial filtering on the resolution and quality of the measured excitation spectra.

1.2 Aims and objectives

This thesis is aimed at the investigation of the rovibronic excitation and the resulting vibrationally resolved fluorescence spectra of CO isotopomers in the VUV spectral region. This will include:

- Using theoretical models for diatomic molecules to determine transition probabilities.

  - Morse potential.
  - Dunham approximation.

- Measuring the fluorescence spectra of resulting from excitation of single rovibronic transitions for different CO isotopes.

  - Determine vibrational constants.
  - Determine coefficients related to the electronic transition moment.

- Measuring the rotationally resolved excitation spectra of CO for multiple vibronic bands and isotopes.

  - Measuring accurate wavelengths of forbidden triplet-singlet transitions.
  - Determining the rotational temperature and other parameters of the supersonic gas jet from the spectroscopic data.

- Development of two new measuring techniques.

  - Accurate measuring of the amount of VUV light available during rotational excitation measurements.
  - Measuring self-absorption free rotational excitation spectra.

Chapter 2

Theory

2.1 Vacuum ultraviolet light

VUV light can only be generated in a gaseous medium since a crystal medium would absorb the VUV light that is generated. Using a gaseous medium would only allow for odd-order nonlinear processes to occur like 1st and 3rd order processes. In our laboratory, VUV generation will be achieved by 3rd order processes (four-wave mixing).

VUV generation is a four-photon process. This process requires three input photons and will give a single photon back in the VUV range. There are two types of frequency generation processes that are of particular importance in this project. The first is the sum frequency (ω_S) in which two photons of frequency ω_1 are used in combination with a photon of frequency ω_2 as illustrated in Figure 2.1 (A). The second process that can occur is third harmonic generation (ω_T) in which three photons of frequency ω_1 are used as illustrated in Figure 2.1(B). The lowest line in Figure 2.1 represents the energy of the
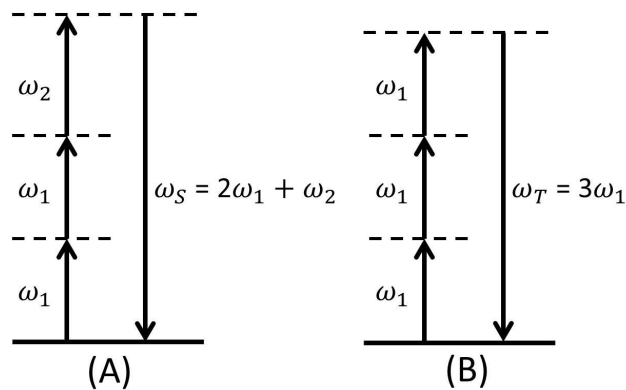
Figure 2.1: Energy level diagram for (A) sum frequency generation and (B) third harmonic generation.

atoms in the medium in their ground state. The energy levels are shown with dashed lines since they are not eigenstates of the material in which the radiation is generated but are instead levels of the combined material-photon beam system. In this respect, they are known as virtual levels as they do not accumulate population in these levels. Instead, one photon of frequency ω_2 and two photons of frequency ω_1 are annihilated, and one photon of frequency ω_S is simultaneously created for sum frequency generation. Similarly, for third harmonic generation, three photons of frequency ω_1 are destroyed and one photon of frequency ω_T is simultaneously created. The upward arrows correspond to the input fields that can drive the material system up in energy. The downward arrows corresponds to the generated field, which returns the material to the initial state.

The intensity of the sum frequency field $I_3(L)$ generated by two collinear laser beams at frequencies ω_1 and ω_2 in an isotropic medium is given by Equation (2.1.1) [19]. To be able to derive Equation (2.1.1) the following assumptions and approximations are made:

- Isotropic medium leading to $\chi^{(2)} = 0$;

- Parallel beams;

- Small signal $(I_3 \ll I_1)$;

- One photon absorption of ω_1, ω_2 and ω_3;

- Slowly varying envelope approximation;

- Medium with rectangular density profile of length L.

$$I_3(L) = \frac{144\pi^4 \omega_3^2}{n_2 n_1^2 n_3 c^4} L^2 \left| \chi^{(3)}(\omega_3, \omega_1, \omega_1, \omega_2) \right|^2 I_2(0) [I_1(0)]^2 F\left(\Delta\vec{k}, \Gamma_i, \Gamma_3\right),$$
(2.1.1)

where ω_3 is the sum frequency generated $(\omega_3 = \omega_s)$, n_i is the index of refraction for a given wavelength, $I_i(0)$ is the intensity of the specific wave at the beginning of the medium, $\chi^{(3)}(\omega_3, \omega_2, \omega_1, \omega_1)$ is the third order susceptibility of the non-linear medium and $F\left(\Delta\vec{k}, \Gamma_i, \Gamma_3\right)$ is the phase matching factor. The optical depth of the medium is given by Γ_i for ω_i (input frequency) and by Γ_3 for the output frequency ω_3. The wave vector mismatch between the incident and generated waves is given by $\Delta\vec{k}$, as will be discussed in Section 2.1.1.

2.1.1 Wave Vector

The wave vector $(\vec{k})$ is defined as a vector of which the magnitude is the wave number, $k = \frac{h\omega}{c} = \frac{2\pi}{\lambda}$. In a lossless isotropic medium like gas, the direction of the wave vector is precisely the direction of wave propagation. It is related

to the linear momentum of the photon, $p = \hbar k \Rightarrow k = \frac{p}{\hbar}$. The wave vector mismatch for third harmonic generation is a result of conservation of linear momentum and is given by:

$$\Delta\vec{k} = \vec{k}_1 + \vec{k}_1' + \vec{k}_1'' - \vec{k}_3 \qquad \text{where} \qquad k_i = \frac{n_i\omega_i}{c}, \qquad (2.1.2)$$

where $\vec{k}_3$ is the wave vector for the generated light, $\vec{k}_1$ is the wave vector for the incident light and n_i is the index of refraction of a medium for a wavelength ω_i. Under the plane wave approximation, the wave vectors have no angular spread and the condition $\Delta k = 0$ is illustrated in Figure 2.2 (A). However, once the light is focused, an angular spread of the wave vectors exists and the condition $\Delta\vec{k} = \vec{0}$ can also be achieved as illustrated in Figure 2.2(B). The wave vector
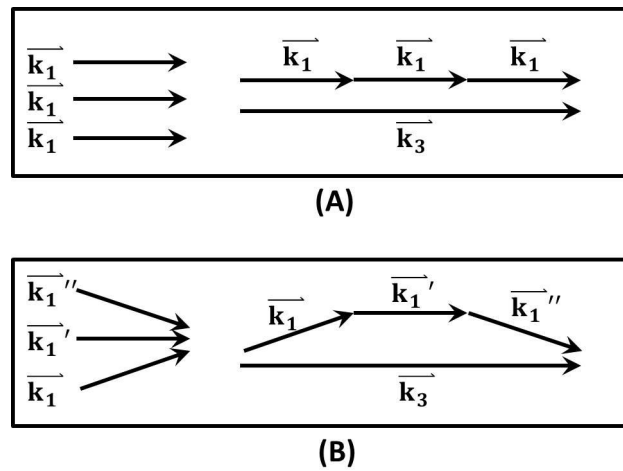
Figure 2.2: Wave vectors for (A) plane wave approximation and (B) Converging-beam (similar for diverging beam).

mismatch is the parameter that can be tuned to optimise the phase matching factor $F\left(\Delta\vec{k}, \Gamma_i, \Gamma_3\right)$.

2.1.2 Phase matching

Phase matching corresponds to the requirement for the conservation of linear momentum during the VUV generation. Phase matching will not only optimize the sum frequency generation but will also aid in suppressing the difference frequency generation. However, it can not always be used to suppress the third harmonic generation since the phase matching conditions for the sum and third harmonic generations are very similar. For parallel beams (meaning that the plane wave approximation is applied) and not absorption the phase

matching factor is given by:

$$I_3 = I_3^{max} \left[\frac{\sin\left(\Delta k L/2\right)}{\Delta k L/2} \right]^2, \tag{2.1.3}$$

thus for perfect phase matching it is required that $\Delta k = 0$ [20].

The phase matching factor for parallel beams (plane wave approximation) with one photon absorptions is given by [21]:

$$F\left(\Delta \vec{k}, \Gamma_i, \Gamma_3\right) = \frac{\exp\left(-\Gamma_i\right) + \exp\left(-\Gamma_3\right) - 2\exp\left(-\frac{\Gamma_3 - \Gamma_i}{2}\right)\cos\left(\Delta \vec{k} L\right)}{\left(\frac{\Gamma_3 - \Gamma_i}{2}\right)^2 + \left(\Delta \vec{k} L\right)^2}, \tag{2.1.4}$$

where $\Delta \vec{k}$ is the wave vector mismatch (Section 2.1.1), Γ_i is the optical depth of the medium for ω_i (input frequency) and Γ_3 is the optical depth for ω_3 (generated frequency). In the previous section it was established that one-photon resonance will be avoided resulting in the optical depth for the incident frequencies $\Gamma_i \approx 0$, therefore, yielding Equation (2.1.5). However, ω_3 often causes photon-ionisation (or auto-ionisation) of the magnesium which should not be ignored ($\Gamma_3 \neq 0$)[21]. Magnesium vapour provides both a large intrinsic third order nonlinear susceptibility as well as suitable two-photon resonances with low two-photon absorption coefficients for the generation of sum-frequencies in the vacuum ultraviolet. Additionally, the atomic energy levels of magnesium allowed for VUV light generation in the required wavelength region and was thus selected as the nonlinear medium.

$$F\left(\Delta k, \Gamma_i, \Gamma_3\right) \approx \frac{1 + \exp\left(-\Gamma_3\right) - 2\exp\left(-\frac{\Gamma_3}{2}\right)\cos\left(\Delta k L\right)}{\left(\frac{\Gamma_3 -}{2}\right)^2 + \left(\Delta k L\right)^2} \tag{2.1.5}$$

By plotting $F\left(\Delta k, \Gamma_i, \Gamma_3\right)$ for different values of the optical depth of Γ_3 (Figure 2.3), it can be seen that for perfect phase matching $\Delta k = 0$ is required. However, as the optical depth increases, the maximum value for $F\left(\Delta k, \Gamma_i, \Gamma_3\right)$ decreases and, the oscillations on both sides of the main peak decreases.

In this study, moderately focused laser beams were used to achieve higher intensities, therefore, the phase matching for a plane wave approximation can not be applied. To illustrate how a focused beam affects the phase matching we consider: a tightly focused laser beam, the Gaussian beam approximation and also assume an optically thin medium resulting in $\Gamma_3 \approx 0$ and $\Gamma_i \approx 0$. When a Gaussian beam is refracted by a lens, the Gaussian beam is transformed into another Gaussian beam which is characterized by a different set of parameters. These parameters are illustrated in Figure 2.4 where w_0 is the spot size, $\Theta = \lambda/\pi w_0$ is the angular divergence, $w(z) = w_0\left(1 + z^2/z_0^2\right)^{1/2}$ is the beam radius and the confocal parameter is given by $b = 2z_0 = kw_0^2$. In this study a
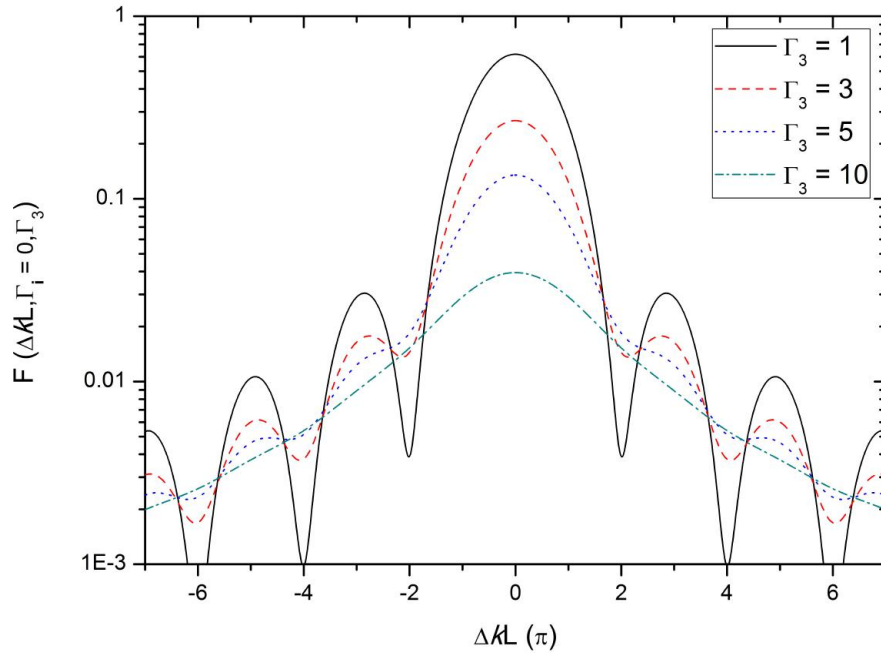
Figure 2.3: Phase matching curve at different optical depths (log scale on y-axis).

medium focus will be used. To investigated the effect that focusing the laser beams will have on the phase matching we consider the tightly focused laser beam approximation which does not take into account absorption. With this approximation it is expected that for optimal phase matching that the phase matching peak shifts to a positive vale for Δk.
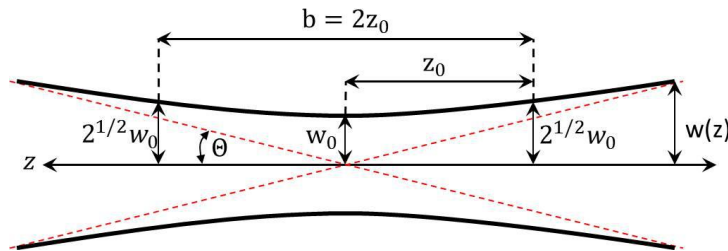
Figure 2.4: Gaussian beam representation.

The phase matching factor for a tightly focused laser beam for third harmonic generation is given by Equation (2.1.6) (see [22] for full derivation) with the tightly focus limit ($L \gg b$).

$$F\left(\Delta k, b/L\right) = 0 \qquad\qquad\qquad \text{for} \quad \Delta k \leq 0$$

$$F\left(\Delta k, b/L\right) = \frac{\pi}{4}\left(\frac{b}{L}\right)^2 (\Delta k b)^2\, e^{-\Delta k b} \qquad \text{for} \quad \Delta k > 0 \qquad\qquad (2.1.6)$$

Figure 2.5 is a plot of Equation (2.1.6) to illustrate the theoretical phase matching curve. The curve reaches its maximum when $\Delta kb \approx 2$, while at $\Delta k = 0$ the third harmonic generations is zero. The shift of the peak to $\Delta k > 0$ can be explained by the phase change which the light undergoes when passing through the focus. The phase change experienced by the incident light and the generated light are not the same. Therefore, the wave vector mismatch for perfect phase matching must be $\Delta kb \approx 2$ to compensate for the phase change caused by the focus.
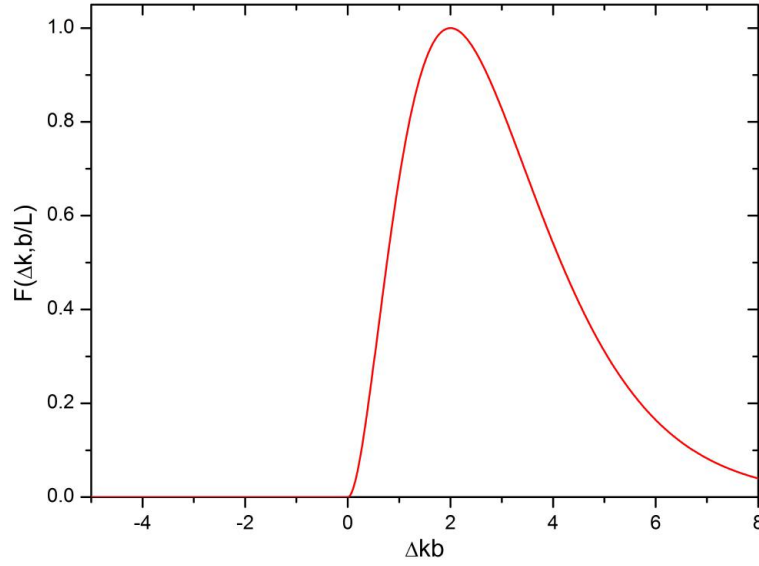
Figure 2.5: Phase matching curve for tightly focused Gaussian beam (y-axis normalized).

2.1.3   Susceptibility

The third order susceptibility for sum frequency generation is given by Equation (2.1.7) (for full expansion see Equation 3.7.11 in [20]). The third order susceptibility was derived by [20] using the density matrix formalism and intrinsic permutation operator.

$$\chi^{(3)}_{kjih}\left(\omega_3, \omega_2, \omega_1, \omega_1\right) = \frac{N}{\hbar^3}\mathcal{P}_I \sum_{gmnv} \rho^{(0)}_{gg} \qquad (2.1.7)$$

$$\left[\frac{\mu^k_{gv}\mu^j_{vn}\mu^i_{nm}\mu^h_{mg}}{\left[(\omega_{vg} - \omega_1 - \omega_1 - \omega_2) - i\gamma_{vg}\right]\left[(\omega_{ng} - \omega_1 - \omega_1) - i\gamma_{ng}\right]\left[(\omega_{mg} - \omega_1) - i\gamma_{mg}\right]} + \dots \right]$$

Where N is the number of atoms/molecules per unit volume and the subscripts *kjih* define the transversal polarisation of each wave with frequency ω_n. The intrinsic permutation symmetry operator is given by $\mathcal{P}_I$ which indicates the expression that

follows must be averaged over all possible permutations of index pairs of ω_1,h and ω_1,i and ω_2,j. The subscripts *gmnv* define the energy level of the atoms in the non-linear medium. The dipole transition moment is given by μ_{vn} and the decay rate is given by γ_{vn} for a transition from v to n. The population density of state g is given by $\rho_{gg}^{(0)}$. It can be observed from this equation that there are multiple resonance structures for $\chi_{kjih}^{(3)}(\omega_3, \omega_2, \omega_1, \omega_1)$ that can be realised by choosing the incident frequencies ω_1 and ω_2 in such a way that the real part of one of the factors in the denominator tends to zero. We will assume that state g is the ground state of magnesium. The
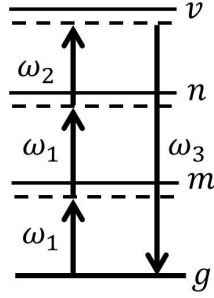
Figure 2.6: Energy diagram of Equation (2.1.7) showing states m,n and v close to resonance.

sum over the different ground states $(\sum_g)$ can be ignored since even at the typical temperature of $760\,^\circ$C approximately all of the magnesium electrons will be in their lowest atomic energy state. If g is the ground state the additional terms (indicated by $\cdots$ in Equation (2.1.7), called counter-rotating terms) can be ignored, since these terms can never be resonant. The remaining term in Equation (2.1.7) is illustrated by the energy diagram in Figure 2.6.

It is important to note that the sum frequency illustrated in Figure 2.7 is not the only third order non-linear process that can occur. The following processes can also occur: third harmonic generation ($3\omega_1$ and $3\omega_2$) and difference frequency generation ($3\omega_1 - \omega_2$ and $2\omega_2 - \omega_1$) as illustrated in Figure 2.7. This raises the question of how to optimize the sum frequency generation and how to suppress the unwanted processes? The first step to optimize the sum frequency generation would be to consider resonance enhancement of $\chi^{(3)}(\omega_3, \omega_2, \omega_1, \omega_2)$. The three possible resonance conditions are illustrated in Figure 2.8, where (A) is one-photon resonance of ω_1 (or ω_2), (B) is two-photon resonance of ω_1 and (C) three-photon resonance. All of these resonance conditions are equally efficient in increasing the value of $\chi^{(3)}(\omega_3, \omega_2, \omega_1, \omega_2)$. However, when considering the one-photon resonance of ω_1 and the three-photon resonance of ω_1, the incident field at ω_1 and ω_s fields will experience linear absorption respectively. This however, is not true for the two-photon resonance which can only cause non-linear two-photon absorption of ω_1, which is much weaker than one-photon absorption. When using the two-photon resonance to enhance $\chi^{(3)}(\omega_3, \omega_2, \omega_1, \omega_2)$, the frequency of ω_1 (fundamental) is selected to be $2\omega_1 = \omega_{ng}$. In this study since magnesium was used, the atomic transition for two-photon resonance is from $3s^2$ (ground state) to the $3s3d$ state. The two-photon resonance does not only increase
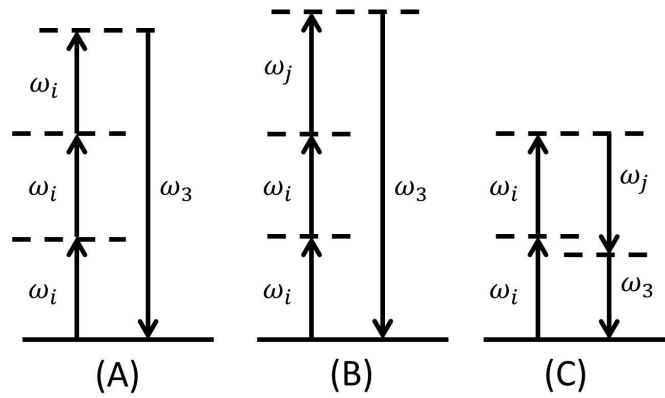
Figure 2.7: Energy diagrams for (A) third harmonic generation, (B) sum frequency generation and (C) difference frequency generation. Broken lines are virtual states

the sum frequency generation but also third harmonic generation of ω_1 and the difference frequency generation $2\omega_1 - \omega_2 = \omega_3$. However, by introducing polarization (of the incident beam) to the system it will be possible to suppress one of these processes. The third harmonic generation will be suppressed when the incident beams of
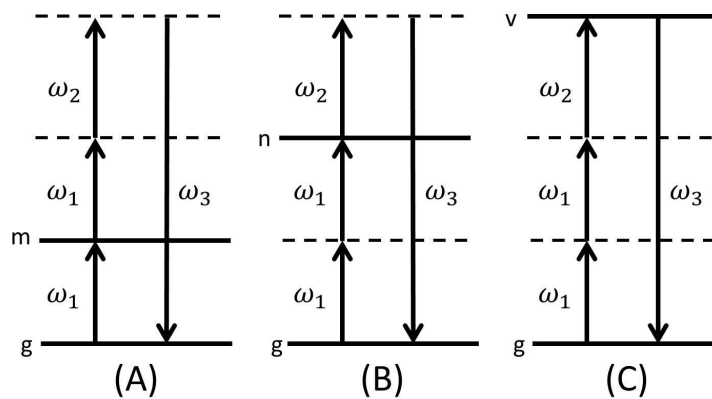
Figure 2.8: Diagram of photon enhancement (A) one-photon resonance, (B) two-photon resonance and (C) three-photon resonance.

ω_1 and ω_2 are polarized circularly in opposite directions, as a result of the quantum mechanical angular momentum selection rules (Equation (2.1.8)) [22].

For sum frequency of different frequency :
$$2\Delta m_1 + \Delta m_2 + \Delta m_3 = 0, \tag{2.1.8}$$

for third harmonic :
$$3\Delta m_1 + \Delta m_3 = 0, \tag{2.1.9}$$

where Δm_i is the change in the magnetic quantum number relating to an electric dipole moment $(\mu_{ab}^j(\omega_i))$. If the two incident laser beams are polarized circularly in opposite directions, then Δm_1 and Δm_2 have values of $+1$ and -1 respectively (or vice versa depending on their respective polarization directions). From Equation (2.1.9) it is clear that the third harmonic generation $(3\omega_1)$ is not allowed since it will require $\Delta m_3 = \pm 3$, which is impossible as a photon can not carry an angular momentum larger than 1. It is also clear from Equation (2.1.8) that sum frequency or different frequency generation are allowed since in that case $\Delta m_3 = \pm 2 \mp 1 = \pm 1$. The use of polarisation facilitates the suppression of the third harmonic generation $(3\omega_1)$ but does not influence the sum frequency generation or the difference frequency generation.

2.2 Diatomic molecules

There are two types of diatomic molecules that exist, homonuclear diatomic molecules which consist of two atoms of the same element (e.g. oxygen) and heteronuclear diatomic molecules which consist of two atoms of different elements (e.g. CO). In this study, carbon monoxide was investigated which is a heteronuclear diatomic molecule. The molecular geometry of diatomic molecules are represented by linear geometry as can be observed in Figure 2.9.
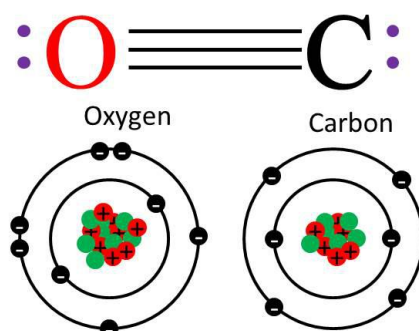
Figure 2.9: Molecular geometry of CO.

Oxygen and carbon have a total number of 10 electrons in the valence shell (Figure 2.9), where oxygen has an electron configuration of $1s^2 2s^2 2p^4$ and carbon has an electron configuration of the form $1s^2 2s^2 2p^2$. The triple bond formed between the oxygen and carbon atoms consist of 6 shared electrons in three bonding molecular orbitals. Where 4 electrons from an oxygen atom and 2 electrons from the carbon atom are utilized, thus leading to one of the bonding orbitals to be occupied by two electrons from oxygen creating a dipolar bond.

2.2.1 Vibrational and rotational structure

The energy of a molecule in a fixed electronic state can be described by vibrational and rotational energy. Where vibrational energy for a diatomic molecule is due to the attraction and repulsion between the individual atoms, whilst the rotational energy is the rotation of the molecule around the mass center point of the molecule. A molecule in a vibrational and rotational energy state can transition to a new vibrational, rotational or vibrational and rotational energy state if energy is introduced to the system which corresponds to a specific frequency (resonant frequency) of the molecule. If the energy introduced to the system does not correspond to a specific frequency of the molecule, the energy will not affect the system. These energy states are known as the vibrational and rotational energy levels of the molecule. The separation between vibrational levels is considerably larger than that of the rotational levels. For example the ground state $X^1\Sigma^+$ of CO the $v'' = 0 \rightarrow v'' = 1$ separation is $2143.24\,\mathrm{cm}^{-1}$ (δE_v in diagram) and the $v'' = 0, J'' = 0 \rightarrow v'' = 0, J'' = 1$ separation is $3.85\,\mathrm{cm}^{-1}$ (δE_J in diagram). The energy diagram for the diatomic molecule CO
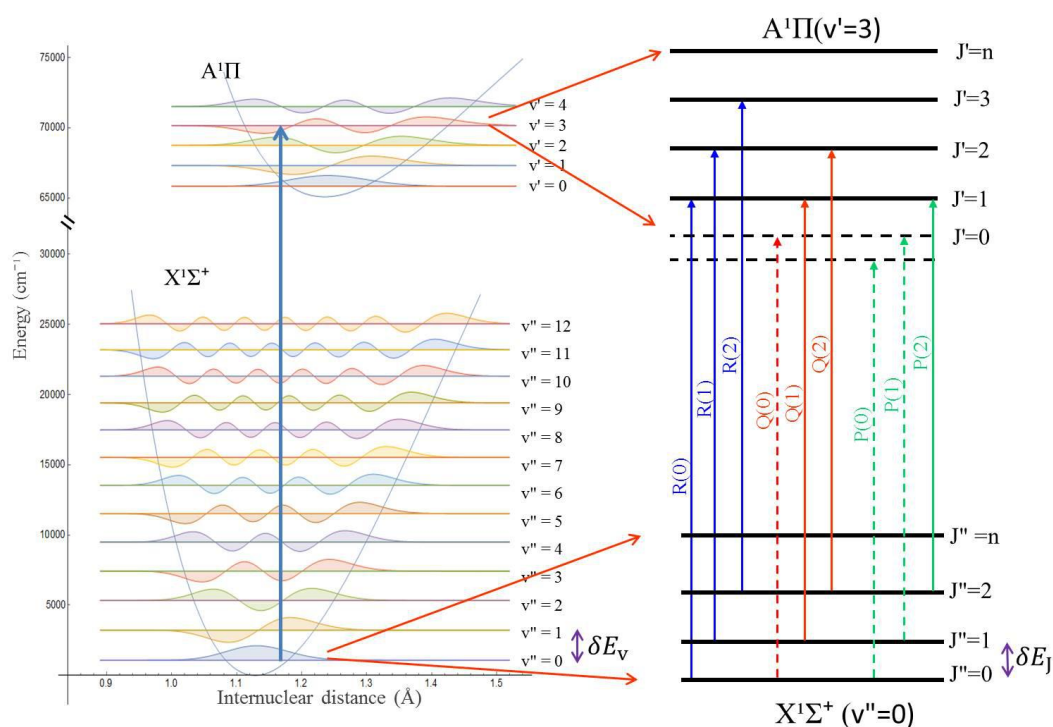
Figure 2.10: Energy diagram of CO for $X^1\Sigma^+$ and $A^1\Pi$ potentials.

can be observed in Figure 2.10, where it is illustrated that for a given vibrational level, multiple rotational levels exists.

2.2.1.1 Selection rules

Electronic excitation or de-excitation between different electronic states are governed by the following selection rule:

$$\triangle S = S' - S'' = 0, \tag{2.2.1}$$

which states that the electronic excitation or de-excitation between different electronic states must have the same spin quantum number S (given by the superscript $A^1\Pi$), thus only singlet-singlet, doublet-doublet or triplet-triplet transitions are allowed. No selection rules for transitions between states of different electronic states for a diatomic molecule exist. However, the transition probability is given by the Franck-Condon factors (FCF's) in Section 2.2.4.1. It will be shown in Section 4.4 that under our experimental conditions CO does not obey Kasha's rule, which states that if a molecule is in an excited vibrational state, that the molecule will first relax to the lowest vibrational level ($v = 0$) in the same potential before undergoing an electronic transition to a different potential.

The selection rules for rotational excitation or de-excitation between different electronic states for an electric dipole are rigorously governed by the total angular momentum quantum number:

$$\triangle J = J' - J'' = 0, \pm 1 \quad \text{with} \quad J' = 0 \nrightarrow J'' = 0, \tag{2.2.2}$$

where J'' is the rotational quantum number in the ground electronic state ($X^1\Sigma^+$), J' is the rotational quantum number in the excited electronic state ($A^1\Pi$). The selection rules given by Equation (2.2.2) states that the allowed rotational transitions must have a change in total angular momentum quantum number 1,-1 or 0 with the constraint that when $J'' = 0$ then $J' \neq 0$ [23]. These selection rules are also known as the P, Q and R branches for rotational lines, where for a rovibronic excitation:

$$\begin{aligned}
P(J'') \quad &\text{branch} \Rightarrow \triangle J = J' - J'' = -1, \\
Q(J'') \quad &\text{branch} \Rightarrow \triangle J = J' - J'' = 0 \quad \text{with} \quad J' = 0 \nrightarrow J'' = 0, \\
R(J'') \quad &\text{branch} \Rightarrow \triangle J = J' - J'' = 1.
\end{aligned} \tag{2.2.3}$$

From the constraints on the selection rules it is clear that $P(0)$, $P(1)$ and $Q(0)$ can not occur. The transition $P(0)$ can not occur as the $A^1\Pi(v = 0, J = -1)$ level does not exists (Figure 2.10). In this study, the electronic transitions between $X^1\Sigma^+ - A^1\Pi$ will be investigated, this will additionally add a restriction to the allowed transition that can occur as the $A^1\Pi$ electronic state is known as a Π state. These states (Π) have an angular momentum vector of $\Lambda = 1$, since the $A^1\Pi$ electronic state has an angular momentum vector of $\Lambda = 1$ that results in the rotational levels $J = 1, 2, 3, ...(J \geq \Lambda)$. The $A^1\Pi$ electronic state does not contain $J = 0$ rotational level thus $P(1)$ transition is not allowed and in addition leads to the $Q(0)$ transitions being forbidden by two different selection rules [24].

In this study, rotational de-excitation was also investigated. Once a molecule is excited to a rovibronic state in an excited electronic state it will de-excite to a specific rovibronic state of the electronic ground state. The same selection rules will apply to these molecules which undergo the de-excitation. For the rotational de-excitation

the P, Q and R notations will also be used, thus if a rotational excitation occurs, the molecule in the excited state will be in $J' = n$ rotational excited state, this molecule can then de-excite to $J'' = n-1$, $J'' = n$ or $J'' = n+1$ rotational levels in the ground state. If the molecule de-excites from $J' = n$ to $J'' = n-1$ rotational level it will be denoted by $R(n)$, a molecule which de-excites from $J' = n$ to $J'' = n$ rotational level will be denoted by $Q(n)$ and, a molecule which de-excites from $J' = n$ to $J'' = n+1$ rotational level it will be denoted by $P(n)$.

Similar to the FCF for vibronic transitions, an expression for the transition probability of rovibronic transitions known as the Hönl London factors exist. The Hönl London factors are dependent on the total angular momentum vector $(\Delta\Lambda = \Lambda' - \Lambda'')$ thus making it dependent on the type of electronic transition which is occurring. In this study, the electronic transition $X^1\Sigma^+ - A^1\Pi$ will be investigated leading to $\Delta\Lambda = 1$ and the following Hönl London factors [10]:

$$
\begin{aligned}
S_J^R &= \frac{(J''+2+\Lambda'')(J''+1+\Lambda'')}{4(J''+1)}, \\
S_J^Q &= \frac{(J''+1+\Lambda'')(J''-\Lambda'')(2J''+1)}{4J''(J''+1)}, \\
S_J^P &= \frac{(J''-1-\Lambda'')(J''-\Lambda'')}{4J''}.
\end{aligned}
\tag{2.2.4}
$$

Where the superscript R, Q and P are the rotational branches for which the particular expression holds, J'' is the rotational quantum number in the ground state and Λ'' is the angular momentum vector for the ground state. In the following section, it will be illustrated how Equation (2.2.4) can be utilised in determining the relative population distribution for the different rotational branches.

2.2.1.2 Population distribution

Under the approximation that the laser-induced fluorescence (LIF) excitation is equivalent to the absorption by the molecule in terms of the relative intensities of different rovibronic transitions $(I_{Abs} \propto I_{LIF})$, the proportional population distribution for the individual rovibronic transitions can be given by [25]:

$$
N^i(v" = 0, J") \propto \frac{I_{LIF}^i(J', J'')g_{J''}}{S_J^i},
\tag{2.2.5}
$$

where $N^i(v" = 0, J")$ is the population distribution, i indicates the specific rotational branch $(R, Q$ or $P)$, S_J^i is the Hönl London factor, the laser-induced fluorescence intensity is given by $I_{LIF}^i(J', J'')$ and $g_{J''}$ is the degeneracy of the lower state $(X^1\Sigma^+ \Rightarrow g_{J''} = 2J''+1)$. Using the Hönl London factors given by Equation (2.2.4) it is possible to determine the relative population distribution for the

individual rotational branches:

$$N^R(v" = 0, J") \propto 4\frac{I^R_{LIF}(J', J'')(2J'' + 1)}{(J'' + 2)},$$
$$N^Q(v" = 0, J") \propto 4I^Q_{LIF}(J', J''), \qquad\qquad (2.2.6)$$
$$N^P(v" = 0, J") \propto 4\frac{I^P_{LIF}(J', J'')(2J'' + 1)}{J'' - 1}.$$

With Equation (2.2.6) it is possible to determine the relative population distributions for the individual rotational branches by measuring the LIF which will be done in this study. Under the condition of thermal equilibrium it is possible to relate the relative population distributions given by Equation (2.2.6) to the Boltzmann distribution for rotational lines given by:

$$N_{J''} = g_{J''}N_0 e^{-\frac{E_{J''}}{kT_{rot}}} \implies \ln\left(\frac{N_{J''}}{g_{J''}N_0}\right) = \frac{-1}{T_{rot}}\frac{E_{J''}}{k}, \qquad (2.2.7)$$

where $N_{J''}$ is the population of the rotational state J'', N_0 is the total number of particles, $g_{J''}$ is the degeneracy of the lower state ($X^1\Sigma^+ \Rightarrow g_{J''} = 2J'' + 1$), $E_{J''}$ is the energy for the rotational state J'' measured relative to the ground state ($X^1\Sigma^+(v = n, J = 0)$), the Boltzmann constant is given by k and T_{rot} denotes the rotational temperature. In this study, the Boltzmann distribution will be used to determine the rotational temperature (T_{rot}) after the population distribution for the rotational lines are determined by using Equation (2.2.6).

Using Equation (2.2.7) it is possible to investigate the impact that the rotational temperature has on the population distribution (Figure 2.11). From Figure 2.11 it
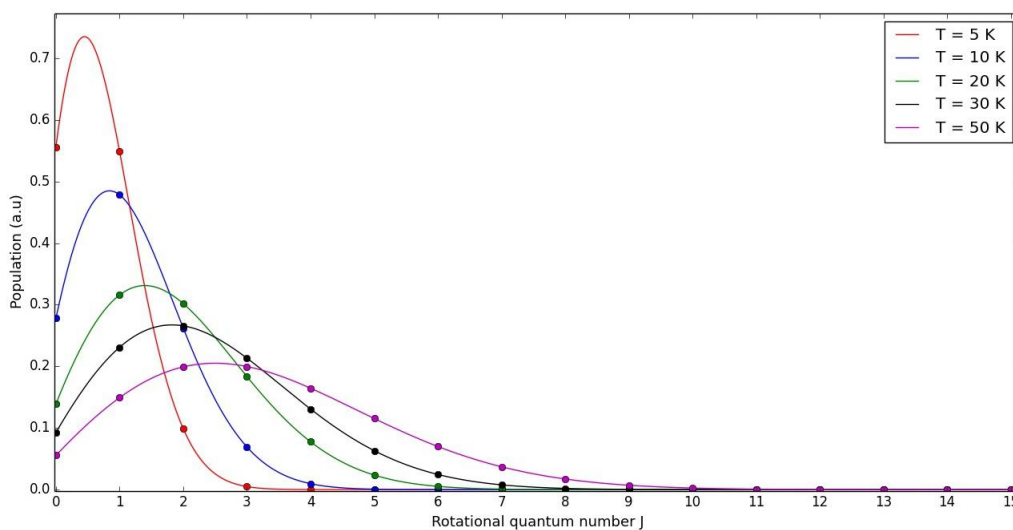
Figure 2.11: Population distribution given by the Boltzmann equation for different rotational temperatures.

can be observed that for low a rotational temperature (5 K) that only the first two

rotational levels are populated and that for a higher rotational temperature ($50\,\mathrm{K}$) the population is distributed from the 0th rotational level to the 9th rotational level with the highest population being at the 2nd and 3rd rotational levels.

2.2.2 Morse Potential

The Morse potential is an approximation for the anharmonic potential for diatomic molecules, therefore it is useful to use Morse potential to approximate the interaction between C and O in CO which is a diatomic molecule. The Morse potential was first proposed in 1929 by Philip M. Morse as an analytical solution to obtain wave function by solving the Schroedinger equation for a diatomic molecule [26]. Many methods exist for approximating anharmonic molecules, however, most of these methods do not analytically solve for the wave functions of these diatomic molecules. The Morse potential was used in this study as it is a reasonable approximation to the vibrational wave functions for low vibrational quantum numbers ($v \leq 0$). The Morse potential also requires considerably less computational power compared to other approximations for diatomic molecules like the Rydberg Klein Rees (RKR) which does not give an analytical solution but a numerical solution to the vibrational wave functions. In Section 2.2.2.3 it will be observed that when substituting the Morse potential into the Schödinger equation an analytical solution for the vibrational energy levels and the vibronic wave functions can be found. The Schödinger equation is given by:

$$\frac{\partial^2 \psi}{\partial x^2} + \frac{\partial^2 \psi}{\partial y^2} + \frac{\partial^2 \psi}{\partial z^2} + \frac{8\pi^2 m}{h^2}\left(E - V\right)\psi = 0. \tag{2.2.8}$$

Where h is Planck's constant, m is the mass of the molecule, the potential energy is given by V and the total energy is given by E.[27]

2.2.2.1 Potential

The simplest possible assumption for a molecule is that it is harmonic. In classical mechanics, the harmonic oscillator potential energy is given by:

$$V\left(r\right) = \frac{1}{2}k(r_e - r)^2, \tag{2.2.9}$$

where r_e is the equilibrium bond length and k is the force constant for the potential. This is however, not a good approximation for a diatomic molecule since it's potential energy is anharmonic [27]. A better approximation for an anharmonic potential is given by:

$$V\left(r\right) = f\left(r - r_e\right)^2 - g\left(r - r_e\right)^3 + j\left(r - r_e\right)^4 + \cdots, \tag{2.2.10}$$

where f, g and j are constants of the potential on condition that $f \gg g \gg j$. However, Equation (2.2.10) can not represent the whole potential as it can only approximate the potential for low values of $(r - r_e)$.

This fact led scientists like Morse to investigate different potentials to solve for the anharmonic potential. One of the key factors contributing to the Morse potential being widely used in physics and chemistry is the exact treatment of the mathematics.

The only approximation or assumption that is made is about the potential which will be explained in the following sections [27]. The Morse potential is given by:

$$V\left(r\right) = D_e \left(1 - e^{-\beta(r-r_e)}\right)^2,\tag{2.2.11}$$

where D_e (unit cm^{-1}) refers to the well depth (dissociation energy) illustrated in Figure 2.12. The equilibrium bond length is given by r_e (unit Å) and β (unit Å^{-1}) is related to the range of the potential. The dissociation energy is the energy difference between the lowest point in the potential (i.e the turning point energy) and the value that $V\left(r\right)$ has when $r \to \infty$ [27]. The dissociation energy and range are related to
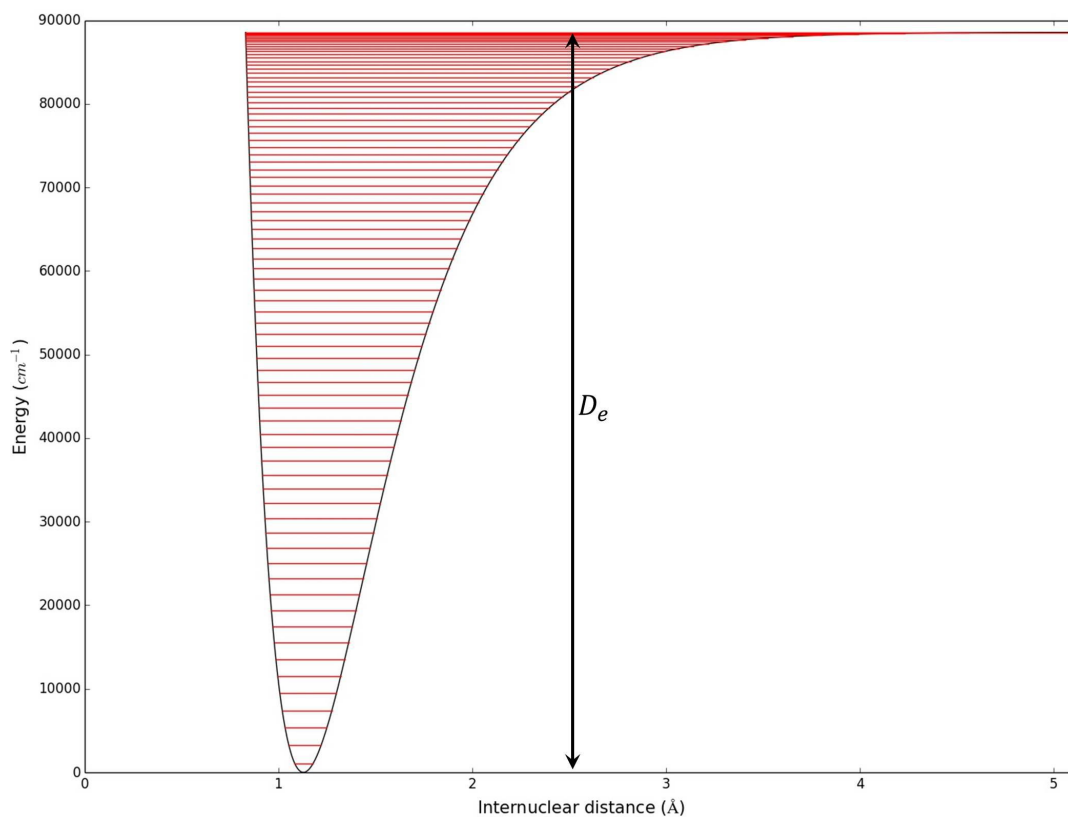
Figure 2.12: Potential for the $X^1\Sigma^+$ of ^{12}C^{16}O with corresponding vibration levels indicated in red (own calculation).

the vibrational constant for the Morse potential and are given by:

$$D_e = \frac{\omega_e^2}{4\omega_e x_e} \quad \text{and} \quad \beta = \omega_e \sqrt{\frac{2\pi^2 c \mu}{D_e h}},\tag{2.2.12}$$

where ω_e (unit cm^{-1}) is the harmonic vibrational constant, $\omega_e x_e$(unit cm^{-1}) is the anharmonic vibrational constant, β related to the range of the potential and the reduced mass given by $\mu = \frac{m_1 m_2}{m_1+m_2}$.

2.2.2.2 Vibrational energy

The corresponding energy values (eigenvalue coefficients for the wave function) of the anharmonic oscillator can be determined by substituting Equation (2.2.11) into the Schödinger Equation (2.2.8) and were found to be:

$$E(n) = w_e \left(\frac{1}{2} + n \right) - w_e x_e \left(\frac{1}{2} + n \right)^2, \qquad (2.2.13)$$

where n denotes vibrational quantum number, ω_e and $\omega_e \chi_e$ are the first and second anharmonic constants respectively. The relation between the $\omega_e, \omega_e \chi_e$ and D_e, β for the Morse potential is given by:

$$\omega_e = \beta \sqrt{\frac{D_e h}{2\pi^2 c \mu}} \quad \text{and} \quad \omega_e \chi_e = \frac{h \beta^2}{c 8 \pi^2 \mu} \quad \text{with} \quad \mu = \frac{m_1 m_2}{m_1 + m_2}. \qquad (2.2.14)$$

The vibrational energies for Morse potential is given by:

$$E(n) = \beta \sqrt{\frac{D_e h}{2\pi^2 c \mu}} \left(\frac{1}{2} + n \right) - \frac{h \beta^2}{c 8 \pi^2 \mu} \left(\frac{1}{2} + n \right)^2, \qquad (2.2.15)$$

where c is the speed of light in a vacuum and μ is the reduced mass. Since the dissociation energy occurs at a specific energy this leads to the number of vibrational levels to be bound and is given by [27]:

$$v_{max} < \left(\frac{\omega_e}{2\omega_e x_e} - \frac{1}{2} \right). \qquad (2.2.16)$$

In most cases, the vibrational constants are unknown for the different isotopes of a diatomic molecule. The vibrational constants are usually measured for the most abundant isotope as it is difficult to measure for less abundant isotopes. This is important to note as the vibrational energy levels will not have the same energy for different isotopes. The method to approximate the vibrational constants for different isotopes makes use of the reduced mass of the abundant isotope (for example $^{12}\text{C}^{16}\text{O}$) denoted by μ and the reduced mass of a different isotope (for example $^{12}\text{C}^{17}\text{O}$) denoted by μ_i where this relationship is given by:

$$\rho = \sqrt{\frac{\mu}{\mu_i}}. \qquad (2.2.17)$$

This leads to the vibrational energy levels for different isotopes to be described by:

$$E(n) = \rho w_e \left(\frac{1}{2} + n \right) - \rho^2 w_e x_e \left(\frac{1}{2} + n \right)^2. \qquad (2.2.18)$$

It is clear from Equation (2.2.18) that for heavier isotopes the energy levels will be more closely spaced compared to that of the abundant isotope.

The Morse potential does not approximate vibrational energies as accurately (Section 4.3) as the Dunham coefficients (Section 2.2.3), however, the strength of the Morse potential is not in approximating the energy of the vibrational levels but rather in yielding the wave function of anharmonic potential. For approximating the vibrational energies, the Dunham coefficients will be used which is a more accurate method to calculate the vibrational energies however, it is also more complex as can be seen in Section 2.2.3.

2.2.2.3 Wave function

It is now possible to solve the Schödinger Equation (2.2.8) to find the corresponding wave functions for the Morse potential. The wave functions are given by:

$$\psi_n\left(r\right) = N_n e^{-\frac{\nu}{2}e^{-\beta(r-r_e)}}\left(\nu e^{-\beta(r-r_e)}\right)^s L_n^{2s}\left(\nu e^{-\beta(r-r_e)}\right), \tag{2.2.19}$$

where ν is the constant related to the potential and s is related to the total energy [26].

$$\nu = \sqrt{\frac{8\mu D_e}{\beta^2\hbar^2}} \qquad \text{and} \qquad s = \sqrt{\frac{-2\mu E}{\beta^2\hbar^2}} \tag{2.2.20}$$

with the constraint that:

$$2s = \nu - 2n - 1. \tag{2.2.21}$$

The normalization factor for wave function is given by N_n^ν which will be derived later and $L_n^{2s}\left(y\right)$ is the associated Laguerre function which is given by:

$$L_n^k\left(y\right) = \frac{1}{n!}\sum_{i=0}^{n}\binom{n!}{i!}\binom{k+n}{n-i}\left(-y\right)^i. \tag{2.2.22}$$

The associated Laguerre functions are well known and are orthogonal over the region $[0,\infty)$ and obey the equation:

$$\int_0^\infty e^{-x}x^{k+1}\left[L_n^k\left(x\right)\right]^2 dx = \frac{(n+k)!}{n!}\left(2n+k+1\right). \tag{2.2.23}$$

To determine the normalization factor, the fact that the wave function must be orthogonal is used which leads to the following:

$$\int_{-\infty}^\infty \psi_n\left(r\right)^2 dr = \int_{-\infty}^\infty \left[N_n\right]^2 e^{-\nu e^{-\beta(r-r_e)}}\left(\nu e^{-\beta(r-r_e)}\right)^{2s}\left[L_n^{2s}\left(\nu e^{-\beta(r-r_e)}\right)\right]^2 dr = 1. \tag{2.2.24}$$

It is clear that it is possible to rewrite Equation (2.2.24) into a similar form as Equation (2.2.23) by using the substitution rule:

$$y\left(r\right) = \nu e^{-\beta(r-r_e)} \quad \implies \quad dr = -\frac{1}{y\beta}dy, \tag{2.2.25}$$

with boundary conditions :

$$y \in \left[y\left(-\infty\right),y\left(\infty\right)\right] \quad \Rightarrow \quad y \in \left(\infty,0\right]. \tag{2.2.26}$$

The substitution leads to:

$$\int_0^\infty \frac{1}{\beta}\left[N_n\right]^2 e^{-y}y^{2s-1}\left[L_n^{2s}\left(y\right)\right]^2 dy = 1. \tag{2.2.27}$$

The normalization factor can now be solved using the identities of the associated Laguerre functions and by applying integration by parts. The normalization factor is given by:

$$N_n = \sqrt{\frac{\beta\left(\nu - 2n - 1\right)\Gamma\left(n+1\right)}{\Gamma\left(\nu - n\right)}}. \tag{2.2.28}$$

It can be seen that no factorial functions were used but instead Gamma functions. It is possible to use Gamma functions since ν and n are Natural numbers and the constraint that is placed on $2s$ also ensures that $(\nu - n > 0)$ will be a Natural number. Under this conditions $n! = \Gamma(n + 1)$.

From a theoretical point of view, the Morse potential is ideal as it is applicable to all diatomic molecules and solves the Schödinger equation where the eigenvalues for this solution gives the vibrational energy levels (Equation(2.2.13)). From a spectroscopy point it is possible to measure the diatomic constants (w_e and $w_e x_e$) needed for the Morse potential. These diatomic constants can then be used to determine the dissociation energy (D_e) and β which are required in order to be able to calculate the vibrational wave functions. The vibrational wave functions can be used to determine the transition probability under the Condon approximation.

The Morse potential, vibrational energy levels, and vibrational wave functions was programmed in Wolfram Mathematica 10 as part of this study as can be found in Appendix B

2.2.2.4 Comparing Morse and Harmonic potential

The Harmonic potential is possibly the most recognised and used potential in physics. The Morse potential has a harmonic limit where $\beta \to \infty$ and $D_e \to \infty$, by applying these limits to Equation (2.2.11) and keeping k (force constant for the potential) finite the Harmonic potential is given by:

$$V(r)_{Harmonic} = \frac{1}{2}k(r - r_e)^2 \quad \text{where} \quad k = 2\beta^2 D_e. \tag{2.2.29}$$

It can be seen that there is a great difference mathematically difference between the Harmonic potential and Morse potential. This difference becomes more apparent when comparing the two potentials visually as illustrated in Figure 4.12. It can be observed from Figure 4.12 that the Morse potential behaves similarly to the harmonic oscillator close to the turning point of the potential, this will become clearer later in Section 4.3.3 when using Franck-Condon factors.

The corresponding energy values (eigenvalue coefficients for the wave function) of the Harmonic oscillator can be determined by substituting Equation (2.2.29) into the Schödinger Equation (2.2.8) and was found to be:

$$E(n)_{Harmonic} = w_e\left(\frac{1}{2} + n\right). \tag{2.2.30}$$

It can be observed that the eigenvalue coefficients of the Harmonic potential is similar to the linear term in the expression for the energy of the Morse potential (Equation (2.2.15)). It is clear that the low vibrational energy will be similar for the Harmonic and Morse potentials where $\left(n + \frac{1}{2}\right)^2$ contribution is low.

The wave functions for the Harmonic potential can now be solved by substituting Equations (2.2.29) & (2.2.30) into the Schödinger Equation (2.2.8) and was found to be:

$$\psi_n^{Harmonic}(r) = \frac{1}{\sqrt{2^n n!}}\left(\frac{\alpha}{\pi}\right)^{\frac{1}{4}} e^{-\frac{1}{2}\alpha(r-r_e)^2} H\left(n, \sqrt{\alpha}(r - r_e)\right), \tag{2.2.31}$$

where $H\left(n, \sqrt{\alpha}\left(r - r_e\right)\right)$ is the Hermite polynomial and α is related to the vibrational separation of consecutive vibrational levels which is given by ω_e. The constant α is given by:

$$\alpha = \frac{4\pi^2 c \omega_e \mu}{h}. \tag{2.2.32}$$

The Harmonic potential, vibrational energy levels, and vibrational wave functions was programmed in Wolfram Mathematica 10 as part of this study and can be found in Appendix B.

2.2.3 Dunham expansion

Dunham expansion was first introduced to the spectroscopy community in 1932 by J.L Dunham after the paper published by Philip M. Morse, as a correction to the energy level approximation for rovibronic energy levels. The Dunham expansion is given by Equation (2.2.33) where it can be observed that it does contain a $\left(\nu + \frac{1}{2}\right)$ term similar to Morse [28].

$$T\left(\nu, J\right) = \sum_i \sum_k Y_{i,k} \left(\nu + \frac{1}{2}\right)^i \left[J\left(J+1\right)\right]^k \tag{2.2.33}$$

Where $T\left(\nu, J\right)$ is the energy of the rovibronic state, ν is the vibrational quantum number, J is the rotation quantum number and $Y_{i,k}$ is known as the Dunham coefficients. The expanded Dunham coefficients can be observed in Table 2.1. The

Table 2.1: Dunham coefficients

Dunham coefficient	Coefficient name
$Y_{0,0}$	Turning point energy
Vibrational constants	
$Y_{1,0} = \omega_e$	Harmonic constant
$Y_{2,0} = -\omega_e\chi$	First anharmonic constant
$Y_{3,0} = \omega_e y$	Second anharmonic constant
$Y_{4,0} = \omega_e z$	Third anharmonic constant
Rotational constants	
$Y_{0,1} = B_e$	Rotational constant
$Y_{0,2} = D_e$	Centrifugal distortion constant
$Y_{0,3} = F_e$	
$Y_{0,4} = H_e$	
Rovibronic constants	
$Y_{1,1} = -\alpha_e$	Rotational-vibrational coupling constant
$Y_{1,2} = \beta_e$	
$Y_{2,1} = \gamma_e$	

constants for Table 2.1 can only be determined experimentally and some of these coefficients will be determined in the ensuing chapters. An alternative form of the

Dunham expansion is given by Equation (2.2.34) where it can be observed that the Dunham expansion can be split up into 4 terms.

$$T\left(\nu, J\right) = Y_{0,0} + \sum_i Y_{i,0}\left(v + \frac{1}{2}\right)^i + \sum_k Y_{0,k}\left[J\left(J+1\right)\right]^k$$
$$+ \sum_{i=1}\sum_{k=1} Y_{i,k}\left(\nu + \frac{1}{2}\right)^i\left[J\left(J+1\right)\right]^k \tag{2.2.34}$$

Where the first term is the electronic energy (turning point energy) of the potential, the second term is the "pure" vibrational contributions, the third term is the "pure" rotational contributions and the last term in this expression is the rotational-vibrational coupled contribution. It was observed in the literature [2] that the coefficients $(Y_{i,k})$ with low i, k number are magnitudes greater than that of the terms with higher i, k numbers. However, it is also important to note that for large quantum numbers ν and J the terms with higher i, k numbers coefficients will play a greater role. A comparison between the Dunham expansion and Morse approximations can be found in Section 4.3 where the calculated vibrational energies are compared.

2.2.4 Transition probability

The transition moment between two electronic states is given by:

$$A = \int \psi' p \psi''^\dagger d\tau, \tag{2.2.35}$$

where p is the electric dipole moment and ψ' and ψ'' is the total eigenfunction for the upper and lower states of the system. According to the Born Oppenheimer approximation the total eigenfunction can be written as the product of three different components as long as the vibrational and rotational coupling is weak, thus resulting in the total eigenfunction given by [27]:

$$\boldsymbol{\psi} = \boldsymbol{\psi}_e \boldsymbol{\psi}_v \boldsymbol{\psi}_r, \tag{2.2.36}$$

where $\boldsymbol{\psi}_e$ is the electronic wave function, $\boldsymbol{\psi}_v$ is the vibrational wave function and $\boldsymbol{\psi}_r$ corresponds to the rotational wave function. The electronic wave function is solely dependent on the co-ordinates of the electrons, where as the vibrational wave function is solely dependent on the internuclear separation of the molecule and the rotational wave function solely dependent on the orientation of the molecule. For the purposes of determining the vibrational-electronic transition probability, it is allowed to ignore the contributions for the rotational wave function leading to $\boldsymbol{\psi} = \boldsymbol{\psi}_e \boldsymbol{\psi}_v$. The electric dipole moment can be written as follows [27]:

$$\boldsymbol{p} = \boldsymbol{p}_e + \boldsymbol{p}_n, \tag{2.2.37}$$

where the electric dipole moment has one term dependent on the electrons $(\boldsymbol{p}_e)$ and one term dependent on the nuclei $(\boldsymbol{p}_n)$. It is important to note that $\boldsymbol{p}_n$ is independent of the electron motion.

By substituting Equations (2.2.37) & (2.2.36) into Equation (2.2.35) and keeping in mind that $\psi_{v}* = \psi_v$ then the transition moment is given by [27]:

$$A = \int \boldsymbol{\psi}_e'^* \boldsymbol{\psi}_v' \boldsymbol{p}_e \boldsymbol{\psi}_e'' \boldsymbol{\psi}_v'' d\tau + \int \boldsymbol{\psi}_e'^* \boldsymbol{\psi}_v' \boldsymbol{p}_n \boldsymbol{\psi}_e'' \boldsymbol{\psi}_v'' d\tau. \qquad (2.2.38)$$

Since $\boldsymbol{p}_e$ and $\boldsymbol{\psi}_e$ only depend on the electronic coordinates and $\boldsymbol{p}_v$ and $\boldsymbol{\psi}_v$ only depend on the nuclear coordinates it is possible to rewrite Equation (2.2.38) into:

$$A = \int \boldsymbol{\psi}_v' \boldsymbol{\psi}_v'' d\tau_n \int \boldsymbol{\psi}_e'^* \boldsymbol{p}_e \boldsymbol{\psi}_e'' d\tau_e + \int \boldsymbol{\psi}_v' \boldsymbol{p}_n \boldsymbol{\psi}_v'' d\tau_n \int \boldsymbol{\psi}_e'^* \boldsymbol{\psi}_e'' d\tau_e. \qquad (2.2.39)$$

The electronic eigenfunctions belonging to different electronic states are orthogonal thus leading to $\int \boldsymbol{\psi}_e'^* \boldsymbol{\psi}_e'' d\tau_e = 0$. In addition, it is also known that the vibrational wave functions are only dependent on the internuclear distance r, thus leading to the following expression for the transition moment:

$$A = \int \boldsymbol{p}_e \boldsymbol{\psi}_e' \boldsymbol{\psi}_e''^* d\tau_e \int \boldsymbol{\psi}_v' \boldsymbol{\psi}_v'' dr. \qquad (2.2.40)$$

The first integral is known that the electronic transition moment has a small dependence on the internuclear distance and this fact is used in the Condon approximation.

2.2.4.1   Condon approximation

Under the Condon approximation, it is assumed that the timescale in which the electronic transitions occur is so much smaller than that of the nuclear motion that the geometry of the nuclei remain unchanged and therefore can be considered constant resulting in the following expression:

$$P = |A|^2 = R_e^2 \left| \int \boldsymbol{\psi}_v' \boldsymbol{\psi}_v'' dr \right|^2. \qquad (2.2.41)$$

The square of the integral $\int \boldsymbol{\psi}_v' \boldsymbol{\psi}_v'' dr$ is known as the Franck-Condon factor and R_e is the average electronic transition moment, and is taken as a constant for the transitions between two selected electronic states in the Condon approximation.

The Franck-Condon factor relates to the probability for a specific vibronic transition between vibrational levels of two different electronic states. The Franck-Condon factors are very useful tools in laser spectroscopy as it can aid in determining if self-absorption occurs and can be used to pre-plan experiments according to the probability of transitions occurring between different potentials. The Franck-Condon factors (FCF's) are calculated by determining the overlap of the wave functions of the two vibrational levels of different electronic states and is given by:

$$q_{v'v''} = \left[\int_0^\infty \psi_n^i \left(y(r) \right)^* \psi_m^j \left(y(r) \right) dr \right]^2, \qquad (2.2.42)$$

where i and j denote the wave functions for the different potentials and n and m denote the vibrational level. When considering transitions from a specific vibrational level in an electronic state to different levels in a different electronic state the Franck-Condon factors are equal to the probability. It is also important to note that in the case of diatomic molecules only real eigenfunction are considered thus $\psi''^* = \psi''$.

2.2.4.2   r-Centroid approximation

The r-Centroid approximation was first introduced in the 1954 by P. A. Fraser as a result of increasing accuracy in intensity measurements in experiments which showed that there is a need for an improvement to the Condon approximation [29]. The r-Centroid approximation builds on the Condon approximation where it is approximated that the transition moment can be written in the form of Equation (2.2.41). However, in this approximation the electronic transition (R_e) is not approximated to be constant instead it varies with the vibrational quantum number. The transition probability can be written as [30]:

$$P_{v'v"} = R_e^2 \left(\bar{r}_{v'v"} \right) q_{v'v''}, \tag{2.2.43}$$

where $\bar{r}_{v'v"}$ is the r-centroid and is given by:

$$\bar{r}_{v'v"} = \frac{\langle v'|r|v"\rangle}{\langle v'|v"\rangle}. \tag{2.2.44}$$

This equation can be interpreted as the internuclear distance where the probability of transition between the two electronic states is the highest.

The r-Centroid approximation makes the assumptions that the electron transition ($R_e^2 \left(\bar{r} \right)$) can be can be represented by a power series expansion given by Equation (2.2.45). Under the condition that the first term is retained, Equations (2.2.43) & (2.2.41) become identical.

$$R_e \left(r \right) = R_0 \left(1 + a_1 r + a_2 r^2 + a_3 r^3 \right) \tag{2.2.45}$$

It is important to note that the constants (a_1, a_2, a_3) given by Equation (2.2.45) can only be determined experimentally and that when incorporating higher terms of Equation (2.2.45) the r-Centroid needs to satisfy the following condition:

$$\bar{r}_{v'v"}^n = \overline{r_{v'v"}^n} \quad \implies \quad \left(\frac{\langle v'|r|v''\rangle}{\langle v'|v''\rangle} \right)^n = \frac{\langle v'|r^n|v''\rangle}{\langle v'|v''\rangle}. \tag{2.2.46}$$

The transition probability under the Condon approximation and the r-Centroid approximation was programmed in Wolfram Mathematica 10 as part of this study and can be found in Appendix B.

2.3   Supersonic free-jet expansion

In this study, a pulsed valve was used to introduce the CO gas sample into the vacuum system described in Section 3.2. When the high-pressure gas freely expands into the vacuum system through a small orifice it forms a supersonic gas jet as a result of the pressure difference between the stagnant gas (1 to 4 bars) and the vacuum system (10^{-6} mbar) as illustrated in Figure 2.13. This type of supersonic gas jet is known as a supersonic free-jet expansion. During the formation of the supersonic gas jet, adiabatic cooling of the internal energy occurs. An adiabatic process is one where no transfer of thermal energy nor matter between the thermodynamic system and
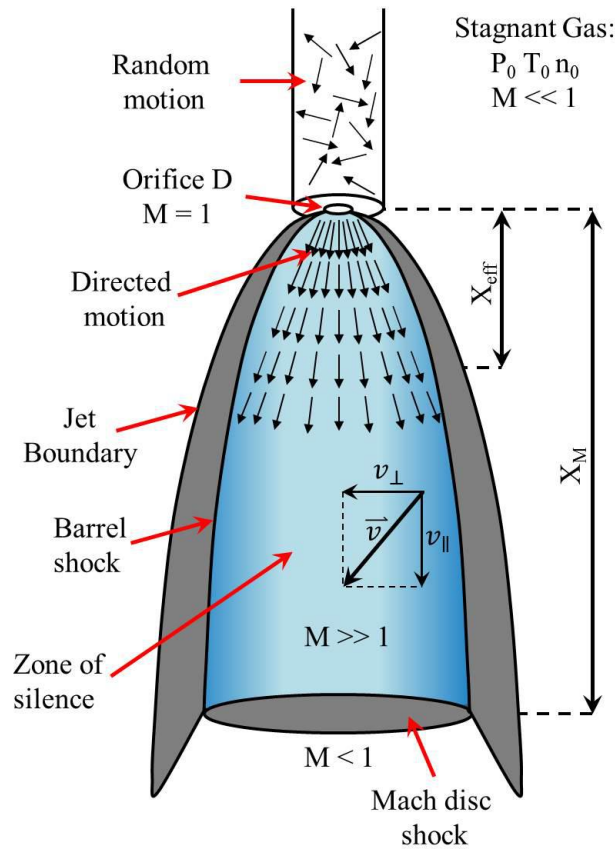
Figure 2.13: Schematic representation of a supersonic free-jet expansion. Parameters: Stagnant gas pressure P_0, stagnant gas temperature T_0, stagnant gas density n_0, Mach number M, diameter of orifice D, effective Mach number M_{eff}, distance from orifice X_{eff}, transverse velocity $v_\perp$, translational velocity $v_\parallel$.

its surroundings occurs. In the case of adiabatic free expansion where gas expands into a vacuum system the work done by and onto the system is zero leading to the change in the total internal energy of the system to be zero.

Once the stagnant gas expands into the vacuum system it leads to an increase in the volume and a decrease in temperature. In the stagnant gas four different temperatures can be defined: $T_\parallel$ is the translational temperature governed by the translational velocity in the vertical direction ($v_\parallel$); $T_\perp$ is the transverse temperature governed by the transverse velocity in the horizontal plane ($v_\perp$); T_v is the vibrational temperature and T_r is the rotational temperature. For the stagnant gas these components are all equal ($T_0 = T_\parallel = T_\perp = T_v = T_r$) [31].

During the creation of the supersonic gas jet, the thermal energy of the molecules are partly transferred into energy associated with the bulk flow of the gas. This energy transfer will occur at the orifice where the highest probability of collision occurs.

The conversion of the velocity distribution from a random motion (stagnant gas leading to $M \ll 1$) to directed motion of gas particles in the jet leads to a narrowing

of the transversal velocity distribution ($M \gg 1$), resulting in a decrease in the transversal thermal energy ($T_\perp$). Although the average $v_\parallel$ increases due to the bulk flow the width of the velocity distribution of $v_\parallel$ around the average decreases and $T_\parallel$ decreases. Energy transfer from vibrational and rotational degrees of freedom to the cold translational degrees of freedom takes place and lowers the vibrational and rotational thermal energies. The rotational thermal energy is lower than that of the vibrational thermal energy as the cross-section for collision-induced rotational transitions is greater than that of the cross-section for collision-induced vibrational transitions ($E_r < E_v$). The thermal energy of the supersonic gas jet can also be described by the four thermal components ($E_\parallel, E_\perp, E_v, E_r$), however, in the case of the supersonic gas jet these components have the following distribution: $E_\perp < E_\parallel < E_r < E_v$.

A schematic representation of the supersonic gas jet is illustrated in Figure 2.13, where it can be observed that the supersonic gas jet is surrounded by a shock barrier known as the barrel shock. A Mach disc shock can further be observed which is created by the molecules of the supersonic gas jet colliding with surrounding gas, the distance at which this occurs is indicated by X_M and given by [32]:

$$X_M = 0.67D\sqrt{\frac{P_0}{P_1}}, \qquad (2.3.1)$$

where D is the diameter of the orifice, P_0 is the pressure of the stagnant gas and P_1 is the pressure of the vacuum chamber. The X_M distance is of high importance as the zone of silence does not exist after this point. The zone of silence is the region inside the supersonic gas jet where no collisions between the molecules of the sample gas exist and is thus the optimal position for spectroscopy.

It is possible to calculate the distance from the orifice to the position where the laser pulse must interact with the supersonic gas jet (also known as the effective distance X_{eff}) to achieve a given effective Mach number (M_{eff}) [31]:

$$M_{eff} = 3.26 \left(\frac{X_{eff}}{D} \right)^{0.67}. \qquad (2.3.2)$$

Additionally, for a given M_{eff} it is possible to calculate the translational temperature ($T_\parallel$) inside of the supersonic gas jet and is given by [33]:

$$T_\parallel = T_0 \left[1 + \frac{1}{2}(\gamma - 1)M_{eff}^2 \right]^{-1}, \qquad (2.3.3)$$

where T_0 is the temperature of the stagnant gas and γ is the heat capacity ratio ($\frac{c_p}{c_v}$). The effective density (n_{eff}) can be expressed by [32]:

$$n_{eff} = n_0 \left[1 + \frac{1}{2}(\gamma - 1)M_{eff}^2 \right]^{-\frac{1}{\gamma - 1}}. \qquad (2.3.4)$$

It can be observed that the expression for the relative density also depends on the heat capacity ratio and the effective Mach number.

Chapter 3

Experimental setup and techniques

3.1   Vacuum ultraviolet light source

Vacuum ultraviolet light was generated by using the setup shown in Figure 3.1. A Nd:YAG laser (neodymium-doped yttrium aluminium garnet; Nd:Y3Al5O12, module Pro-270-10 developed by Quanta-ray Spectra-Physics Laser inc.) was used as a pump laser for two dye lasers. Dye laser *II* (Sirah CSTR-D-24 manufactured by Laser-und Plasmatechnik GmbH) is a tuneable dye laser. This laser can be tuned between 370 nm to 560 nm and provides ω_2. Dye laser *I* (Lambda Physik module Fl 3001 manufactured by Lasertechnik) was set at a wavelength of 430.9378 nm and it provides ω_1. Considering the incident wavelengths that are accessible with commercial laser dyes, the accessible VUV range was calculated to be between 136.17 nm to 155.60 nm. The light that is emitted by the dye lasers is aligned co-linearly, is po-
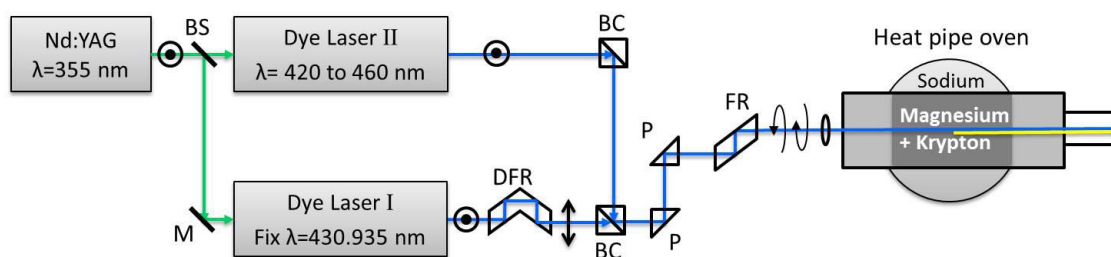
Figure 3.1: Experimental design for VUV generation. Components: Beam splitter (BS), Double Fresnel rhombus (DRF), Polarising beam combiner (Glan-Taylor prism) (BC), Fresnel rhombus (FR), Fused Silica prism (P), Mirror (M).

larised circularly and then weakly focused ($f \approx 100$ cm) into a heat pipe oven. The heat pipe oven is filled with magnesium vapour and krypton gas. The krypton gas is used to achieve phase-matching. Magnesium is used because of its high non-linear

susceptibility for generating VUV light by two-photon resonant sum-frequency generation ($\omega_{vuv} = 2\omega_1 + \omega_2$ see Section 2.1.3). The light that is emitted from the heat pipe oven is a mixture of VUV light and light that did not get converted to VUV light. This light then proceeds into a vacuum system in order to prevent oxygen from absorbing the VUV light.

3.1.1 Characterisation of incident beams

In the previous section, it was mentioned that two dye lasers are used to generate VUV light. In this section, the experimental setup used to characterise the incident laser beams will be discussed. In Figure 3.2 it is illustrated how the internal reflection
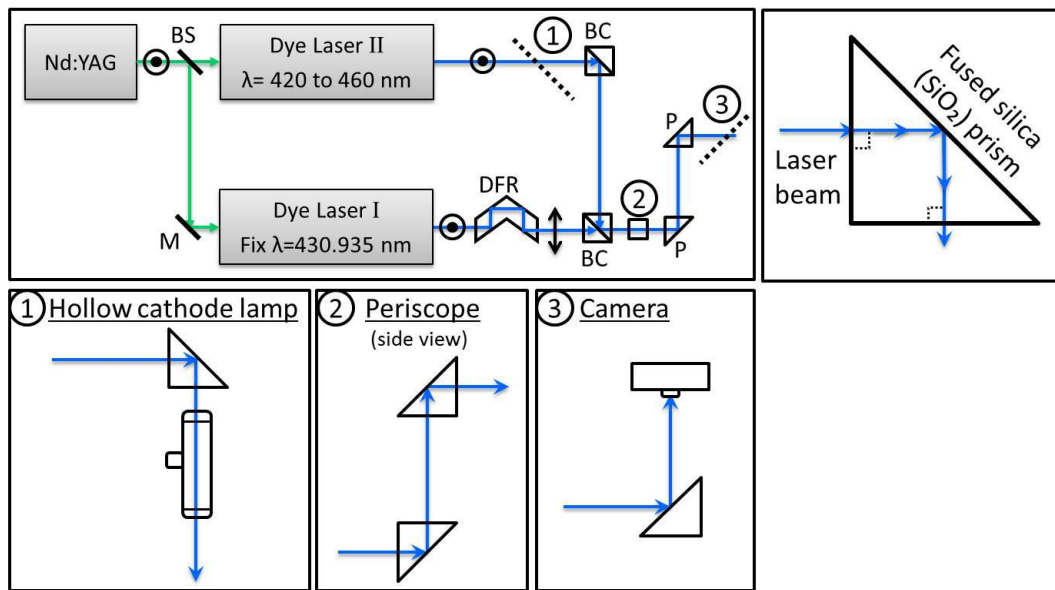
Figure 3.2: Optical path of dye lasers with detailed inserts of a hollow cathode lamp calibration setup ①, the side view of the periscope ② and a beam profiling camera setup ③.

of fused silica prisms are utilized. Three parts of the setup are of interest:① A see-through hollow cathode lamp (zirconium element and neon gas) setup where the light was reflected using the internal reflection of a fused silica prism to the hollow cathode lamp. This setup was used to measure optogalvanic spectra of neon for calibration of the tuneable dye laser and was removed after calibration was achieved; ② A periscope is used in the system to achieve the correct beam height in the horizontal plane, this setup is part of the system and is not removed; ③ A Coherent beam view analyzer LaserCam (Coherent beam view analyzer Analog 2.3 Digital 3.1) camera was used to determine the beam drift as a result of a change in the index of refraction caused by a change in the wavelength of the tuneable dye laser. It can be observed that an outer reflection of the fused silica prism is used as the camera can not withstand high-intensity light. The beam path length to the camera was

selected to be the same as the path length to the center of the heat pipe oven. This was done to ensure an accurate estimation of the beam drift in the center of the heat pipe oven. This setup was then removed after the beam drift was successfully determined.

3.2 Vacuum ultraviolet spectroscopy setup

Vacuum ultraviolet spectroscopy measurements were achieved by using the setup illustrated in Figure 3.3. The VUV light from the heat pipe oven crosses and interacts with a supersonic gas jet. The VUV light that is not absorbed by the sample gas then travels along the vacuum chamber until a portion ($\sim 10\%$) is split off by a magnesium fluoride (MgF_2) window, attenuated by 3 more reflections and measured by a Hamamatsu R 6835 solar blind photomultiplier tube (PMT3) with a wavelength range of 115-200 nm.
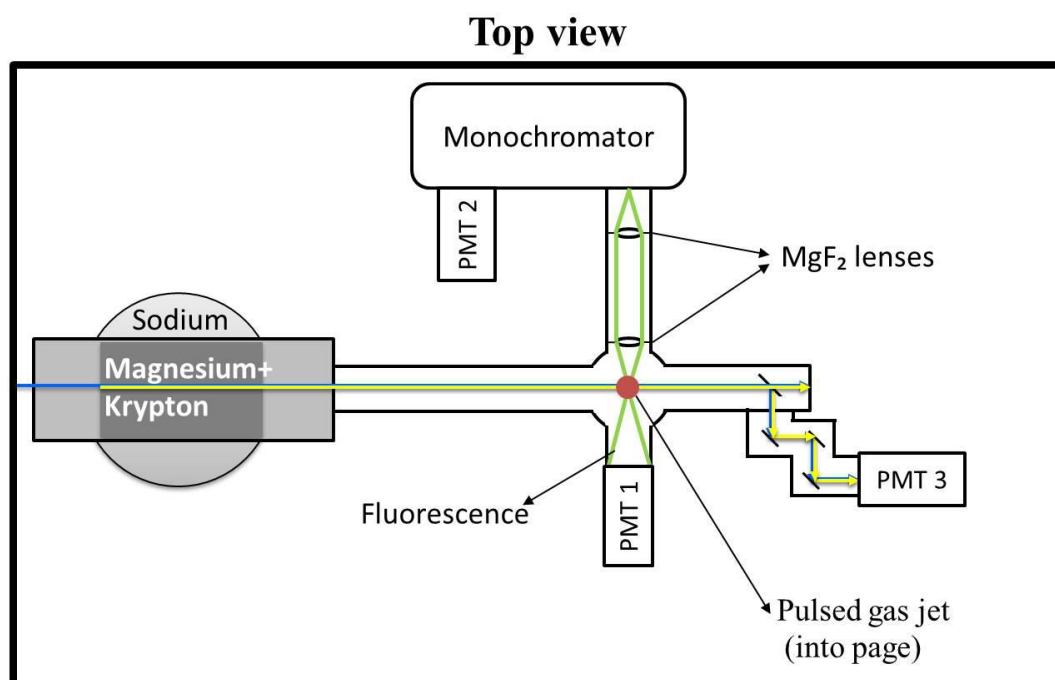
Figure 3.3: Experimental layout for vacuum ultraviolet spectroscopy. Blue line visible light and Yellow line VUV light.

The gas sample is introduced into the vacuum system by means of a Parker pulsating valve. The gas is cooled by an adiabatic expansion (see Section 2.3). The VUV light is absorbed by the sample gas resulting in excitation of the gas. When the gas de-excites to the ground state, it emits fluorescence in all directions. A fraction of the fluorescence is measured by a Hamamatsu R 6835 solar blind photomultiplier PMT2.

Furthermore, a fraction of the fluorescence also enters the scanning monochromator (Section 3.2.2) by using two planar convex MgF_2 lenses (lens specifications in Section 3.2.1). The fluorescence that propagates inside the scanning monochromator is then measured by the photomultiplier PMT1. The selection of the PMT is dependent on the type of measurement to be taken as explained in Sections 4.4 & 4.6.

3.2.1   Lens Selection

MgF_2 lenses are transparent in the VUV range and were therefore used (Figure 3.3). Since the fluorescence emitted by the sample gas is in all directions, it was necessary to collimate the light by using a collimating lens. For optimal light collection, a collimating lens with a diameter of 25 mm (maximum diameter allowed by vacuum tube) and a focal length of 76.22 mm at 144 nm wavelength, was mounted 75 mm from the point of fluorescence (minimum focal distance allowed by vacuum chamber). It is important to note that the diameter of the collimated light beam is 25 mm. The light was then passed through a focusing lens with a focal length of 152.03 mm at 144 nm wavelength also with a diameter of 25 mm. The focusing lens was mounted 150 mm away from the entrance slit of the scanning monochromator. The focal length of this lens was specifically selected since a magnification of approximately 2 was required for the light beam to have a diameter of approximately 50 mm (the beam diameter was calculated as 46.86 mm) on the first mirror inside the monochromator. This was necessary to achieve optimal diffraction by illuminating the full surface of the grating (Figure 3.6).

When working in the VUV range it is important to note that the focal length given by the manufacturer is measured at a wavelength of 633 nm, thus the focal lengths in the VUV range will be significantly different and are calculated by using the lens-maker's formula given by:

$$\frac{1}{f(\lambda)} = \frac{(n(\lambda)_{lens} - n_0)}{n_0}\left(\frac{1}{R_1} - \frac{1}{R_2}\right),\tag{3.2.1}$$

where n_0 is the index of diffraction of the surrounding medium (in air $n_0 = 1$), R_1 and R_2 is the radius of curvature of the lens (if plano-convex lens $\frac{1}{R_2} = 0$) and $n(\lambda)_{lens}$ is the index of diffraction of the lens which is wavelength dependent and given by the Sellmeier-type dispersion equation:

$$n(\lambda)^2 = 1 + \sum_i A_i \frac{\lambda^2}{\lambda^2 - \lambda_i^2},\tag{3.2.2}$$

where λ_i is the calculated wavelength of an oscillator and A_i is the corresponding strength of the oscillator (data used from [13] which can be found in Table A.1). The relationship between the focal length and the wavelength as well as the index of refraction can be observed in Figure 3.4. The focal lengths calculated was also compared to the focal lengths given by the manufacturer for specific wavelengths. It can be observed that the calculated values are within 0.01% of that given by the manufacturer (Table 3.1).
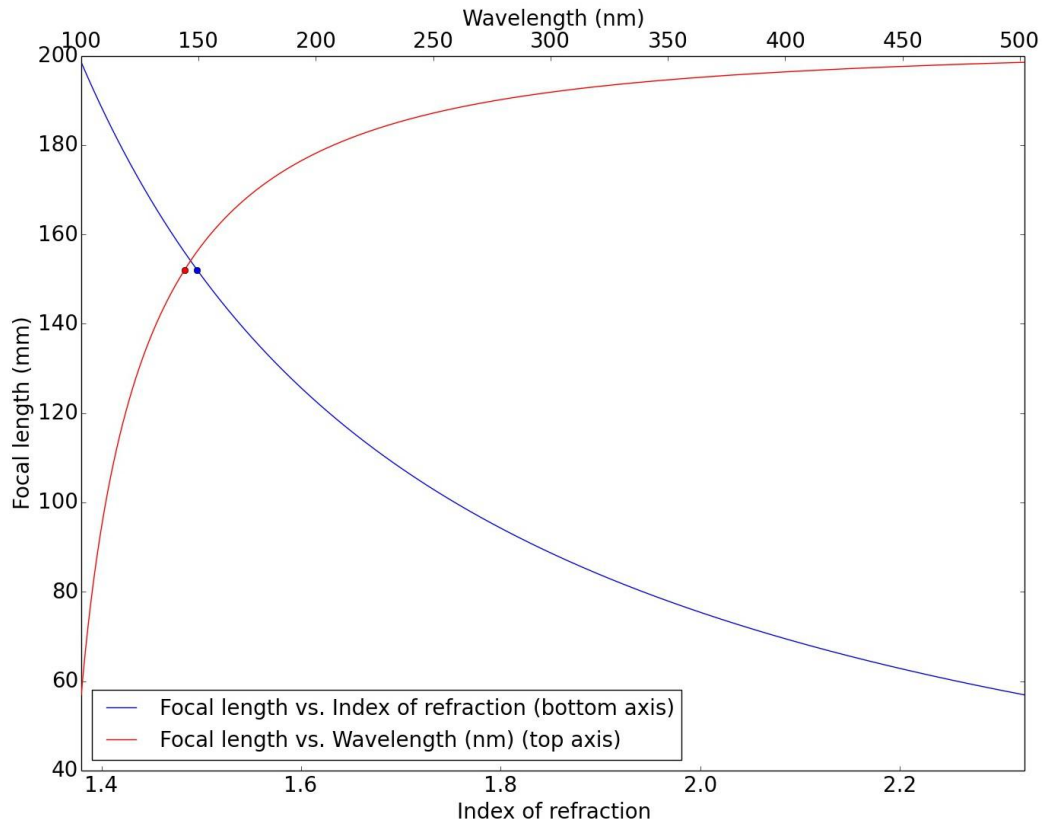
Figure 3.4: Calculated focal length (y-axis) vs. wavelength (top x-axis) and index of refraction (bottom x-axis) for a plano-convex lens with $\frac{1}{R_2} = 0 \, \text{mm}$ and $R_1 = 75.4 \, \text{mm}$. Red curve: focal length as a function of the wavelength. Blue curve: focal length as a function of the index of refraction.

Table 3.1: Calculated focal lengths compared with that of the manufacturer [9] for a radius of curvature of 75.4 mm

Wavelength (nm)	Focal length (mm) from manufacturer [9]	Calculated focal length (mm)	Percentage difference
144	Not given	152.03	
200	178.2	178.21	0.006
486	198.3	198.31	0.005
633	200	200.01	0.005
2000	205.0	204.98	0.01

3.2.2   McPherson 218 scanning monochromator

A McPherson 218 scanning monochromator was used in this study. In Figure 3.5 the optical path of the McPherson 218 is illustrated. The scanning monochromator uses the Czerny-Turner X formation. This optical path diagram has been placed over an image of the scanning monochromator (Figure 3.6) to explain the properties of
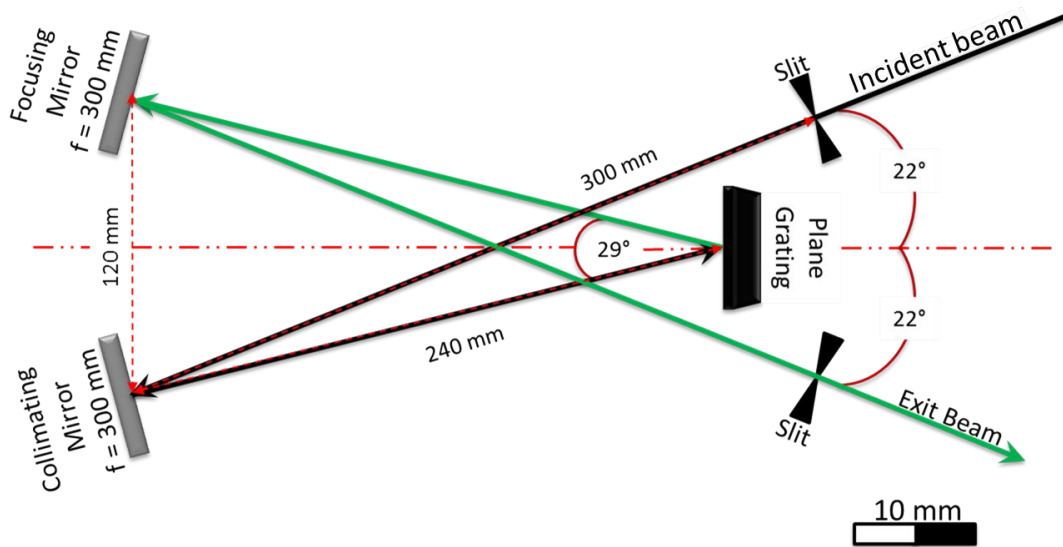
Figure 3.5: Optical path of McPherson 218

the scanning monochromator in further detail. In Figure 3.6 some extra mechanical properties can be seen. The rotating axis can be rotated by hand or by a stepper motor. In this study, a stepper motor (RAPID SYN: 23H-501 manufactured by Computer Devices Corp., Santa Fe Springs, California; not visible in Figure 3.6) was incorporated to rotate the rotating axis. The rotating axis moves the drive train along the rotating axis, the lever converts this transversal motion into rotational motion in order to rotate the grating. As the rotating axis moves the drive train from top to bottom (in Figure 3.6) the grating will rotate counter-clockwise. The limit switches in Figure 3.6 provide a very important function in the setup as it prevents the drive train from running off the rotating axis.

3.2.2.1 Light propagation inside McPherson 218

The light that is transmitted through the entrance slit (slit size 0 mm to 2 mm) will first be collimated and reflected by the collimating mirror (focal length of 300 mm and dimensions of 50 mm by 50 mm) to the grating. The grating (grating number of 2400 grooves/mm and blazed for 105 nm with dimensions 50 mm by 50 mm) will diffract the light into its different wavelengths. The diffracted light of the first order reaches the focusing mirror (focal length of 300 mm and dimensions of 50 mm by 50 mm) which will, in turn, reflect the light to the exit slit. For monochromatic light, the image that forms on the exit slit (slit size 0 mm to 1.5 mm) will have the same dimensions as the entrance slit.
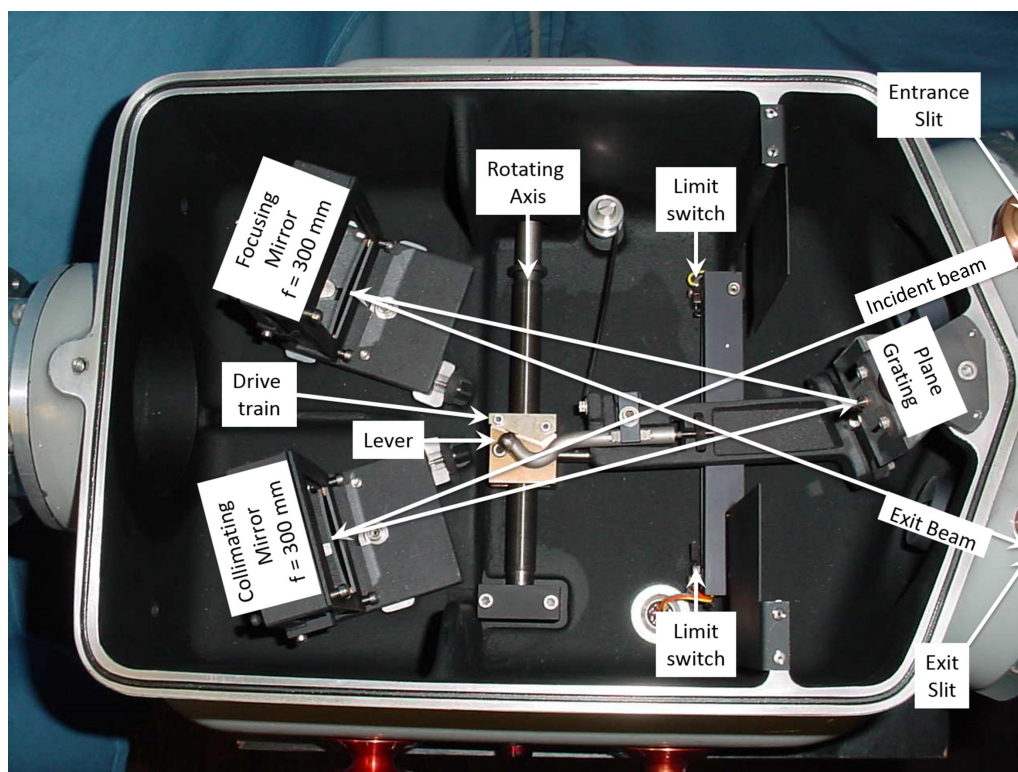
Figure 3.6: Beam path superimposed on scanning monochromator image

[34]

3.2.2.2 Computerised control of McPherson 218

A stepper motor was used to rotate the grating, this motor was controlled by using a controller and data acquisition (Daq) device (Uragan μ Daq developed by Synertronic Designs). This device did not only control the stepper motor but also retrieved information regarding the step count and the signal from the PMT. The Daq device was controlled by using Uragan Studio Software. In the software, there is a terminal in which Python scripting is permitted with private functions which aid in controlling the stepper motor. I developed the custom script which was used in this study to control the stepper motor as part of my BScHons degree [35]. In Figure 3.7, a flow diagram is used to illustrate the basic construction of the program.

The program allows sequential scanning over multiple wavelength regions in one scan. During the first step, the program switches the motor on. The program will then check if a single region was selected, if not it will skip this operation. Conversion from wavelength to steps is necessary since the Uragan Studio Software only works in steps and not wavelengths. The program will check that the safety parameters are not being breached, however, if it is then the program corrects for that by using the safety constants for speed and position so that the system does not get damaged. Additionally, the program also checks that the regions are being scanned from short to long wavelengths and inverts the scanning direction if necessary as this is recommended in the instruction manual. The resolution of the graph (not spectral
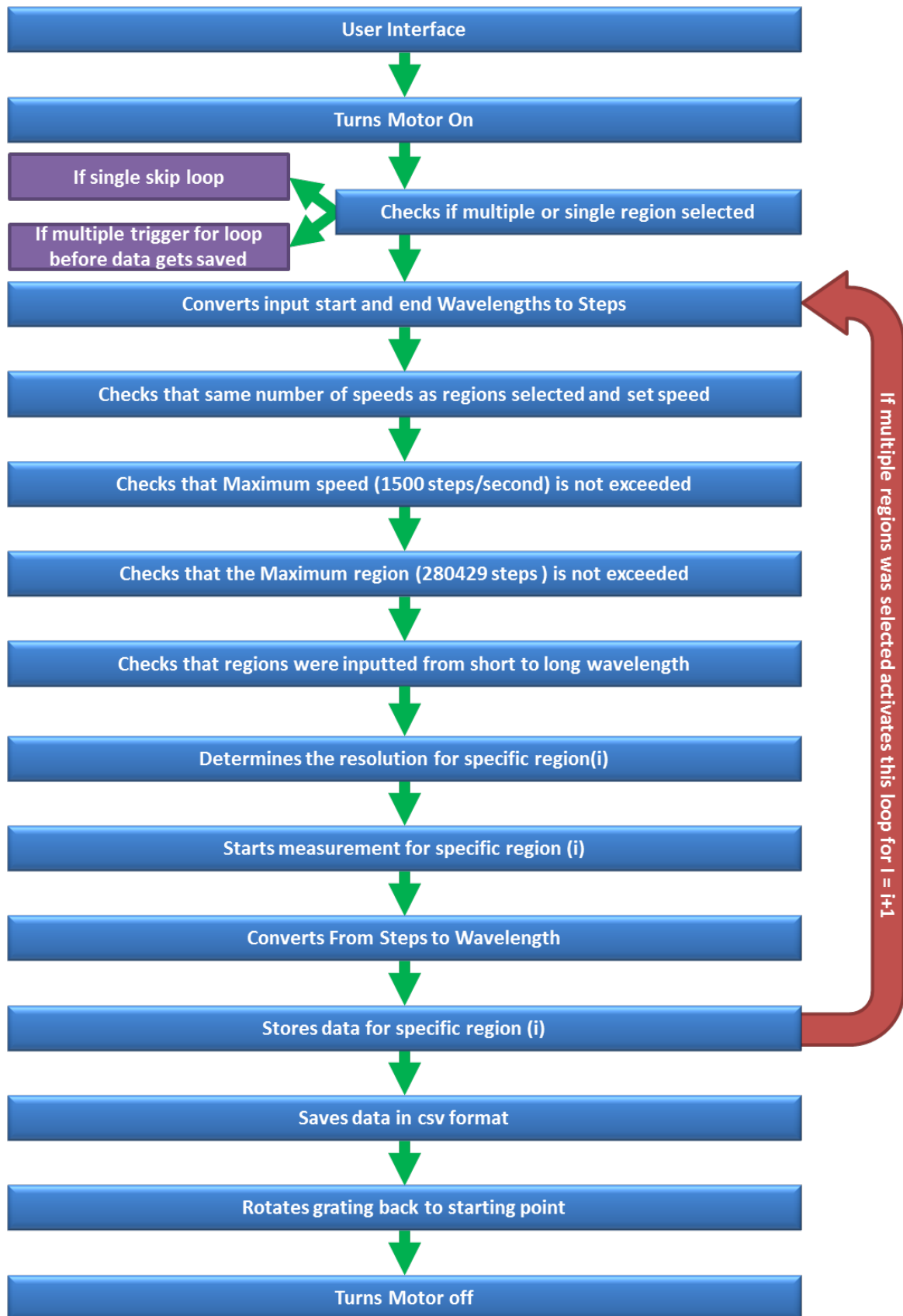
Figure 3.7: Program flow diagram

resolution) is calculated from the input parameters (wavelength range and scanning speed) as well as the number of data points (chosen to be fixed at 50000). After a successful measurement is achieved the data collected is exported in the form of a CSV file.

The backlash of the system is counteracted by the Uragan Studio Software. The software has the option of inserting a number of backlash steps. For this study 2000 steps (4.09 nm) was selected to counteract the backlash of the system which was found to be 1568 ± 63 steps. When the software detects that the stepper motor is going to move from a longer wavelength to a shorter wavelength, the backlash function is activated. This function will move 4.09 nm past the desired position (long to short wavelength direction) and then only move to the desired position (short to long wavelength direction).

The wavelength reproducibility was also investigated [35] and was determined to be 16.74 motor steps (0.034 nm) which is similar to that of the spectral resolution (0.03 nm) given by the manufacturer. The spectral resolution was also determined experimentally and was found to be 0.45 nm in the VUV range, with an entrance slit size of 155 μm and exit slit size 40 μm, where the spectral resolution of the system is determined by the size of the largest slit.

3.2.2.3 Calibration set-up for scanning monochromator

Previous calibration of the scanning monochromator was achieved using a high-pressure mercury lamp in the wavelength range of 550-320 nm however, it was discovered that extrapolating this calibration to the VUV range was not sufficient. Re-calibration of the scanning monochromator was necessary in order to have reliable wavelength measurements in the visible (420 nm) and the VUV (142 nm) wavelength region. To achieve this calibration a similar setup shown in Figure 3.8 was used. In
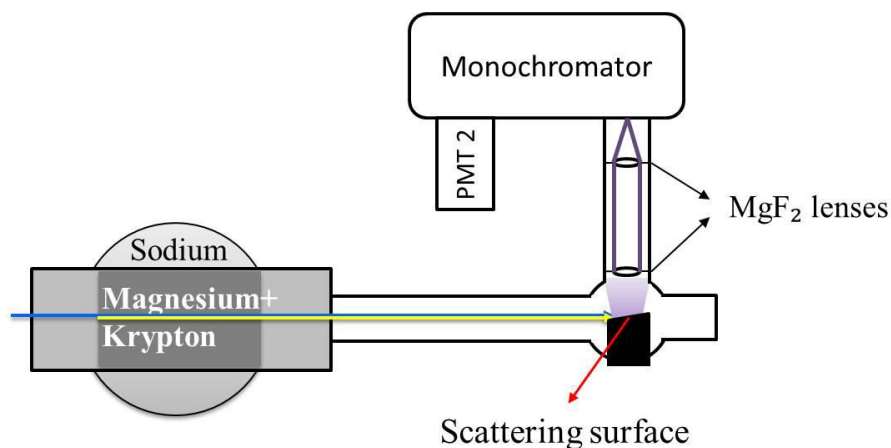
Figure 3.8: Calibration set-up for scanning monochromator.

Figure 3.8 it can be observed that the visible and VUV light from the heat pipe is diffracted off a sandblasted glass slide with an angle of incidence of 10 °C. This angle

was specifically selected in order to spread the laser beams as evenly as possible over the sandblasted glass to produce scattered light with a uniform intensity at the entrance slit. Previous measurements indicated that placing the sandblasted glass slide at an angle of 45 °C caused an uneven intensity distribution at the entrance slit as a result of not only scattered light but also specular reflections reaching the entrance slit. In addition, the sandblasted glass slide was also placed at the position from which the fluorescence from the gas jet is emitted therefore increasing the accuracy of calibration for fluorescence measurements.

3.2.3 Data collection

For data collection, our laboratory makes use of a set of seven Gated Integrators and Boxcar Averagers (SR250 Gated Integrator). The signal from the PMT's are pulses which enter the boxcar integrator, the boxcar integrator integrates over a selected part of the signal and returns a constant voltage which can then be recovered by the DAQ. A boxcar can be triggered internally or externally. In our laboratory external triggering is achieved by using a photodiode inside of the Lambda Physik laser (Figure 3.1, photodiode not shown) to ensure that the boxcars are synchronised with the laser pulses. When a boxcar is triggered it emits a signal at an output named "busy" this signal is then used to trigger the second boxcar. The busy signal from the second boxcar will then be used in turn to trigger the third and so on, thus only one boxcar is triggered by the photodiode. The boxcars make use of an integration gate which can be adjusted using the delay settings (moves the gate in time relative to the signal) and gate width setting (altering the integration bounds). Boxcars can additionally, replicate the input signal and emit this replicated signal at the "signal output" port. A signal can also be multiplied by adjusting the sensitivity settings, however, this is not advised when reliable intensity measurements are required as the exact multiplication factor may differ from boxcar to boxcar. The last setting on the boxcars deals with averaging which can be set between 1 (last sample) to 10 k. It is important to note that the boxcars use a moving exponential average technique.

The signal from the photodiode in Figure 3.9 is split in two, where one part is used to trigger the delay generator and the second part is used to trigger a boxcar integrator. Once the delay generator is triggered it will emit a block pulse signal with a specific delay. The delay generator used is a 4 channel Stanford research systems delay generator (DG535) which can emit up to 4 separate signals, one of these signals are used to trigger the pulsed valve and another signal is used to trigger the LabVIEW DAQ device (NI USB 6211). The remaining signal from the photodiode in Figure 3.9 is used to trigger boxcar 1A, this boxcar integrates the signal from PMT1. The signal from the "signal output" is used as the signal input of boxcar 1B to investigate fluorescent signals that have longer lifetimes. These signals are investigated by increasing the integration gate delay (Figure 3.10). The "busy" signal from boxcar 1A is used to trigger boxcar 1B. The same processes between boxcars 1A and 1B are repeated for boxcars 1B, 1C and 1D all with different integration gate delays. Boxcar 1A was used to measure the short-lived fluorescence of singlet-singlet transitions whilst boxcars 1B, 1C and 1D are used to measure the longer-lived fluorescence resulting from forbidden triplet-singlet transitions with different
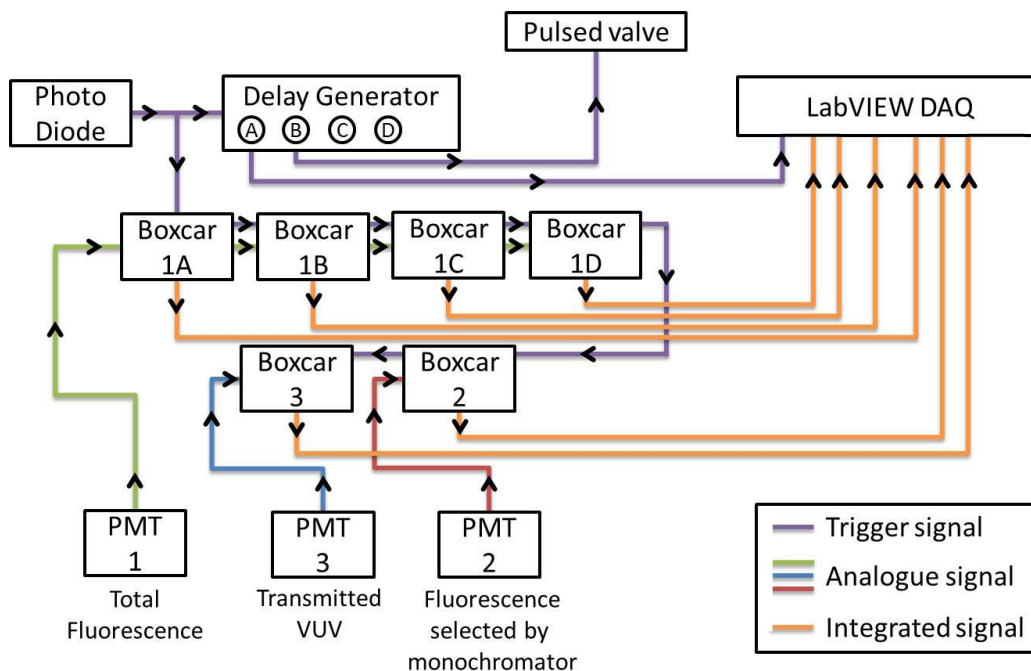
Figure 3.9: Diagram of the data acquisition system showing trigger and signal pathways. In this setup, the laser and pulsed valve both operate at 10 Hz.

time delays for the integration gates. Using different time delays for boxcars 1B, 1C and 1D allows for investigation of the optimal time delay of the integration gate for the singlet-singlet and the triplet-singlet signal as illustrated in Figure 3.10. My investigation did not include results obtained using boxcars 1B, 1C and 1D due to time limitations.

The "busy" signal from boxcar 1D is used to trigger boxcar 2. Boxcar 2 is used to integrate the signal from PMT2. Boxcar 2 is the only boxcar where the averaging setting is used, this setting is only used during measurements where the scanning monochromator is used to record the fluorescence spectrum of CO, in this case, the averaged integrated signal does not go to the LabVIEW DAQ but rather goes to the Uragan μ Daq. The "busy" signal from boxcar 2 is used to trigger boxcar 3 which is used to integrate the signal from PMT3.

All integrated signals from the boxcars go to the LabVIEW DAQ where the signals are recorded with their corresponding wavelengths. When a measurement is performed the wavelength region is selected as well as the wavelength step size and the number of laser pulses to be recorded at each step. This leads to a pulse to pulse averaging method where for example 30 pulses will be recorded at a wavelength before the wavelength is altered.

In order to measure the transmitted VUV light without interference from the CO gas jet during measurements, it was necessary to change the frequency of the pulsed valve from 10 Hz to 5 Hz, thus ensuring that every second laser pulse is allowed to be detected by PMT3 without interacting with the CO gas jet. To change the pulse frequency of the pulsed valve it was necessary to add an additional delay generator
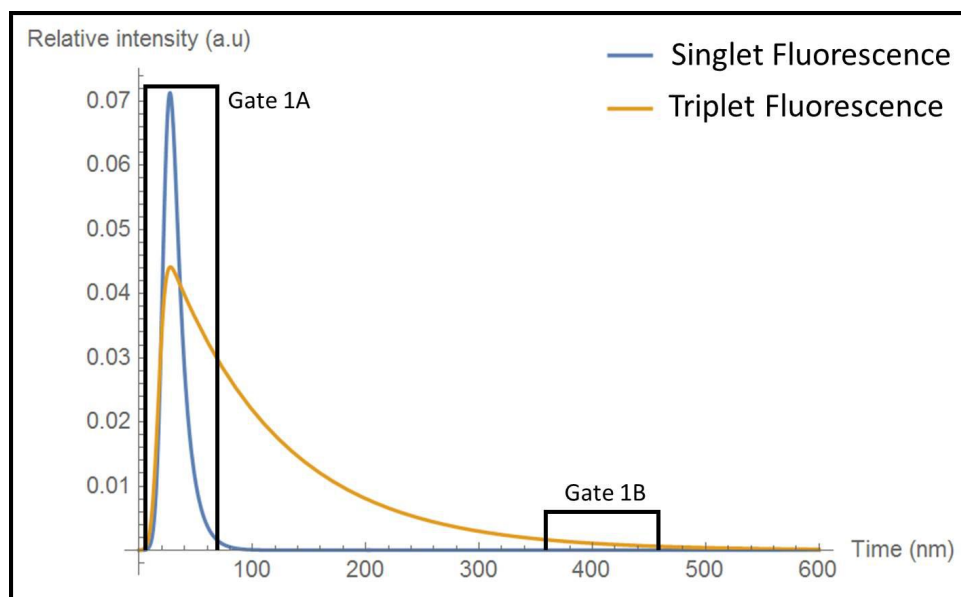
Figure 3.10: Illustration of the integration gates used to detect fluorescence from singlet and triplet excited states.

as can be observed in Figure 3.11. It was observed that adding the delay generator and setting its delay to 100 ms did change the frequency of the pulsed valve to 5 Hz. However, it was not possible to split the data set into "sample" and "no sample" data by simply selecting every second data point in the full data set as the boxcars were not triggered at every second pulse. This is illustrated in Figure 3.12.A.

It was determined that the boxcar was not triggered. If the delay generator was not triggered then no data will be recorded as the LabVIEW DAQ is dependent on the signal from the delay generator. The boxcars have a trigger level which is fixed at the start of a measurement to a specific level. The signal from the photodiode needs to be greater than this specific value otherwise the boxcars will not integrate the signal which it receives from the PMT. The signal strength of the photodiode is dependent on the pump laser, and it is known that the intensity of the pump laser does fluctuate slightly. This fluctuation will not have a significant impact when conducting measurements where the laser pulse and pulsed valve are operating at 10 Hz.

In order to split the data correctly, a signal from the new delay generator was needed to be recorded. The signal from the delay generator was sent to boxcar 4 and recorded as a reference signal. Boxcar 4 is triggered by the "busy" signal from boxcar 1D. The integrated signal from boxcar 4 also goes to the LabVIEW DAQ. The signal recorded by the LabVIEW DAQ from boxcar 4 is used as a reference signal to distinguish between both the laser pulses which do not interact with the CO gas jet and the laser pulses which interact with the CO gas sample. It is, therefore, possible to split all the data into two separate sets of data. The first data set is when the pulsed valve is triggered and the second data set is when the pulsed valve is not triggered. A custom program was written in order to split the data as illustrated in Figure 3.12.B.
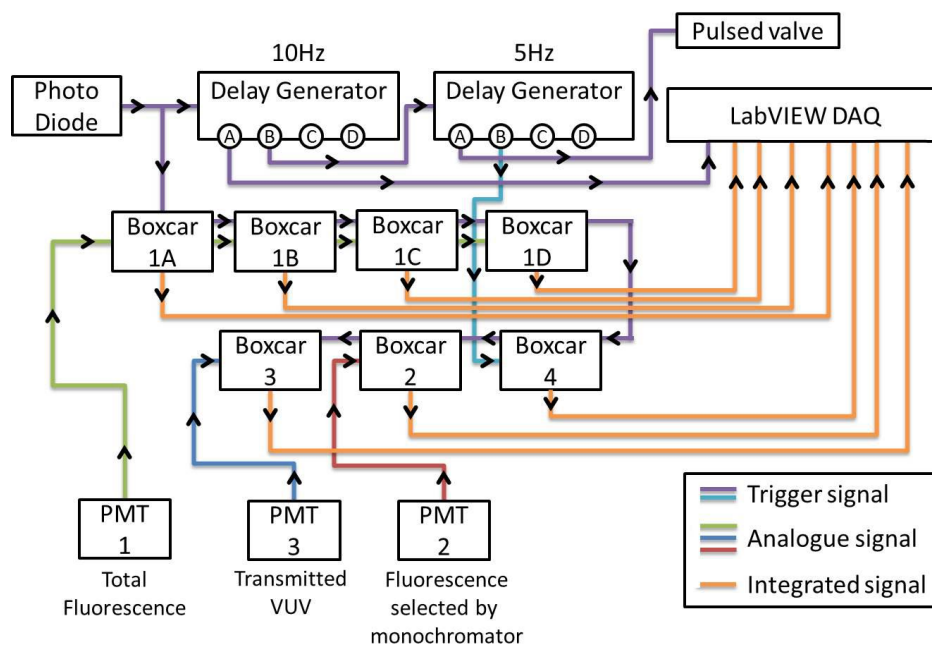
Figure 3.11: Diagram of the triggering and data acquisition system for experiments requiring laser pulses at 10Hz and gas pulses at 5 Hz.
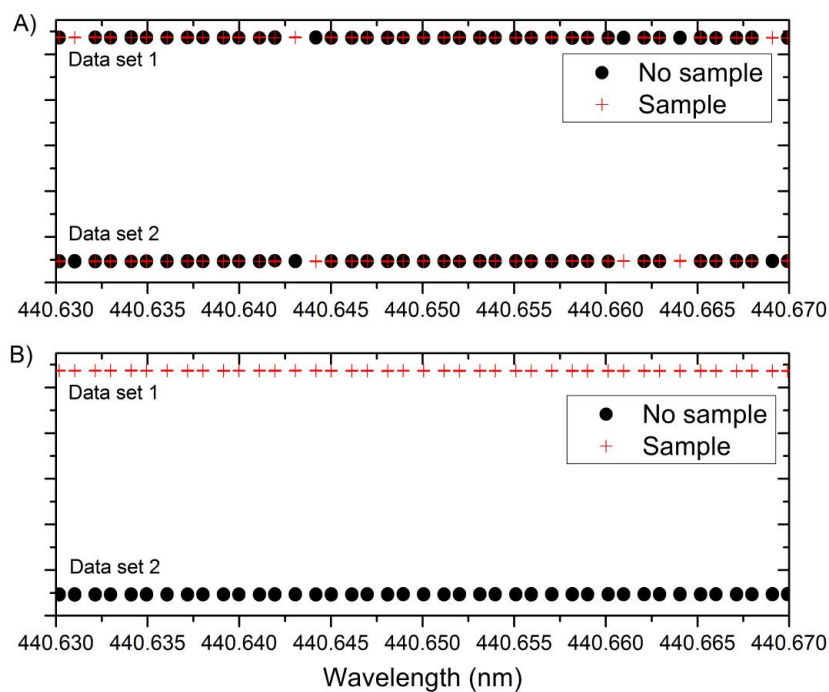
Figure 3.12: Reference signal data is split into two sets, showing A) incorrect splitting when using every second data point and B) correct splitting when using the custom program.

Chapter 4

Results and discussion

4.1   Investigation of Dye lasers

In this section, the calibration of dye lasers, the wavelength dependent index of diffraction of the fused silica prisms and wavelength reproducibility of the tuneable dye laser will be discussed.

4.1.1   Calibration of dye lasers

The calibration of dye lasers was deemed necessary in order to determine the VUV wavelengths generated. A hollow cathode lamp was used for this calibration as can be observed in Figure 3.2. Multiple wavelength regions were scanned using the tuneable dye laser (Figure 4.1). In Figure 4.1, the wavelength region selected to use for calibration was from $417\,\mathrm{nm}$ to $431.5\,\mathrm{nm}$. This was specifically selected as this is the wavelength region of interest for $X^1\Sigma^+(v''=0) - A^1\Pi(v'=4)$ excitation spectra. The calibration of the tuneable dye laser was achieved using literature values from [36] (Figure 4.2).
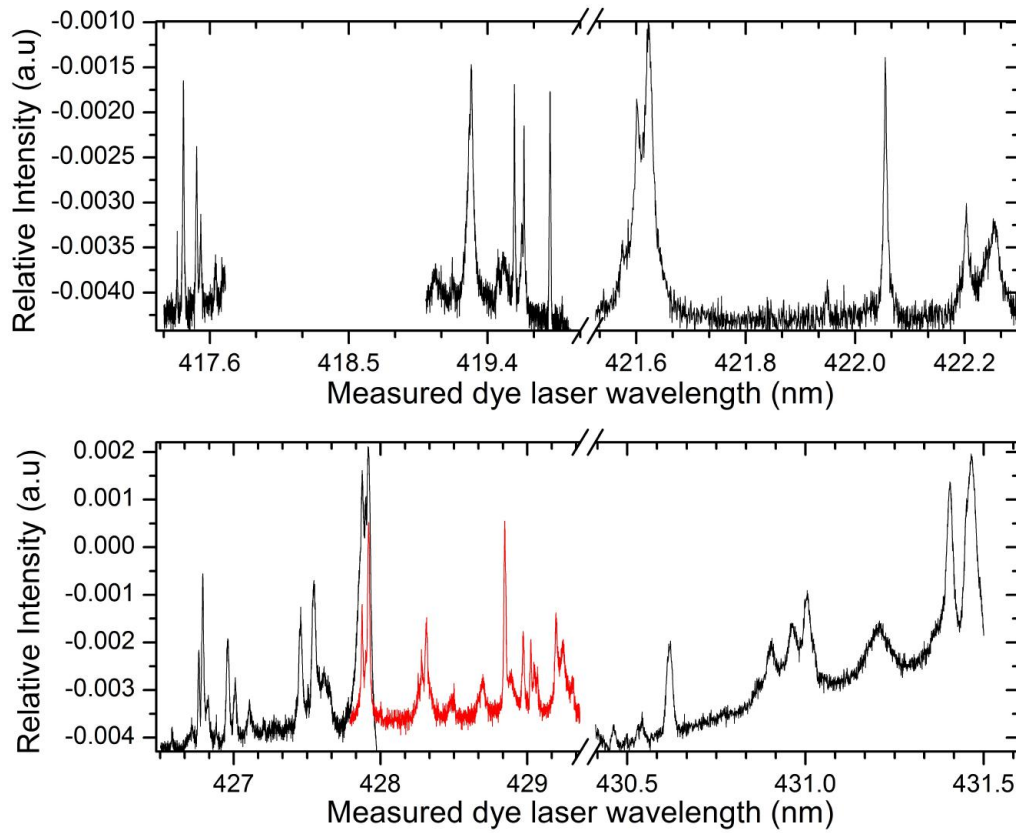
Figure 4.1: Measured optogalvanic spectra using a zirconium-neon gas hollow cathode lamp.
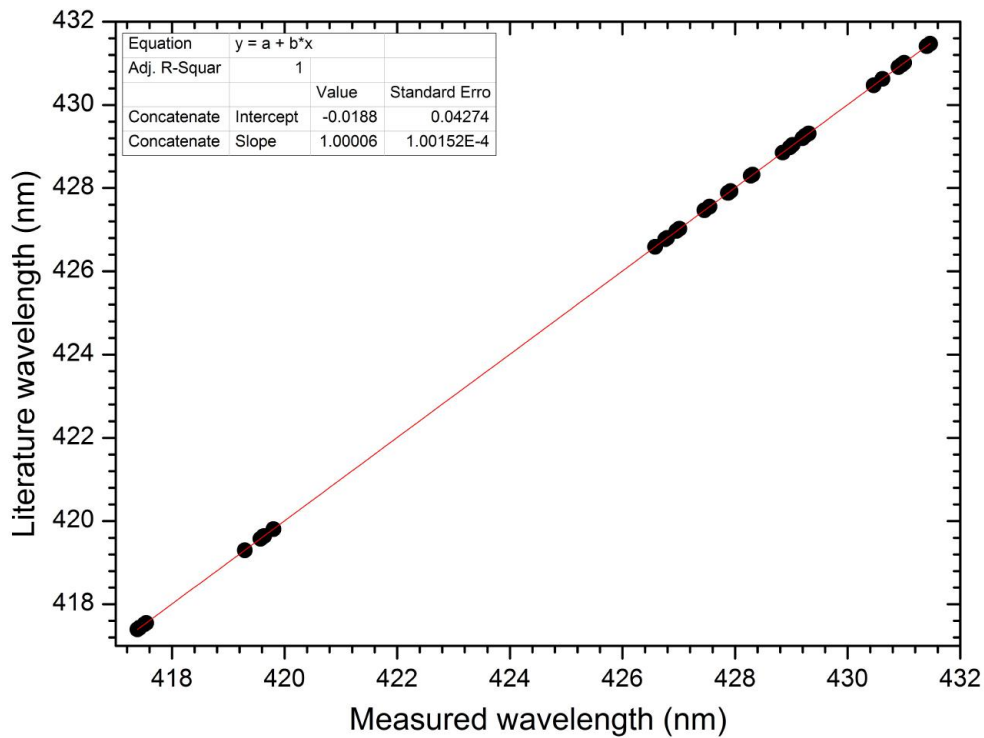
Figure 4.2: Calibration curve for tuneable dye laser.

From the results in Figure 4.2, it is clear that a gradient $(1.00006 \pm 1 \times 10^{-4})$ and an intercept $(-0.0188 \pm 0.0427\,\text{nm})$ exists which needs to be applied to the measured wavelengths. The uncertainty in the wavelength of the tuneable dye laser after calibration is $\pm0.0022\,\text{nm}$, determined from the average of the standard deviation in Figure 4.2.

Calibration for the fixed dye laser (which is set to the two-photon resonance of Mg) can not be achieved in the same manner as that of tuneable dye laser since the wavelength scanning of the fixed dye laser is not automated thus making it impossible to do spectral scans. The use of the intracavity etalon in the fixed dye laser leads to a narrower bandwidth. However, the intracavity etalon needs to be adjusted for individual wavelengths and by adjusting the intracavity etalon an alteration in the wavelength occurs.

The wavelength of the fixed dye laser was calibrated using the setup shown in Section 3.2.2.3. The monochromator was scanned over the wavelength of the fixed dye laser yielding the spectrum in Figure 4.3 (the secondary peak on the long wavelength side will be discussed in Section 4.2). By determining the wavelength of the fixed dye laser in terms of the stepper motor position of the scanning monochromator it was possible to find the correct wavelength of the fixed dye laser using the tuneable dye laser. This was achieved by firstly setting the scanning monochromator stepper motor to the position at the peak of the spectrum measured for the fixed dye laser (position A in Figure 4.3) and, secondly scanning the wavelength of the tuneable dye laser over the same wavelength range while measuring the transmission through the monochromator. This yields the second spectrum in Figure 4.3. The wavelength at which the (pre-calibrated) tuneable laser spectrum in Figure 4.3 has its peak is the wavelength at which the stepper motor position A corresponds, and therefore it is the wavelength of the fixed dye laser.
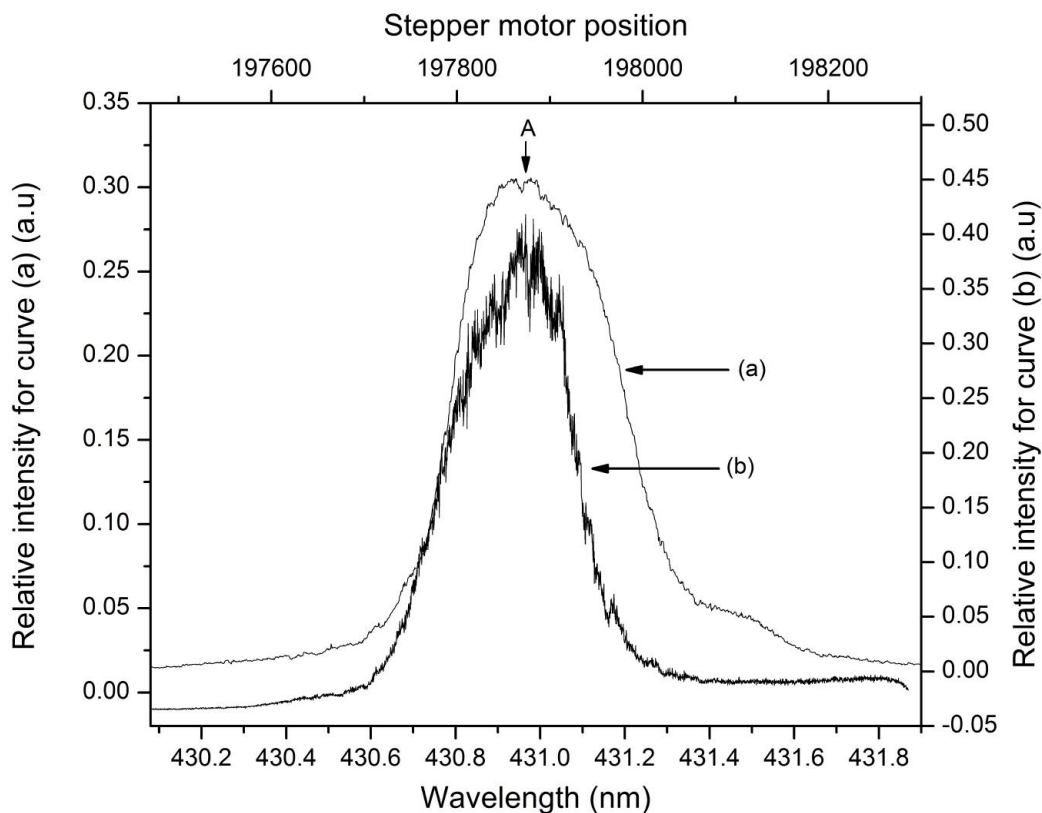
Figure 4.3: Spectra measured to calibrate the wavelength of the fixed dye laser. (a) Output spectrum of the fixed dye laser obtained by scanning monochromator. (b) Spectrum obtained by keeping the monochromator at position A and scanning the tuneable dye laser while observing its transmission through the monochromator

Using this method, it was determined that the fixed dye laser was at a wavelength of 430.9378 nm while using the intracavity etalon. The uncertainty in the wavelength value obtained by this method is estimated to be ± 0.0038 nm, determined from a combination of the uncertainty from tuneable dye laser and peak position of fixed dye laser in Figure 4.3.

If the calibrated wavelengths of the two dye lasers are used, the VUV wavelength can be calculated with an uncertainty of 0.0015 nm (at 143 nm using error propagation). When the rotationally resolved excitation spectra are analysed, the known lines of $^{12}C^{16}O$ and $^{13}C^{16}O$ are used to calibrate the CO spectra, resulting in a smaller uncertainty for the wavelengths of the unknown lines in the spectrum.

4.1.2 Wavelength dependent index of refraction

In Section 3.2.1 it was discussed how wavelength can have an impact on the focal length of optics as a result of the change in refractive index. In this section, the impact of the wavelength on the optical path will be discussed. As mentioned in Section 3.1 fused silica (SiO_2) prisms are used for steering of the incident beams and are aligned perpendicular to the incoming laser beam. In an ideal setup, the impact

of the change in refractive index would not play a role in the optical pathway as the incoming light would be perpendicular to the prism face and would be internally reflected at a 45° and would once again leave the prism perpendicular to the prism face (Figure 3.2). However, if the alignment is not perfect, the angle of incidence is not 0° and the angle at which the beam exits the prism becomes dependent on the index of refraction of the prism material and therefore of the wavelength.

To test the impact that the refractive index has on the optical path a Coherent beam view analyzer LaserCam camera was used (Section 3.1.1). The tuneable dye laser was set to different wavelengths and its beam position was recorded relative to the beam position of the fixed dye laser (Figure 4.4). In Figure 4.4, it can be
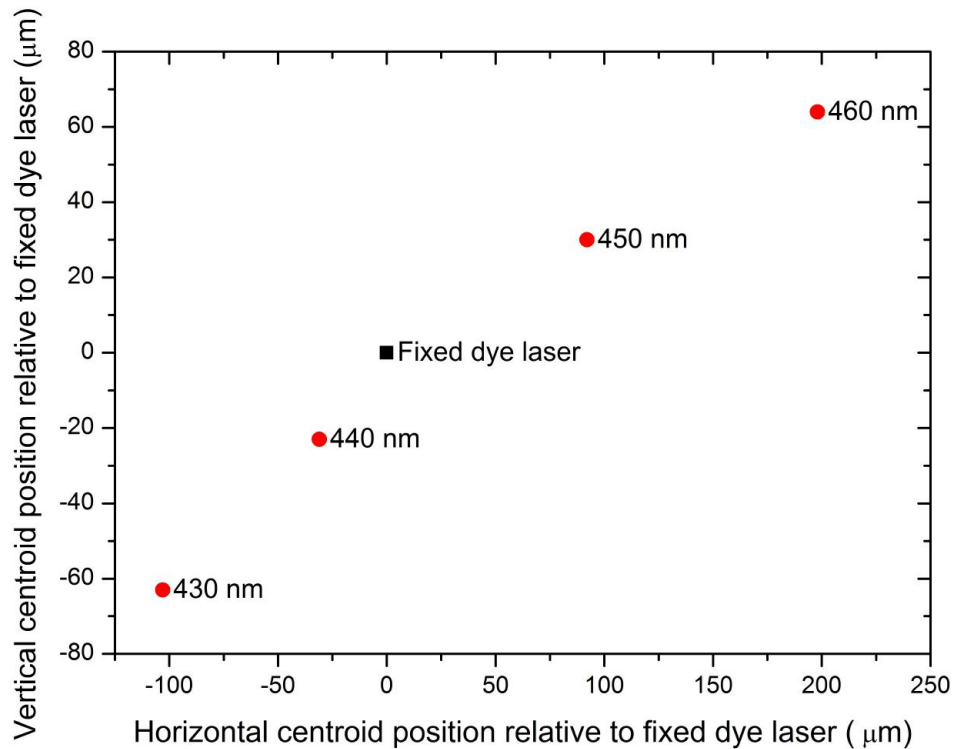
Figure 4.4: Centroid position of tuneable dye laser relative to the fixed dye laser.

observed that the position of the tuneable dye laser beam changes systematically in both the horizontal and vertical directions. There is a greater shift in the x-direction (horizontal) then in the y-direction (vertical), this is as a result of the beam only being reflected once in the vertical direction, occurring at the periscope (Figure 3.2) thus leading to a smaller shift in the beam position in comparison to the horizontal direction. In the horizontal direction, the laser beam is reflected 3 times thus, increasing the magnitude of the total deviation.

The wavelength dependent index of refraction of fused silica can be determined theoretically using the dispersion Equation (3.2.1) and constants from [37]. The refractive index of silica as a function of wavelength is shown in Figure 4.5. It can be

observed in Figure 4.5 that the refractive index does undergo a change (maximum change of 0.3%) in the wavelength region of interest.
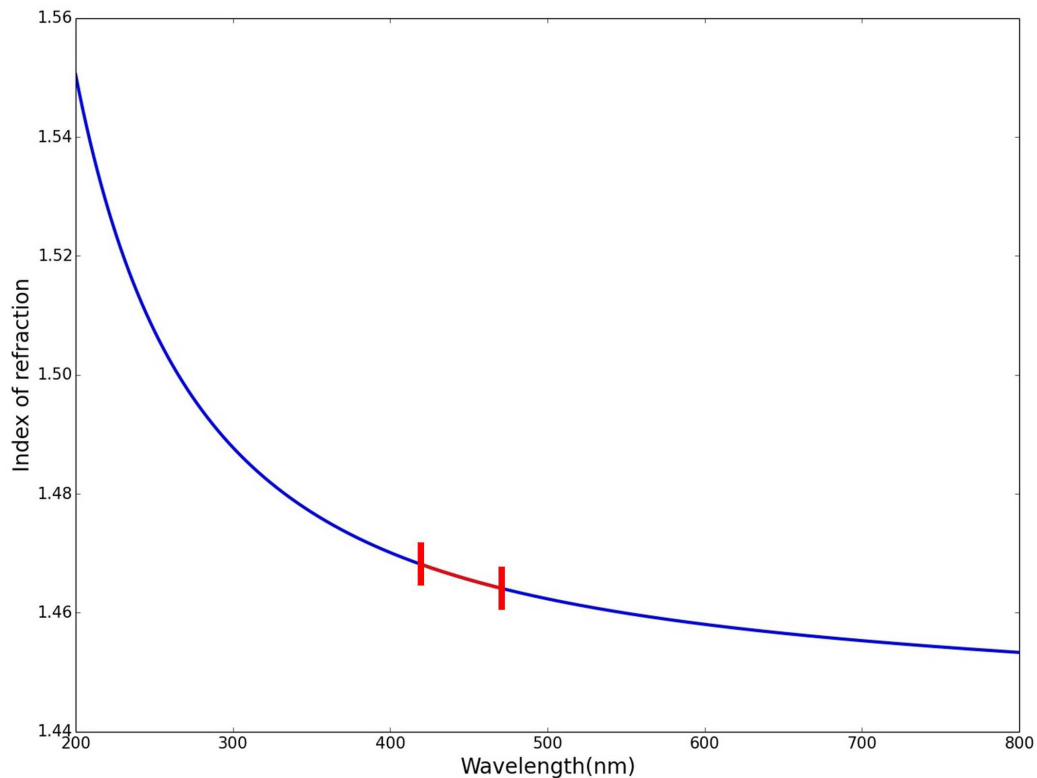
Figure 4.5: Refractive index of SiO_2 vs. wavelength (wavelength region of interest indicated in red).

The shift in beam position will impact the VUV generation as the two dye lasers need to be spatially overlapped to generate VUV light. It was possible to approximate the VUV spatial intensity profile by, approximating the two dye laser intensity profiles as Gaussian and keeping in mind that the intensity profile of the fixed dye laser needs to be squared as it contributes two photons to the generated VUV light. Using a beam waist of 150 µm, it was determined that if the spatial overlap of the two dye lasers are less than 45 µm that the VUV generation will still be above 90%, however, if the beam overlap would exceed 120 µm the VUV generation will fall below 50%. In this study, the effect of the beam shift during measurements can be ignored as the tuneable dye laser will not exceed a scanning range of 4 nm per scan thus the beam shift will remain below 45 µm. Realignment will be done when the tuneable dye laser's wavelength is changed by more than 5 nm.

4.2   Calibration of scanning monochromator

Calibration of the scanning monochromator was achieved using the setup described in Section 3.2.2.3. The laser light from the heat pipe (visible and VUV) spreads over a diffuse reflector (sandblasted glass slide) placed at the position of the gas jet to ensure uniform illumination of the monochromator's entrance slit. It was important to ensure that the light distribution on the entrance slit is as uniform as possible since the entrance slit is imaged onto the exit slit for this type of scanning monochromator. By setting the tuneable dye laser to known wavelengths and recording the spectrum of the visible laser emission and generated VUV light repeatedly it was possible to generate the spectra in Figure 4.6. It can be observed in Figure 4.6 that different slit
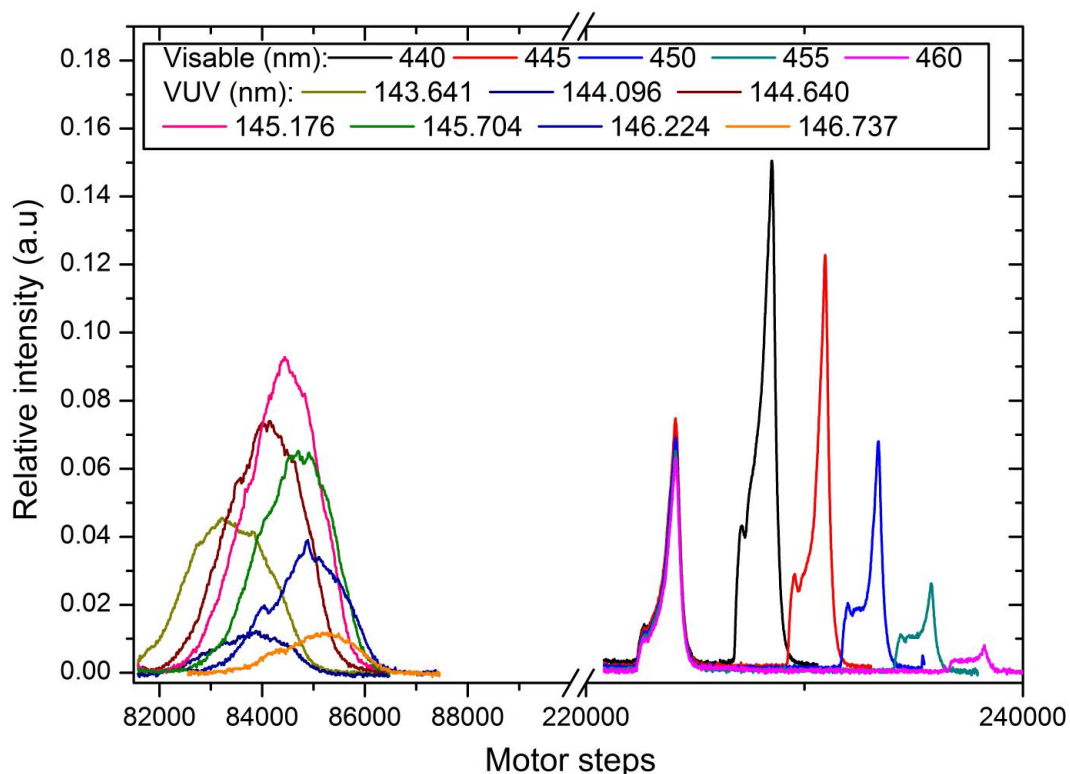
Figure 4.6: Emission spectra of the tuneable dye laser set to different wavelengths and the resulting VUV spectrum. The measurements were done with an entrance slit size of 20 µm and an exit slit size of 20 µm for visible light and an entrance slit size of 100 µm and an exit slit size of 100 µm for VUV light.

sizes were used for visible and VUV scans. This was necessary as the intensity of the VUV light was too low to measure while using an entrance and exit slit size of 20 µm. This resulted in the use of larger slit sizes for the VUV light, thus leading to the great difference in the spectral resolution between the visible and VUV light. It can be observed that the spectra for visible light has two peaks for every wavelength scanned. It was determined that these peaks are as a result of the non-uniform illumination of the monochromator entrance slit. In the visible spectra of Figure 4.6, it can be

observed that a double peak was recorded for each tuneable dye laser wavelength which was scanned by the scanning monochromator. Asymmetric structure due to scattering of strong visible laser beams in monochromator (probably producing a sharp line of light next to image of entrance slit in the plane of the exit slit).

We ignored the "plateau" of each peak and used the sharp peak on the right-hand side of each peak.
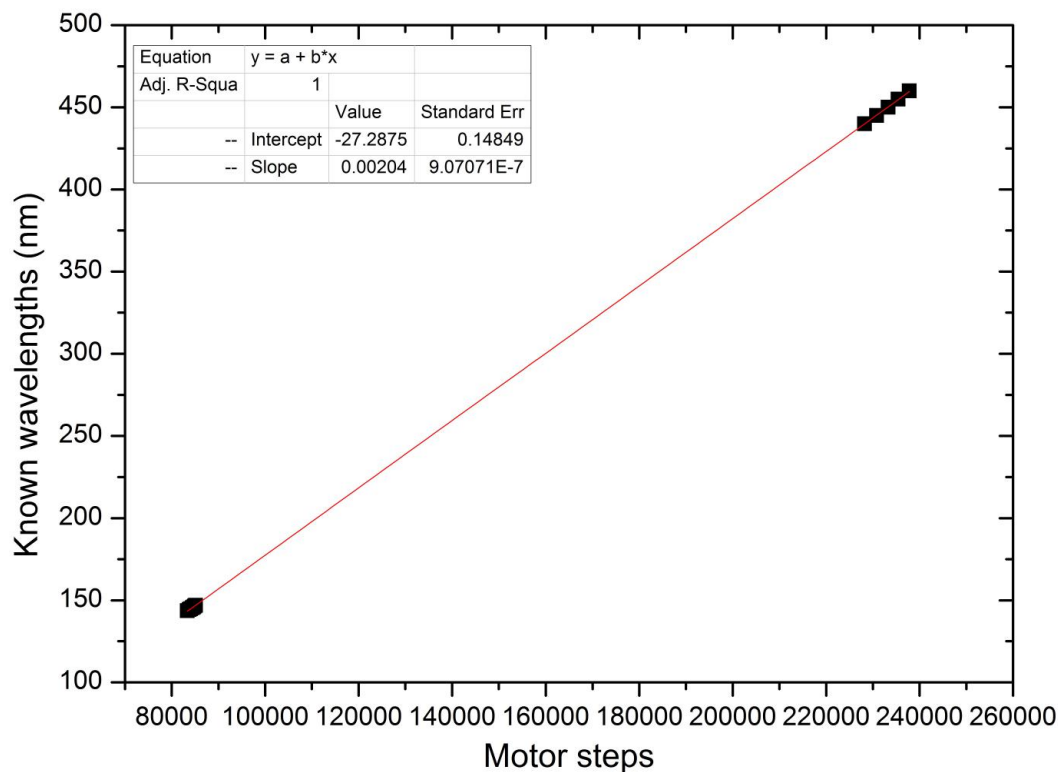
Figure 4.7: Calibration curve.

In Figure 4.7 the calibration curve using the measurements of the visible and VUV light is shown. As expected from the design of the monochromator there is a linear relation between the motor step position and the wavelength which was verified by the linear fit. Linear fits were also fitted to the measurement points in the visible and VUV light separately to investigate if it is reasonable to interpolate over this region. It was found that the slope for the data in the visible region was $0.0021\,\mathrm{nm/step}$ and the slope for the VUV region was $0.0018\,\mathrm{nm/step}$. As the slopes are in agreement with one another it is reasonable to interpolate over the missing region.

4.3   Theoretical model of the CO molecule

In Section 2.2.2 the Morse potential was discussed and how it can be used to approximate the potentials of a diatomic molecule. In this study, the CO molecule was

modelled by using constants obtained from Herzberg et al. [10] as listed in Table 4.1. Using these constants, it is possible to plot the potential curves for CO and their corresponding vibrational levels (Figure 4.8).

Table 4.1: Vibrational constants from Herzberg et al. [10].

Vibrational constants for $X^1\Sigma^+$	
$Y_{0,0}$	$0\,\mathrm{cm}^{-1}$
ω_e	$2169.81358\,\mathrm{cm}^{-1}$
$\omega_e x_e$	$13.28831\,\mathrm{cm}^{-1}$
D_e	11.226 eV
Vibrational constants for $A^1\Pi$	
$Y_{0,0}$	$6575.77\,\mathrm{cm}^{-1}$
ω_e	$1518.24\,\mathrm{cm}^{-1}$
$\omega_e x_e$	$19.40\,\mathrm{cm}^{-1}$
D_e	7.33 eV
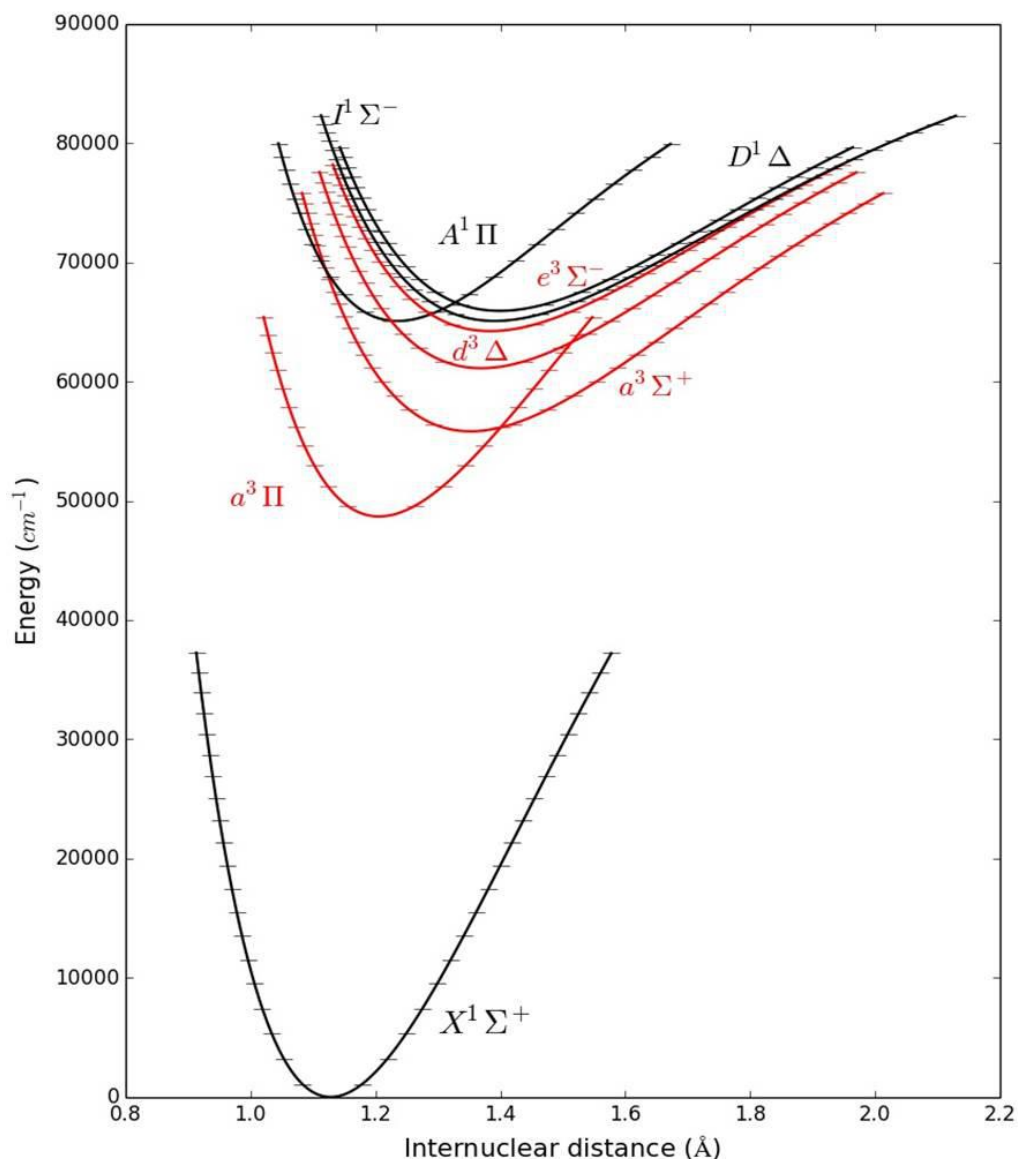
Figure 4.8: Potential curves of different electronic states of $^{12}C^{16}O$ (singlets in black and triples in red) with their corresponding vibrational levels.

The aim of the calculations was to predict the wavelengths and strengths of the vibronic transitions to the $I^1\Sigma^-$ and $D^1\Delta$ states of CO that are not well characterised in the literature. Calculations of the well-known lower lying electronic states were done and compared to our experimental fluorescence spectra. By understanding the possible electronic transitions between the different potentials it is possible to estimate the wavelength region where fluorescence will occur thus, narrowing the wavelength regions to scan during measurement of fluorescence spectra. In addition, this will aid in determining which detectors to use during measurements as the PMTs are wavelength sensitive.

4.3.1   Calculation of vibrational energies

To determine the accuracy of the Morse approximation to the vibrational energy levels, it was compared to measured values published by Krupenie [1] and calculated energies values using Dunham coefficients published by Velichko et al. [2] and Farrenq et al. [3].
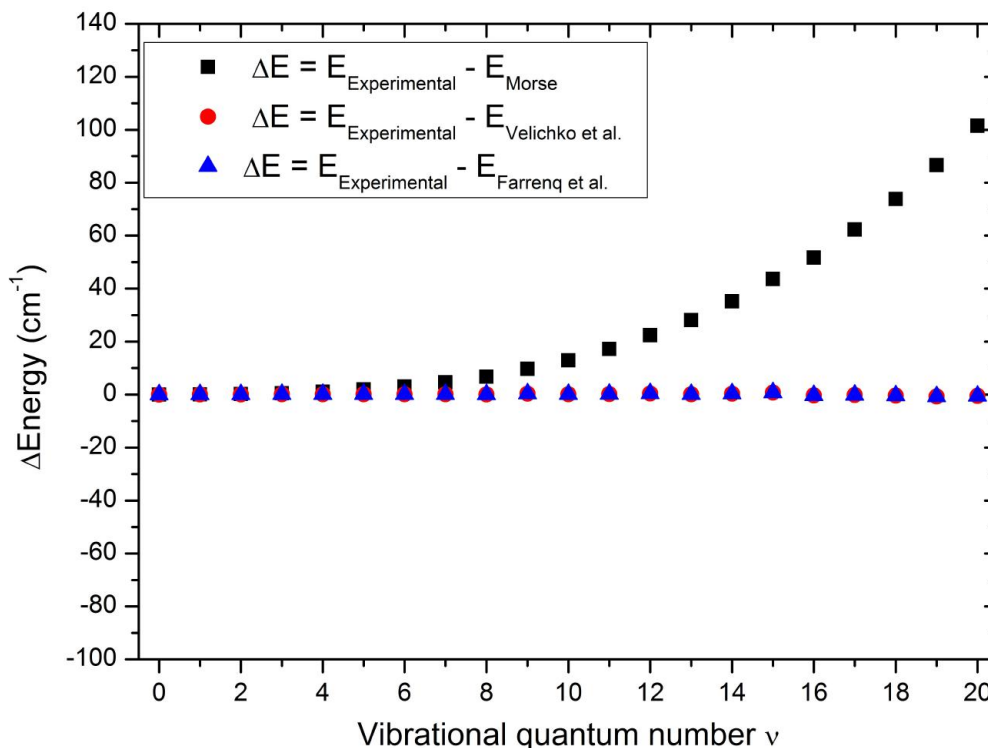
Figure 4.9: Comparison between experimental and theoretical values for vibrational energies of the $X^1\Sigma^+$ state of CO. The difference between experimentally measured energies from Krupenie [1] and energy value calculations using the Morse potential [own calculations](squares) and Dunham coefficients from Velichko et al. [2] (circles) and Farrenq et al. [3] (triangles)

It can be observed from Figure 4.9 that the Dunham coefficients method is an accurate approximation (accurate to $2\,\text{cm}^{-1}$) of the vibrational energies of CO up to $v = 20$ and will, therefore, be used when calculating the vibrational energy for CO. The Morse potential approximates the vibrational energies more accurately for low vibrational quantum numbers. However, to put this into perspective the energy derivation in Figure 4.9 of $\sim100\,\text{cm}^{-1}$ for $v = 20$ in only $\frac{100}{2000} = 5\%$ of the energy difference between subsequent energy levels. For that reason, the Morse potential is still useful for calculations of analytical wave functions.

The error of the vibrational energies of the Morse approximation increases exponentially since the Morse approximation of the vibrational energy only uses the harmonic and anharmonic vibrational constants (Equation (2.2.15)) leading to a 2nd

order polynomial equation, whereas the Dunham approximation (Equation (2.2.34)) uses a multi-order polynomial. When comparing these two approximations it can be observed that the higher order terms in the Dunham approximation will contribute more to the vibrational energies as the vibrational quantum number increases. The potential of CO behaves similar to that of the harmonic potential at low vibrational quantum number (as observed in Figure 4.13), thus it is possible for the Morse approximation to approximate these low vibrational energy levels, however at higher vibrational quantum numbers close to the dissociation energy the potential of CO and its vibrational energy levels have more anharmonic character, which the Dunham approximation provides.

4.3.2   Calulation of wave functions and Frank-Condon factors

The Morse potential is useful to calculate vibrational wave functions and Frank-Condon factors (FCFs) by analytic expressions. To calculate the Franck-Condon factors one must first calculate the wave functions for the vibrational levels in the different potentials as illustrated in Figure 4.10. The vibrational wave functions and vibrational energies in Figure 4.10 were calculated using constants from Table 4.1 and was programmed in Wolfram Mathematica 10 (Appendix B). The Franck-Condon factors are a useful tool in spectroscopy as it will give an estimation of the expected intensity distribution.
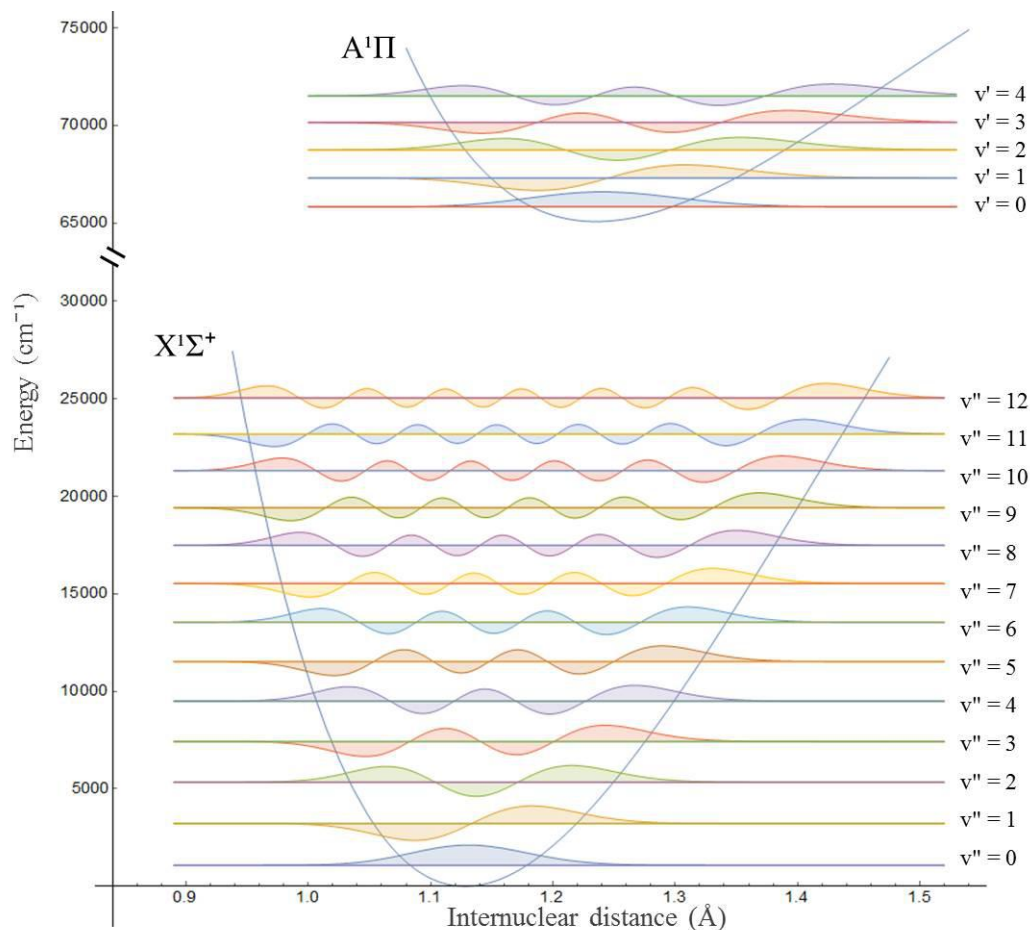
Figure 4.10: Potential curves and vibrational wave functions for the $X^1\Sigma^+$ and $A^1\Pi$ states of CO.

It can be observed from Figure 4.10 that the two defining parameters for wave function overlap are, the internuclear distance and the v-dependent form of the wave function. The Franck-Condon factors are calculated using Equation (2.2.42) in Section 2.2.4.1 and the results for $A^1\Pi - X^1\Sigma^+$ transition of CO are shown in Table 4.2, together with values from 3 literature sources ([4], [5], [6]).

The values in Table 4.2 differ depending on the set of vibrational constants and the model used. Using a different set of vibrational constants can lead to a change in the width of the potential in the internuclear space for a given vibrational level. This would result in modification of the wave function for this vibrational level which in turn would result in a different wave function overlap (Franck-Condon factor). It can be observed that in some cases values calculated in this study differs by an order of magnitude, for example, $A^1\Pi(v' = 5) - X^1\Sigma^+(v'' = 2)$ transitions. It is not possible to give a definitive answer to why this occurred, one possibility is that the two wave functions are fast oscillating so that small changes in the wave functions cause a large change in the overlap. However, it is of importance that the values in Table 4.2 follow the same trend e.g. if there is a decrease in the FCF from

Table 4.2: Franck-Condon factors for $A^1\Pi - X^1\Sigma^+$. First row entry: Own calculation using Morse potential, Second row entry: Morse potential, from Nicholls [4], Third row entry: Using Hua Potential, from Majedifar et al. [5], Forth row entry: Morse potential, from Matsumoto et al. [6]

$\frac{v''}{v'}$	0	1	2	3	4	5
0	1.084E-01	2.570E-01	2.849E-01	1.986E-01	9.866E-02	3.747E-02
	1.319E-01	2.609E-01	2.848E-01	1.963E-01	9.604E-02	3.554E-02
	1.104E-01	2.594E-01	2.868E-01	1.986E-01	9.670E-02	3.530E-02
	1.105E-01	2.584E-01	2.847E-01	1.978E-01	9.770E-02	3.670E-02
1	2.023E-01	1.585E-01	5.249E-03	6.792E-02	1.872E-01	1.889E-01
	2.161E-01	1.549E-01	3.058E-03	7.644E-02	1.931E-01	1.857E-01
	2.132E-01	1.571E-01	3.600E-03	7.620E-02	1.954E-01	1.872E-01
	2.096E-01	1.571E-01	4.200E-03	7.180E-02	1.900E-01	1.874E-01
2	2.159E-01	1.871E-02	7.677E-02	1.226E-01	1.101E-02	4.195E-02
	2.300E-01	1.218E-02	9.013E-02	1.161E-01	5.083E-03	5.718E-02
	2.293E-01	1.350E-02	8.810E-02	1.167E-01	5.000E-03	5.950E-02
	2.240E-01	1.520E-02	8.370E-02	1.195E-01	7.700E-03	4.970E-02
3	1.751E-01	9.922E-03	1.176E-01	5.099E-03	7.285E-02	9.723E-02
	1.813E-01	2.049E-02	1.170E-01	6.454E-04	8.957E-02	8.417E-02
	1.826E-01	1.890E-02	1.169E-01	8.000E-04	8.970E-02	8.350E-02
	1.791E-01	1.520E-02	1.180E-01	2.000E-03	8.200E-02	9.060E-02
4	1.210E-01	6.217E-02	5.050E-02	3.669E-02	8.133E-02	1.010E-04
	1.188E-01	8.729E-02	3.443E-02	5.763E-02	6.656E-02	6.171E-03
	1.206E-01	8.510E-02	3.540E-02	5.630E-02	6.630E-02	6.600E-03
	1.204E-01	7.580E-02	4.180E-02	4.800E-02	7.390E-02	2.300E-03
5	7.576E-02	9.955E-02	2.611E-03	8.463E-02	6.453E-03	6.391E-02
	6.885E-02	1.230E-01	3.236E-04	9.125E-02	1.384E-05	8.236E-02
	7.040E-02	1.221E-01	2.000E-04	9.030E-02	0.000E+00	8.210E-02
	7.230E-02	1.132E-01	2.000E-04	8.970E-02	1.500E-03	7.520E-02

$A^1\Pi(v' = 0) - X^1\Sigma^+(v'' = 0)$ to $A^1\Pi(v' = 0) - X^1\Sigma^+(v'' = 1)$ it needs to be present in all models. This is the case as illustrated in Figure 4.11, and similar for the other cases.

4.3.3 Comparing the wave functions of the Morse and Harmonic potential

As mentioned in Section 2.2.2.4 there is a mathematical difference between the Morse and harmonic potentials, as observed from Figure 4.12. It can be observed from Figure 4.12 that the Morse potential behaves similar to the harmonic oscillator close to the turning point of the potential, this will become clearer later in this section when using Franck-Condon factors. It is important to note that $X^1\Sigma^+$ is one of the more harmonic potentials of CO. However, by applying the harmonic approximation to $X^1\Sigma^+$ potential it will be shown that even at low vibrational levels that the
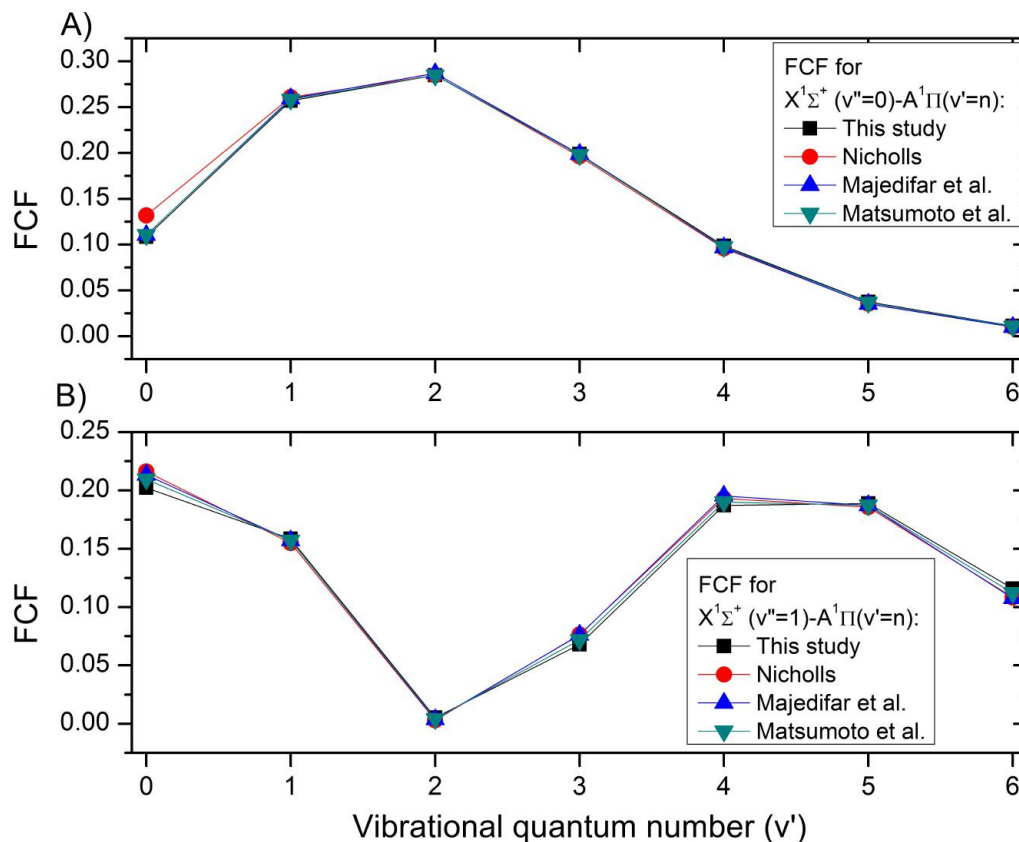
Figure 4.11: Comparing FCFs from different studies: Own calculation using Morse potential (black), Nicholls [4] using Morse potential (red), Majedifar et al. [5] using Hua Potential (blue) and Matsumoto et al. [6] using Morse potential (green). A) $X^1\Sigma^+(v''=0) - A^1\Pi(v'=n)$ transitions and B) $X^1\Sigma^+(v''=1) - A^1\Pi(v'=n)$ transitions.

harmonic approximation is not an effective approximation for the $X^1\Sigma^+$ potential. This raises the question of how anharmonic the potentials of CO are compared to that of a harmonic potential? This question can be answered by investigating the overlap between the harmonic wave function and Morse wave function which will give a measure of how harmonic the Morse potential is for a given vibrational level and this is given by:

$$\text{Wave function overlap} = \left[\int_0^\infty \psi_n^{Harmonic}(r)^\dagger \psi_n^{Morse}(r) \right]^2 dr. \qquad (4.3.1)$$

The larger this overlap is, the more the wave functions of the harmonic and Morse potentials agree, indicating harmonic nature.
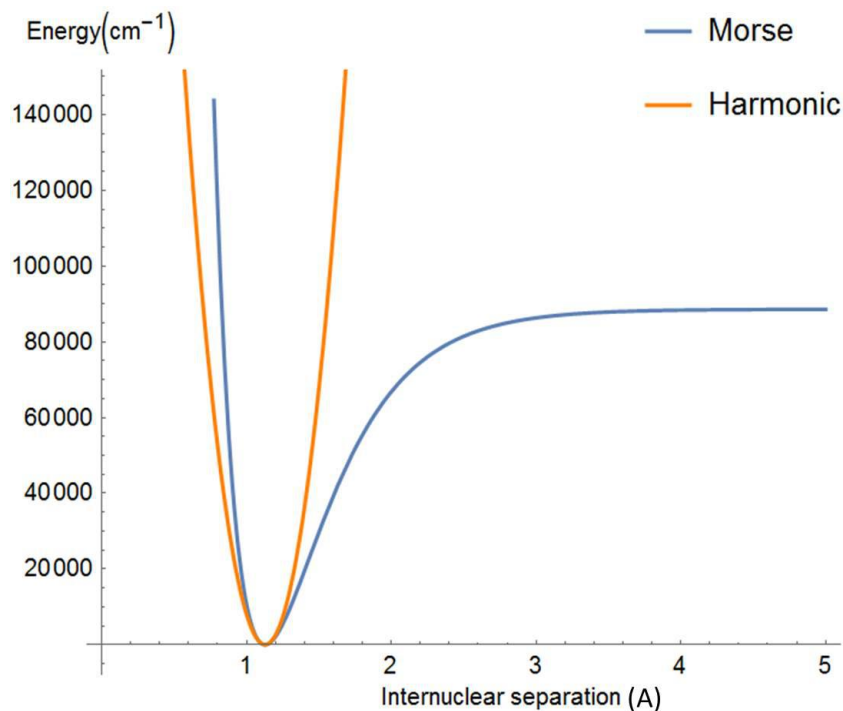
Figure 4.12: Illustrates Harmonic potential (orange) and Morse potential (blue).
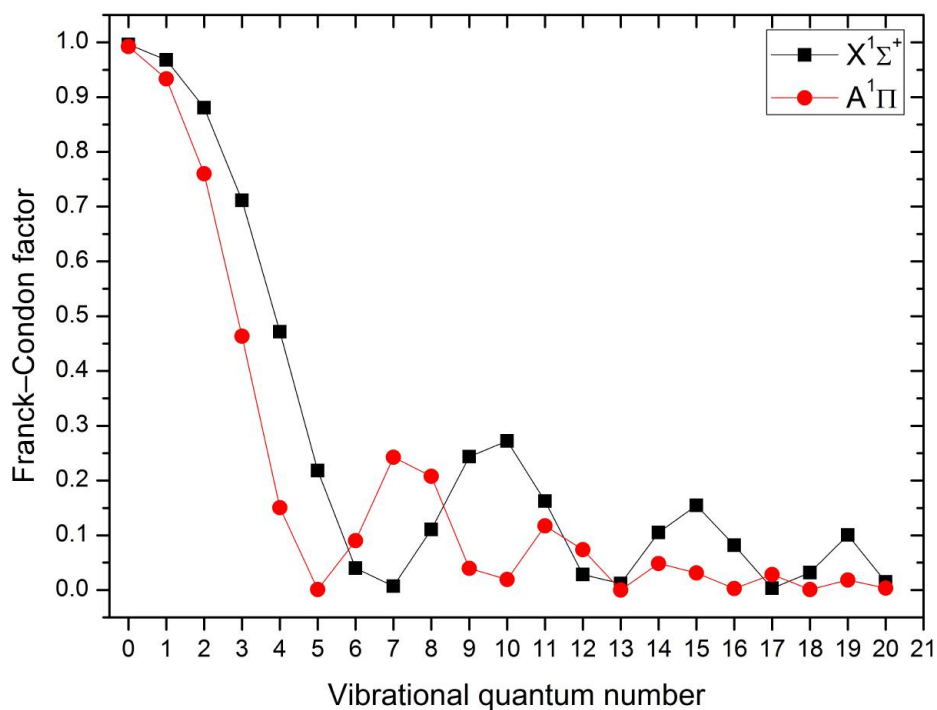
Figure 4.13: Franck-Condon factors between harmonic and anharmonic potentials for the electronic ground state $X^1\Sigma^+$ and the first singlet excited state $A^1\Pi$.

It can be observed from Figure 4.13 that the spatial overlap of the harmonic and Morse wave functions for the $A^1\Pi$ potential is significantly lower (for $v > 1$) compared to the $X^1\Sigma^+$ potential, thus indicating that the $A^1\Pi$ potential is more anharmonic than the $X^1\Sigma^+$ potential.

It can additionally be observed that the wave function overlap between the harmonic and anharmonic potentials is only large for the first three vibrational levels. At the 7th vibrational level for the $X^1\Sigma^+$ electronic state, the spatial overlap of the harmonic and Morse wave functions tend to zero. The harmonic and Morse wave functions for the 7th vibrational level is shown in Figure 4.14.A where it can be observed that a 90° spatial phase shift between the wave functions exists. This phase shift results in the spatial overlap of the harmonic and Morse wave functions tending to zero. The phase shift is as a result of the difference in the form of the harmonic and Morse potential at this point. It is important to note that when calculating the spatial overlap between two wave functions that the wave functions are firstly multiplied then integrated over space.

The spatial overlap of the harmonic and Morse wave functions increases towards the 10th vibrational level (Figure 4.13) for the $X^1\Sigma^+$ electronic state. The increase in the spatial overlap is as a result of a 180° spatial phase shift between the harmonic and Morse wave functions at $v = 10$ as can be observed in Figure 4.14.B. The spatial phase shift is once again a result of the difference in the form of the harmonic and Morse potential at this point.
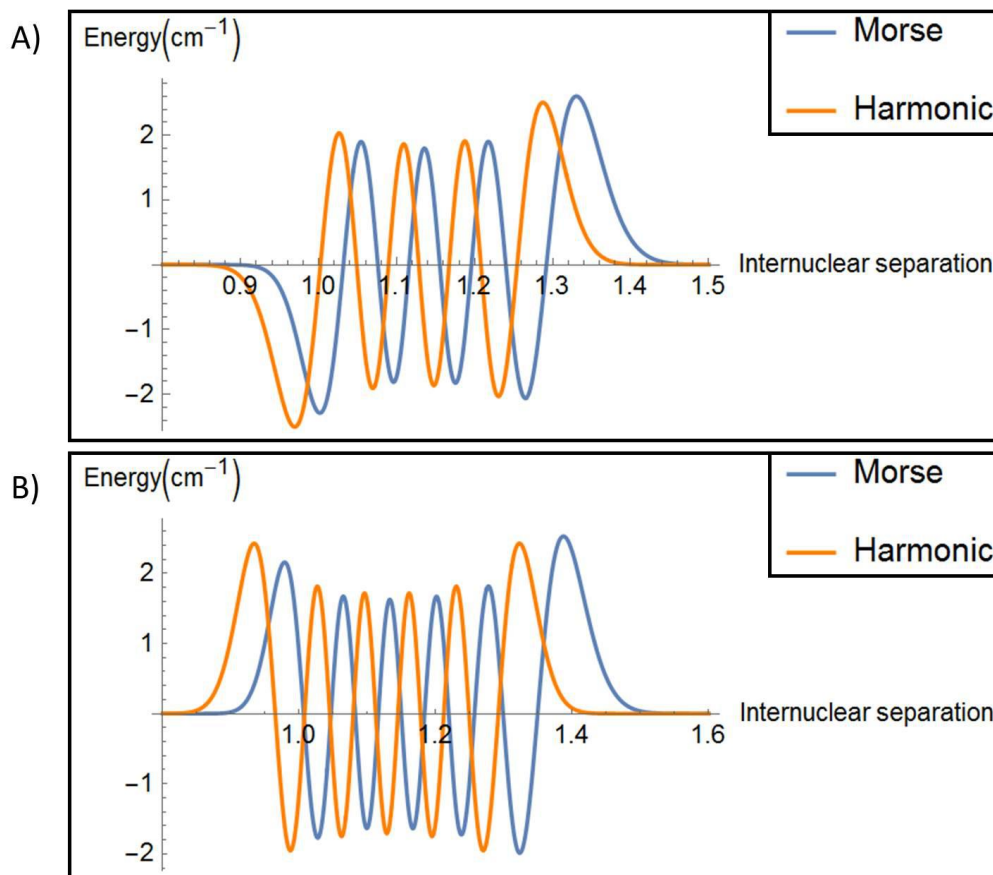
Figure 4.14: Harmonic wave functions indicated in orange and Morse (anharmonic) wave functions indicated in blue for A) $X^1\Sigma^+(v''=7)$ and B)$X^1\Sigma^+(v''=10)$.

4.4 Vibrationally resolved fluorescence spectra of Carbon Monoxide

Previously in our laboratory excitation spectra of CO in a supersonic gas jet was measured. The incident VUV wavelength is scanned to excite individual rovibronic transitions and the total fluorescence was measured. In this study, fluorescence spectra of CO in a supersonic gas jet was measured for the first time in our laboratory. The excitation wavelength (VUV wavelength) is kept constant, whilst the scanning monochromator is used to record the fluorescence spectrum, for example Figure 4.15. In Figure 4.15.A the fluorescence spectra of the $^{12}C^{16}O$ isotope after excitation of the $R(1)$, $R(0)$, $P(5)$ and $P(5)$ rovibronic transitions in the $X^1\Sigma^+(v''=0)-A^1\Pi(v'=3)$ band are shown (The experimental setup for these measurements are discussed in Section 3.2.).
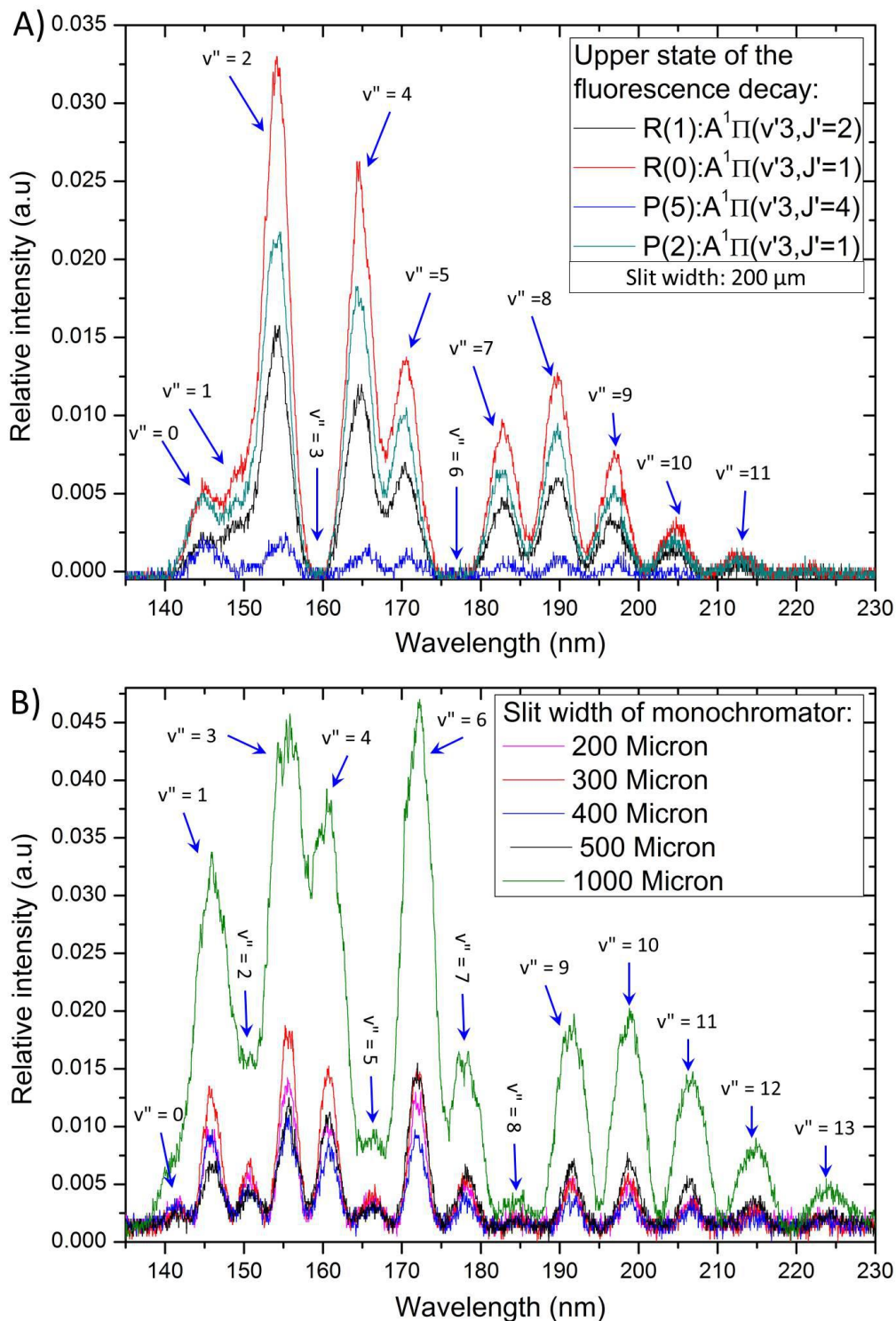
Figure 4.15: Fluorescence spectra recorded after excitation of the following rovibronic transitions: A) the $R(1)$, $R(0)$, $P(5)$ and $P(5)$ transitions in the $X^1\Sigma^+(v''=0) - A^1\Pi(v'=3)$ band of $^{12}C^{16}O$ and B) the $R(0)$ transition in the band $X^1\Sigma^+(v''=0) - A^1\Pi(v'=4)$ of $^{12}C^{16}O$. The vibrational quantum numbers of the ground state $X^1\Sigma^+(v'')$ to which the molecules return by fluorescence are indicated. The slit widths (both entrance and exit slits have the same width) are indicated.

When analysing the transitions wavelengths in Figure 4.15 we conclude that for a vibronic excitation to the $A^1\Pi(v' = 3)$ state, no vibrational relaxation in the $A^1\Pi(v' = 3)$ state (as illustrated in Figure 4.16) takes place. This is the result of the low temperature, as well as collision-free conditions in the gas jet.
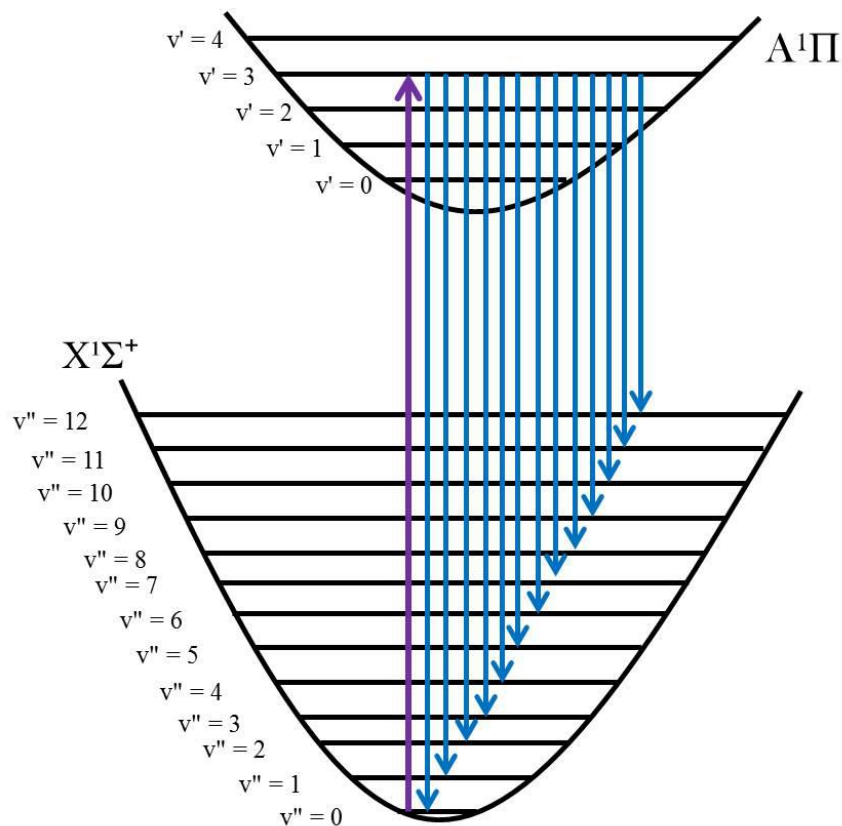
Figure 4.16: Illustration of the fluorescence decay for $A^1\Pi(v' = 3) - X^1\Sigma^+(v'' = n)$.

In Figure 4.16 the transitions associated with the observed fluorescence bands following excitation from the $X^1\Sigma^+(v'' = 0)$ vibronic state to the $A^1\Pi(v' = 3)$ vibronic state is illustrated. De-excitation to different vibrational states in the ground state potential $(X^1\Sigma^+)$ occurs. The scanning monochromator can not distinguish between different rovibronic transitions as the spectral resolution of the monochromator is lower than the spacing of the rovibronic transitions.

It can be observed from Figure 4.15 that the peak separation seems to increase from shorter to longer wavelengths. This is simply the result of the $\frac{1}{\lambda^2}$ scaling when $\Delta\nu$ is converted to $\Delta\lambda$. The vibrational level separation is very similar for the different v-values (becoming slightly closer together at high v due to anharmonicity), but the $\Delta\lambda$ values increase with λ. It can also be observed that some of the electronic vibrational transitions are too weak to measure or do not occur ($v'' = 3$ and $v'' = 6$).

It was also possible to measure the fluorescence after excitation of the $X^1\Sigma^+(v'' = 0) - A^1\Pi(v' = 4)$ transition by changing the dye agent used in the tuneable dye laser

from Coumarin 440 to Stilbene 420 which allows for efficient VUV generation in this wavelength range. These results can be observed in Figure 4.15.B.

For these measurements, the excitation wavelength was kept fixed at the $X^1\Sigma^+(v''=0, J''=0)-A^1\Pi(v'=4, J'=1)$ transition and the slit size of the scanning monochromator was altered as indicated in Figure 4.15.B. Both entrance and exit slits were set to the same width to investigate at which slit width it will still be possible to distinguish between the different vibrational transition as this will be important in later sections. It can be observed from Figure 4.15.B that it is still possible to distinguish between the $A^1\Pi(v'=4)-X^1\Sigma^+(v''=3)$ and $A^1\Pi(v'=4)-X^1\Sigma^+(v''=4)$ transitions at a slit size of 1000 µm although the smaller peaks (e.g. $v''=0,2,5,8$) are not clearly resolved. It can also be observed that with a smaller slit size there is an increase in spectral resolution but a decrease in the intensity and the opposite is true for a larger slit size. Furthermore, it was possible to measure all transitions up to $A^1\Pi(v'=4)-X^1\Sigma^+(v''=13)$ including weaker transition.

4.4.1   Peak analysis

To determine which transitions are occurring the peak positions of the fluorescence spectra were compared to the calculated transition wavelength values for the transitions $A^1\Pi(v'=3)-X^1\Sigma^+(v''=n)$ and $A^1\Pi(v'=4)-X^1\Sigma^+(v''=n)$. The relative intensities of the peaks can be approximated using Franck-Condon factors (Section 2.2.4.1) as these factors are related to the transition probability (see Table 4.3). The "calculated wavelengths" values in Table 4.3 were calculated using the Dunham expansion coefficients from Velichko et al. [2]. The Franck-Condon factors given in Table 4.3 are calculated using the Morse potential.

Table 4.3: Table of results for the $A^1\Pi(v' = 3) - X^1\Sigma^+(v'' = n)$ and $A^1\Pi(v' = 4) - X^1\Sigma^+(v'' = n)$ fluorescence transitions. FCF stands for Frank-Condon factor.

$v'' = n$	Calculated Wavelength (nm)	Measured Wavelength (nm)	FCF	Relative measured intensity (a.u)
Measured from $A^1\Pi(v' = 3) - X^1\Sigma^+(v'' = n)$
0	144.78	144.60	0.18	0.0075
1	149.41	149.24	0.0099	0.020
2	154.30	154.05	0.12	0.11
3	159.44	Not observed	0.0051	-
4	164.86	164.59	0.073	0.075
5	170.59	170.78	0.097	0.046
6	176.65	Not observed	0.0063	-
7	183.06	183.34	0.042	0.032
8	189.87	189.84	0.14	0.036
9	197.09	196.81	0.16	0.018
10	204.78	204.71	0.10	0.0082
11	212.96	213.08	0.050	0.0032
Measured from $A^1\Pi(v' = 4) - X^1\Sigma^+(v'' = n)$
0	141.99	141.97	0.11	0.0017
1	146.43	146.45	0.087	0.0077
2	151.11	151.16	0.034	0.0039
3	156.05	156.04	0.058	0.012
4	161.24	161.28	0.067	0.0090
5	166.71	166.74	0.0062	0.0021
6	172.50	172.48	0.098	0.011
7	178.61	178.65	0.051	0.0033
8	185.08	185.18	0.0027	0.00054
9	191.93	191.94	0.089	0.0036
10	199.22	199.24	0.17	0.0035
11	206.96	207.06	0.13	0.0018
12	215.20	215.21	0.068	0.0013
13	223.99	224.02	0.026	0.0021

In Figures 4.17.A & 4.17.B the fluorescence spectra are graphed with the FCF's plotted versus calculated wavelength as an overlay. In Figure 4.17.A it can be observed that transitions $A^1\Pi(v' = 3) - X^1\Sigma^+(v'' = 3)$ and $A^1\Pi(v' = 3) - X^1\Sigma^+(v'' = 6)$ are not observed as a result of their low transition probability given by the Frank-Condon factors (0.0051 and 0.0062 respectively). In the $A^1\Pi(v' = 4) - X^1\Sigma^+(v'' = n)$ band the expected peaks are all observable although some have equally small FCF values of the $v'' = 5$ and $v'' = 8$ transitions due to the larger slit width used.

It can be further observed that for both the spectra the peak associated with de-excitation to $X^1\Sigma^+(v'' = 0)$, the intensity measured is lower than expected when compared to the Franck-Condon factors. This is the result of self-absorption occurring which will be discussed in more detail in Section 4.5.
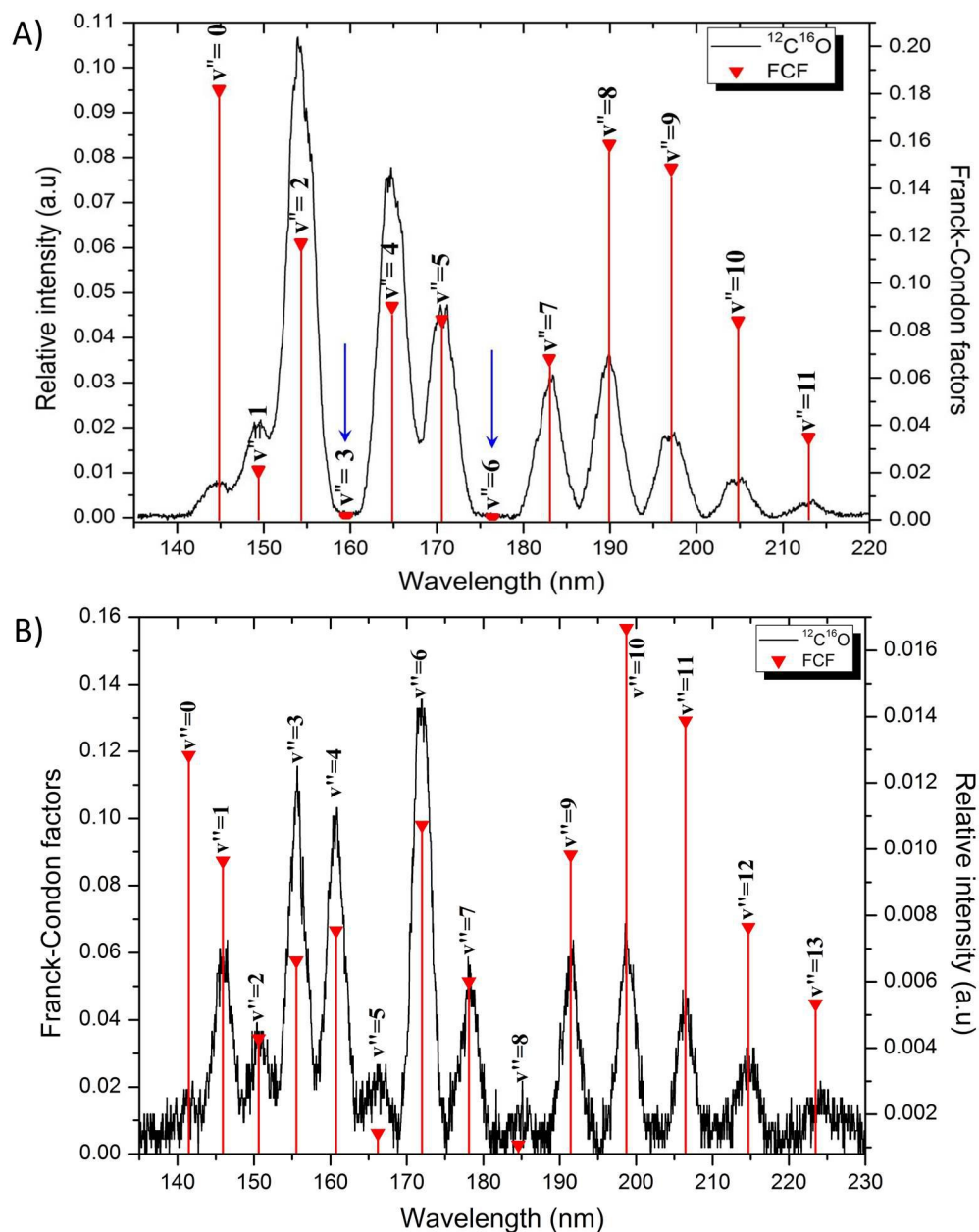
Figure 4.17: Fluorescence of $^{12}C^{16}O$ with corresponding Franck-Condon factors for the A) $A^1\Pi(v' = 3, J' = 1) - X^1\Sigma^+(v'' = n)$ and B)$A^1\Pi(v' = 4, J'' = 1) - X^1\Sigma^+(v'' = n)$ fluorescence decay transitions, measured with slit widths of $200\,\mu m$ and $500\,\mu m$ respectively

It can be observed from Figures 4.17.A & 4.17.B that not all the Franck-Condon factors agree with the measured peak intensities in particular for higher v'' values. This is as result of the molecule vibrating in such a way that the center of mass position shifts leading to a less accurate approximation of the peak intensities when using the Condon approximation. An additional approximation can be used to solve

this problem namely the r-centroid approximation (see Section 2.2.4.2). By using Gaussian fits the areas of the spectral peaks were obtained. By normalizing to a specific peak in each spectrum ($A^1\Pi(v' = 3) - X^1\Sigma^+(v'' = 2)$ and $A^1\Pi(v' = 4) - X^1\Sigma^+(v'' = 3)$ respectively) it is possible to compare different measurements. This is necessary since the absolute intensities of different measurements varied. The Morse approximation was used to determine the corresponding wave functions used to calculate the r-centroid (r) values using Equation (2.2.44). The calculated r-centroid values can be found in Table A.2 in the appendix. By making the electron transition moment ($R_e^2(r)$) the subject, Equation (2.2.43) is given by:

$$R_e\left(r_{v'v''}\right) = \sqrt{\frac{P_{v'v''}}{q_{v'v''}}}, \tag{4.4.1}$$

where the transition probability ($P_{v'v''}$) is the normalized areas of measured peaks, $q_{v'v''}$ is the Franck-Condon factors given in Table A.2 and r is the r-centroid given by Equation (2.2.44).
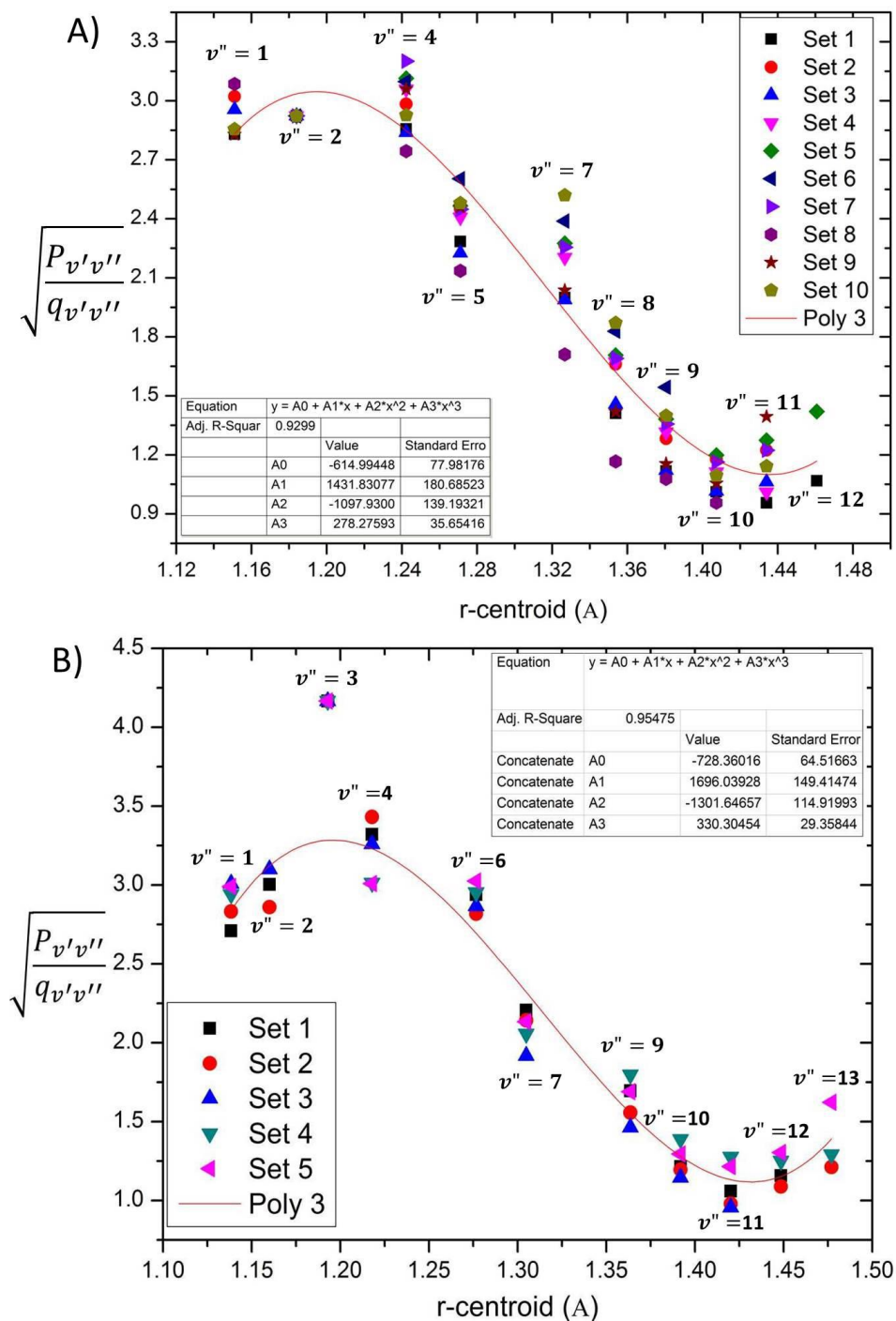
Figure 4.18: Electronic moment approximation for measured A) $A^1\Pi(v' = 3) - X^1\Sigma^+(v'' = n)$ and B) $A^1\Pi(v' = 4) - X^1\Sigma^+(v'' = n)$ transition.

When R_e (r) is plotted versus r (Figures 4.18.A & 4.18.B) the polynomial relationship between the r-centroid and the electronic moment (Figures 4.18.A & 4.18.B), which is expected when considering Equation (2.2.45), is obtained. By fitting a 3rd

order polynomial to Figure 4.18.A it is possible to extract the r-centroid coefficients for the $A^1\Pi(v' = 3) - X^1\Sigma^+(v'' = n)$ fluorescence band and these were found to be:

$$R_e\left(r\right) = R_0\left(1 - 2.3282r + 1.7853r^2 - 0.4525r^3\right) \qquad (4.4.2)$$

$$\text{with} \quad R_0 = -614.994\text{Å}^{-2}.$$

By fitting a 3rd order polynomial to Figure 4.18.B it is possible to extract the r-centroid coefficients for the $A^1\Pi(v' = 4) - X^1\Sigma^+(v'' = n)$ fluorescence band and these were found to be:

$$R_e\left(r\right) = R_0\left(1 - 2.3286r + 1.7871r^2 - 0.4535r^3\right) \qquad (4.4.3)$$

$$\text{with} \quad R_0 = -728.360\text{Å}^{-2}.$$

It can be observed in Figure 4.18.B that the $A^1\Pi(v' = 4) - X^1\Sigma^+(v'' = 3)$ transition is an outlier and it was therefore not used for the fit. In addition, $A^1\Pi(v' = 4) - X^1\Sigma^+(v'' = 5)$ and $A^1\Pi(v' = 4) - X^1\Sigma^+(v'' = 8)$ was also not used for the fit as these are weak peaks and the areas of these peaks could not be determined accurately. Unfortunately, it was not possible to compare these results directly with the literature as no 3rd order polynomials describing the electronic moment could be found. However, 1st and 2nd order polynomials for the electronic moment exists and was compared to that of this study (Figure 4.19).

It is important to note that the literature values given by Field et al. was determined using the following transitions $A^1\Pi(v' = 4, 5, 5, 6, 6, 7, 7, 10, 11, 16)$-$X^1\Sigma^+(v'' = 12, 12, 3, 13, 14, 14, 15, 16, 17, 19)$ and the literature values given by DeLoen et al. was determined using the following transitions $A^1\Pi(v' = 22) - X^1\Sigma^+(v'' = 21 - 13)$. This is of importance as the paper published by Fraser et al. [29] states that the electronic transition moment is transition dependent, meaning that even if the results hold for the same r-centroid value range, it will differ if different vibronic transitions were used to determine the electronic transition moment. The fact that the electronic transition moment is transition dependent may clarify why there exists a deviation between the studies done by Field et al., DeLoen et al. and this study. Additionally, the studies done by Field et al. and DeLoen et al. where firstly not conducted in a collision free environment and secondly these studies did not take self-absorption into account when calculating the coefficients of the electronic transition moment. In this study the effect of self-absorption could be ignored for most vibrational transition as the only level that is populated is the ground vibrational level ($X^1\Sigma^+(v'' = 0)$).
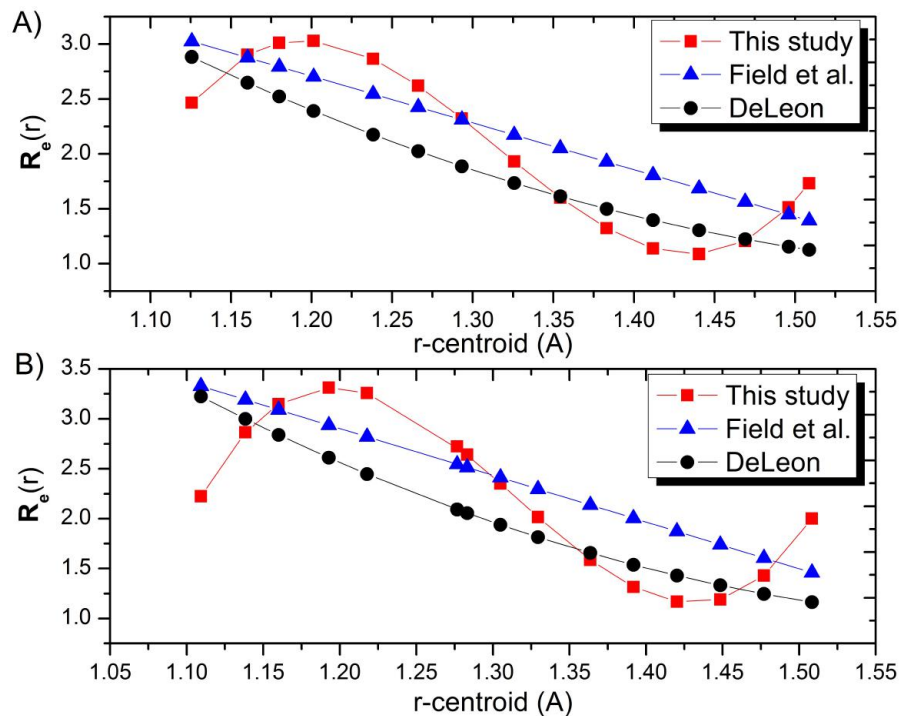
Figure 4.19: Comparison of r-centroid approximation for the A) $A^1\Pi(v' = 3) - X^1\Sigma^+(v'' = n)$ band and B) $A^1\Pi(v' = 4) - X^1\Sigma^+(v'' = n)$ band calculated in this study (red, 3rd order polynomial), by DeLeon [7] (black, 2nd order polynomial) and by Field et al. [8] (blue, 1st order polynomial).

Using these results it is possible to recalculate the transition probabilities of the transitions as can be observed in Figures 4.20.A & 4.20.B.
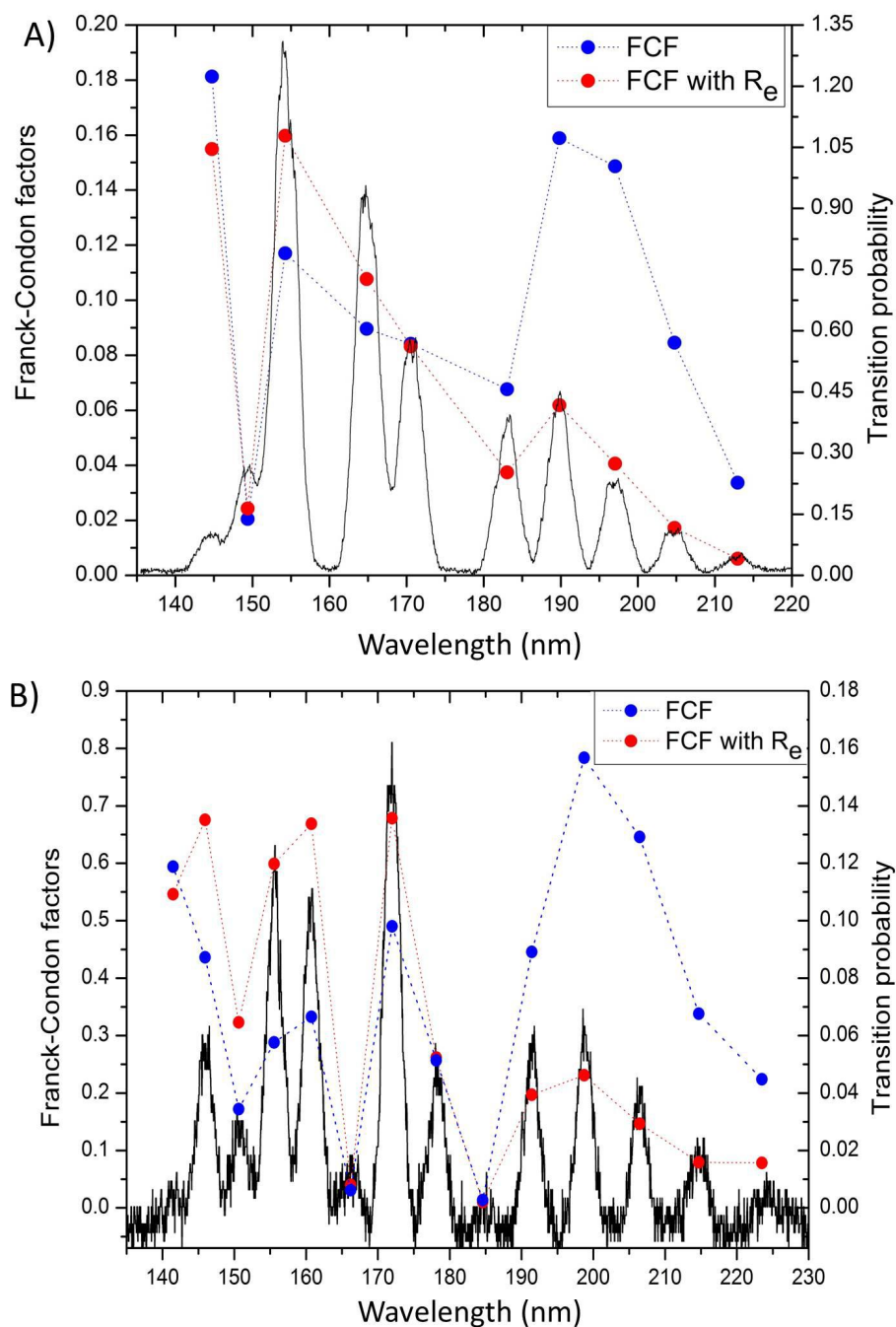
Figure 4.20: Comparison between the r-centroid and Franck-Condon factors approximation's for fluorescence transitions of A) the $A^1\Pi(v'=3, J'=1) - X^1\Sigma^+(v''=n)$ band and B) the $A^1\Pi(v'=4, J'=1) - X^1\Sigma^+(v''=n)$ band.

In Table 4.4 average normalized areas of measured peaks are compared to the normalized FCFs and the normalized transition probability calculated using the r-

centroid approximation. It is clear from these results that the r-centroid approximation can approximate the transition probability more effectively than the FCFs.

Table 4.4: Comparing the average normalized areas of measured peaks to normalized FCF approximation and normalized r-centroid approximation.

$v'' = n$	Normalized peak area	Normalized FCFs	Percentage difference	Normalized r-centroid	Percentage difference
1	0.28	0.18	36.37	0.15	44.58
2	1.00	1.00	0.00	1.00	0.00
3	0.80	0.77	4.51	0.67	15.88
4	0.48	0.72	48.37	0.52	7.48
5	0.32	0.58	80.50	0.23	26.75
6	0.41	1.36	233.05	0.39	4.97
7	0.24	1.27	419.01	0.25	3.86
8	0.10	0.72	618.80	0.11	7.50
9	0.05	0.29	525.55	0.04	17.83
10	0.02	0.09	440.72	0.01	19.93

4.4.2 Vibrational constants

Vibrational constants of $^{12}\text{C}^{16}\text{O}$ can be determined by investigating the peak positions of the fluorescence peaks in Figure 4.15.A. The $A^1\Pi(v'=3) - X^1\Sigma^+(v''=0)$ transition was used as the zero-point energy. This point was also used as the reference point for the remaining spectral peaks. The conversion from wavelength (nm) to wave numbers (cm^{-1}) is given by:

$$\text{Energy}\left(\text{cm}^{-1}\right) = \frac{\lambda_{A^1\Pi(v'=3)-X^1\Sigma^+(v''=0)} - \lambda_{A^1\Pi(v'=3)-X^1\Sigma^+(v''=n)}}{\left(\lambda_{A^1\Pi(v'=3)-X^1\Sigma^+(v''=0)}\right)\left(\lambda_{A^1\Pi(v'=3)-X^1\Sigma^+(v''=n)}\right)} \times 10^7. \quad (4.4.4)$$
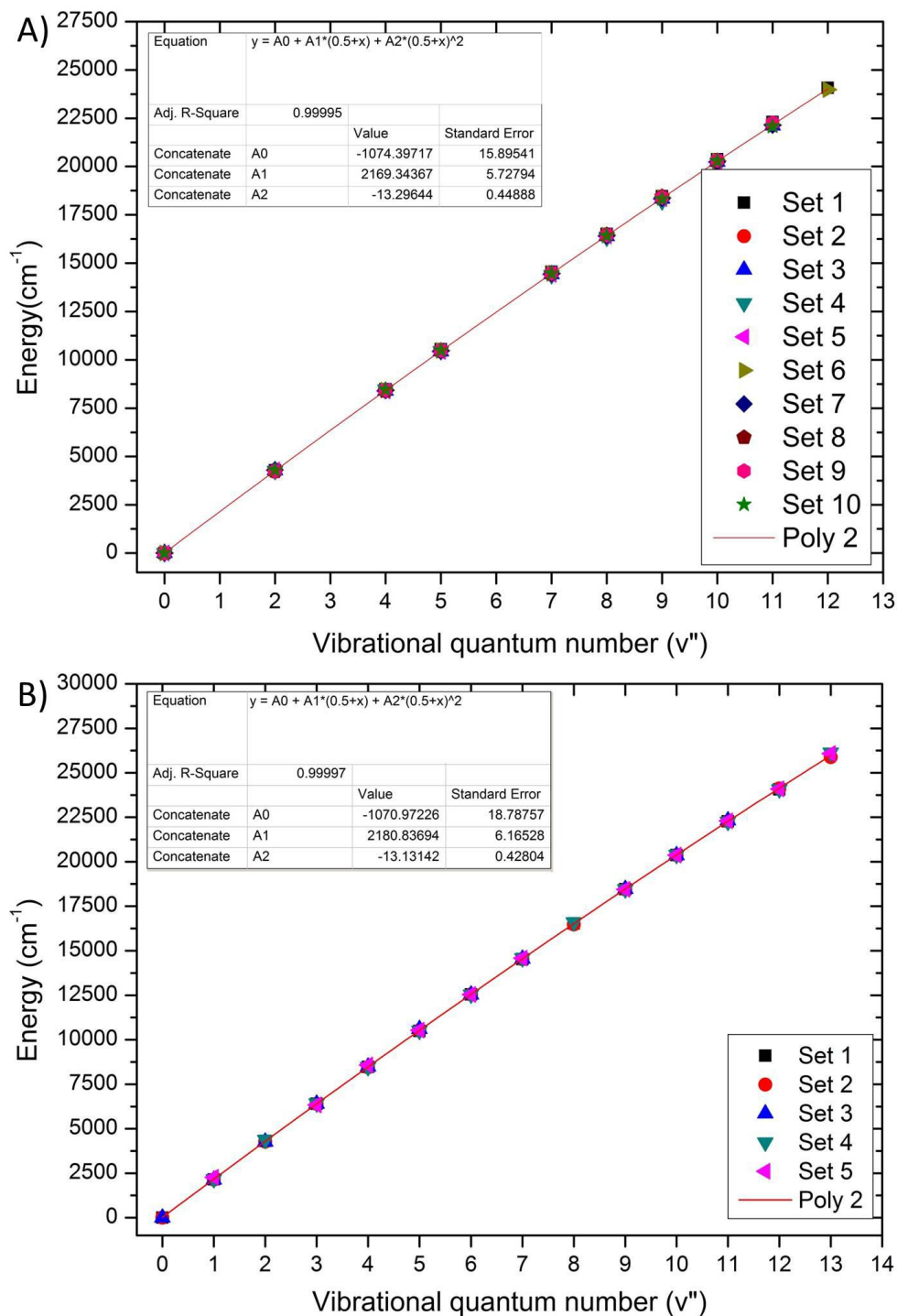
Figure 4.21: Measured vibrational energy vs. vibrational quantum number for A) $A^1\Pi(v' = 3) - X^1\Sigma^+(v'' = n)$ and B) $A^1\Pi(v' = 4) - X^1\Sigma^+(v'' = n)$ transitions.

By fitting Equation (2.2.13) to Figures 4.21.A & 4.21.B it was possible to extract the vibrational constants for the $X^1\Sigma^+$ potential. However, it was found that for

a low error fit it was necessary to exclude the $A^1\Pi(v'=3) - X^1\Sigma^+(v''=1)$ as it was not possible to determine the position of this peak accurately. From the fits in Figures 4.21.A & 4.21.B it can be observed that the coefficient A0 is the negative of the turning point energy $(\Gamma_{0,0})$ as a result of using $A^1\Pi(v'=3) - X^1\Sigma^+(v''=0)$ transition as the zero-point energy. In Figures 4.21.A & 4.21.B the harmonic constant ω_e is given by A1 and the anharmonic constant $\omega_e\chi_e$ is given by A2. These measured values were also compared to that of the literature (Table 4.5) where it can be observed that the measured values are within 1.4% of the literature values.

Table 4.5: Comparison between measured and literature values for vibrational constants of the $X^1\Sigma^+$ potential.

Vibrational constants	Measured value	Literature [10]	Percentage difference	Literature [2]	Percentage difference
Measured from $A^1\Pi(v'=3) - X^1\Sigma^+(v''=n)$					
$\Gamma_{0,0}(\text{cm}^{-1})$	1074.40	1085.447	1.018	1085.431	1.017
$\omega_e(\text{cm}^{-1})$	2169.34	2169.814	0.022	2169.813	0.022
$\omega_e\chi_e(\text{cm}^{-1})$	13.30	13.28831	0.058	13.28791	0.061
Measured from $A^1\Pi(v'=4) - X^1\Sigma^+(v''=n)$					
$\Gamma_{0,0}(\text{cm}^{-1})$	1070.97	1085.447	1.334	1085.431	1.332
$\omega_e(\text{cm}^{-1})$	2180.84	2169.814	0.508	2169.813	0.508
$\omega_e\chi_e(\text{cm}^{-1})$	13.13	13.28831	1.184	13.28791	1.181

4.4.3 Isotopomers

As mentioned in the previous sections, CO has different isotopomers. It was possible to measure the fluorescence spectra of 3 out of the 4 isotopomers namely $^{12}\text{C}^{16}\text{O}$ (natural abundance of 98.668%), $^{13}\text{C}^{16}\text{O}$ (natural abundance of 1.100%) and $^{12}\text{C}^{18}\text{O}$ (natural abundance of 0.1979%) with natural CO gas as a sample. As a result of the low abundance of $^{12}\text{C}^{17}\text{O}$ (natural abundance of 0.04%) which in turn results in the intensity of the fluorescence to be low, it was not possible to measure this fluorescence. In Figure 4.22 the fluorescence measurements can be observed for the different isotopomers. The different isotopomers were selectively excited by using appropriate excitation wavelengths so that it is sure that each fluorescence spectrum contains only fluorescence from the chosen isotopomer.
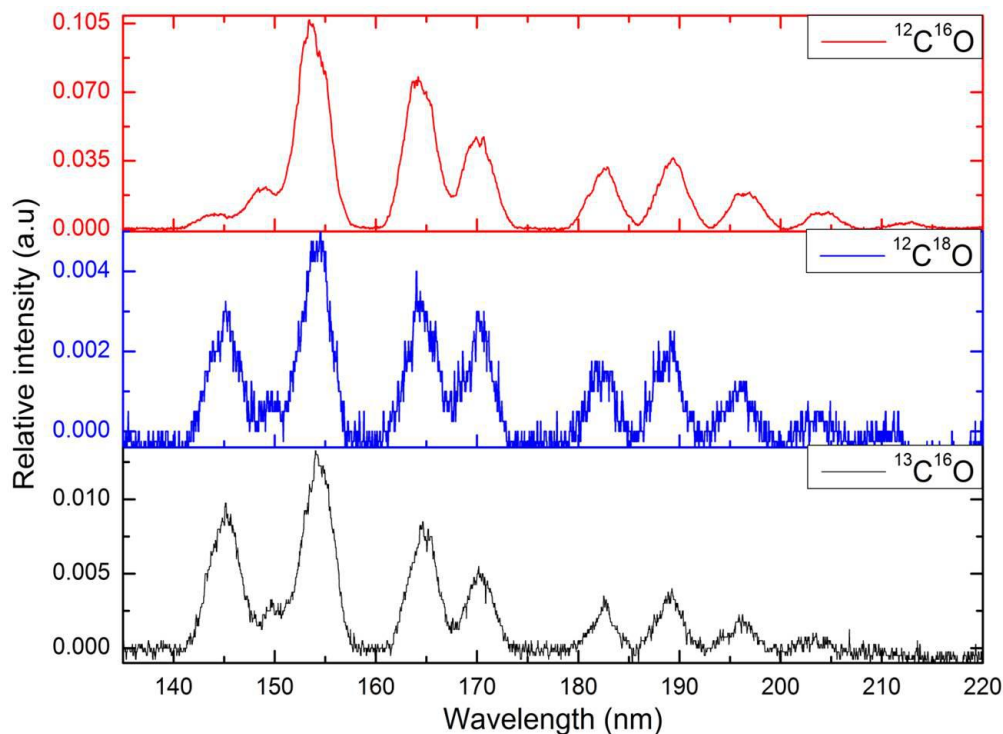
Figure 4.22: Fluorescence spectra of different CO isotopomers for $A^1\Pi(v' = 3, J' = 1) - X^1\Sigma^+(v'' = n)$ transitions.

The same data analysis which was done on $^{12}C^{16}O$ has been done on these isotopomers as well. Firstly, new Franck-Condon factors and r-centroid values were calculated. Literature values from [2] were used for comparison as it contains values for all isotopes measured in the current study, thus making it unnecessary to use Equation (2.2.17) for scaling vibrational constants. It can firstly be observed from Table 4.6 that the measured vibrational constants agree with that of the literature within 2%. Secondly, the gradient coefficients ($A1$) for R_e are similar for the isotopomers $^{12}C^{18}O$ and $^{13}C^{16}O$.

It can be observed in Table 4.7 that the r-centroid approximation approximates the transition probability more accurately compared to that of the FCF's, for both the $^{12}C^{18}O$ and $^{13}C^{16}O$ isotopomers.

In Figure 4.22 it can be observed that the isotopomers $^{12}C^{18}O$ and $^{13}C^{16}O$ undergo significantly less self-absorption compared to $^{12}C^{16}O$ isotope for the $A^1\Pi(v' = 3) - X^1\Sigma^+(v'' = 0)$ band, this is as a result of a low natural abundance of these isotopomers thus leading to a lower population in the $v = 0$ vibrational level.

Table 4.6: Summary of results for different isotopomers of carbon monoxide, results can be observed in Figure A.1

		$^{12}\text{C}^{16}\text{O}$	$^{12}\text{C}^{18}\text{O}$	$^{13}\text{C}^{16}\text{O}$
Natural abundance	Literature [23]	98.668	0.1979	1.100
$\Gamma_{0,0}(\text{cm}^{-1})$	Literature [2]	1081.586	1055.536	1057.545
	Measured	1074.40	1081.456	1067.301
	Percentage difference	0.67	2.46	0.92
$\omega_e(\text{cm}^{-1})$	Literature [2]	2169.813	2117.397	2121.439
	Measured	2169.34	2116.317	2120.423
	Percentage difference	0.022	0.051	0.048
$\omega_e\chi_e(\text{cm}^{-1})$	Literature [2]	13.288	12.654	12.702
	Measured	13.30	12.490	12.656
	Percentage difference	0.14	1.30	0.36
R_e coefficients (Å^{-2}) (from measurements in this study)	A0	-614.994	2.475	4.53788
	A1	-2.3282	0.657	0.6887
	A2	1.7853	N/A	N/A
	A3	0.4525	N/A	N/A

Table 4.7: Comparing the average normalized areas of measured peaks to normalized FCF approximation and normalized r-centroid approximation for the $A^1\Pi(v'=3) - X^1\Sigma^+(v''=n)$ band of $^{12}\text{C}^{18}\text{O}$ and $^{13}\text{C}^{16}\text{O}$.

$v''=n$	Normalized peak area	Normalized FCFs	Percentage difference	Normalized r-centroid	Percentage difference
Measured from $A^1\Pi(v'=3) - X^1\Sigma^+(v''=n)$ for $^{12}\text{C}^{18}\text{O}$					
1	0.16	0.05	70.20	0.05	67.34
2	1.00	1.00	0.00	1.00	0.00
4	0.76	0.55	28.04	0.38	50.26
5	0.55	0.87	58.96	0.49	10.24
7	0.39	0.30	21.62	0.10	73.92
8	0.48	1.16	144.30	0.28	40.34
9	0.32	1.37	324.67	0.23	28.60
10	0.19	0.94	384.06	0.10	48.61
Measured from $A^1\Pi(v'=3) - X^1\Sigma^+(v''=n)$ for $^{13}\text{C}^{16}\text{O}$					
1	0.18	0.05	69.79	0.06	65.77
2	1.00	1.00	0.00	1.00	0.00
4	0.62	0.54	11.47	0.34	45.06
5	0.37	0.87	134.19	0.41	10.39
7	0.19	0.28	47.25	0.06	67.66
8	0.25	1.13	344.65	0.15	40.71
9	0.15	1.36	796.49	0.09	39.33
10	0.07	0.95	1287.35	0.02	66.59

4.5   Self-absorption

To explain self-absorption, consider a molecule in the vibrational ground state ($X^1\Sigma^+$ ($v'' = 0$)) which is then excited to an excited electronic state ($A^1\Pi(v' = 3)$). When this molecule de-excites it emits a photon. This photon can be emitted in any direction and to any vibrational level in the ground state potential ($X^1\Sigma^+(v'' = n)$), since there is no selection rule for vibronic transitions between electronic states. In our optical setup, only 0.26% of all the fluorescence emitted into all directions reaches the detector. Therefore, an emitted photon has a 0.26% chance of being emitted in the correct direction to be detected.

Under the low temperature conditions in the gas jet the $v'' = 0$ level is the only vibrational level in the ground state that has a significant population. If a molecule de-excites from $A^1\Pi(v' = 3)$ level to $X^1\Sigma^+(v'' = 0)$ the photon which is emitted will be resonant with an excitation transition of the populated $v'' = 0$ state. This photon can interact with a molecule in the vibrational ground state as not all the sample gas (molecules) would have been excited into a higher electronic state. Once again this newly excited molecule de-excites into any vibrational level in the ground state potential ($X^1\Sigma^+(v'' = n)$) and emit a photon into any direction with again only a 0.26% chance of reaching the detector. This process significantly reduces the probability of detecting fluorescence in the $A^1\Pi(v' = 3) - X^1\Sigma^+(v'' = 0)$ band. However, if the molecule would de-excite to any vibrational level in the ground state potential excluding the ground vibrational level ($X^1\Sigma^+(v'' = n)$ with $n \neq 0$), the emitted photon will not be reabsorbed by a molecule as all the sample gas molecules are in the vibrational ground state ($X^1\Sigma^+(v'' = 0)$).
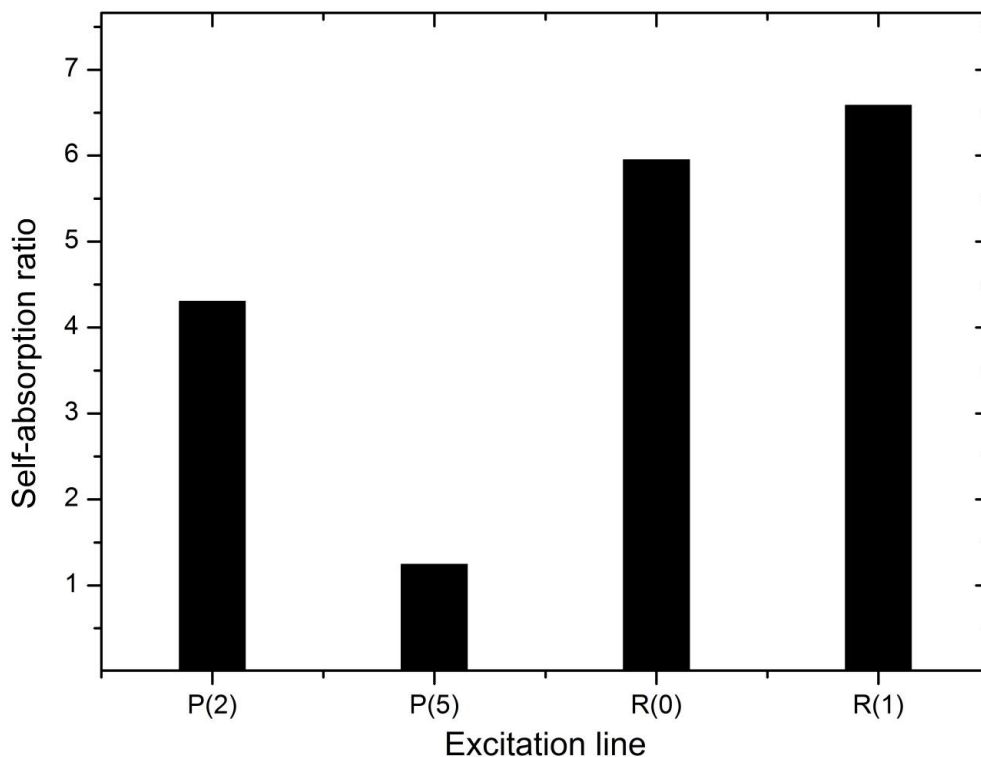
Figure 4.23: Ratio of the $A^1\Pi(v'=3) - X^1\Sigma^+(v''=2)$ band area and $A^1\Pi(v'=3) - X^1\Sigma^+(v''=0)$ band area as measure of self-absorption.

To quantify the self-absorption in fluorescence spectra, the ratio of peak areas of the $A^1\Pi(v'=3) - X^1\Sigma^+(v''=2)$ peak (that is not self-absorbed) to the $A^1\Pi(v'=3) - X^1\Sigma^+(v''=0)$ peak (that is self-absorbed) can be used. The larger the ratio, the more self-absorption has taken place. This method is applied to the fluorescence spectra in Figure 4.15.A. The result is shown in Figure 4.23. The different fluorescence spectra of Figure 4.15.A are resulting from excitation of different rovibronic transitions in the same vibronic band. Figure 4.23 shows a significant difference in the degree of self-absorption in these spectra. This observation can be explained by considering the selection rules for rovibronic transitions and the relative populations of the different rotational levels in the $X^1\Sigma^+(v''=0)$ state.

A detailed analysis of this aspect will be presented in Section 4.6. However, we can already make the important conclusion that the degree of self-absorption is different for fluorescence resulting from different rovibronic excitations and therefore self-absorption must have a significant effect on the relative peak heights in rotationally resolved excitation spectra.

4.6 Rotationally resolved excitation spectra of Carbon Monoxide

In this section, the rotationally resolved excitation spectra done on CO will be discussed. For rotationally resolved measurement the CO molecule will be excited from of a specific rovibronic state $(X^1\Sigma^+(v''=0, J''=n))$ in the ground state to a specific rovibronic state in a different potential $(A^1\Pi(v'=3, J'=n, n\pm1)$ where allowed) and the total fluorescence from all the allowed de-excitation transitions to rovibronic levels in the ground electronic state $(A^1\Pi(v'=3, J'=m) - X^1\Sigma^+(v''=0, J''=m, m\pm1)$ where allowed) is recorded using a PMT. The PMT can not distinguish between different wavelength, thus all the de-excitation pathways are recorded as one. For rotational excitation measurements the tuneable dye laser is tuned over a wavelength region and the signal from the PMT is recorded as a measure of a number of molecules excited vs. wavelength.

In Figure 4.24 a rotational excitation spectrum for $X^1\Sigma^+(v''=0, J''=n) - A^1\Pi(v'=3, J'=n, n\pm1)$ band of $^{12}C^{16}O$ can be observed. Also, indicated in Figure 4.24 is the corresponding rotational branches. For the R, Q and P transitions $J'=J''-1$, $J'=J''$ and $J'=J''+1$ respectively. The value of J'' is indicated in the brackets for each transition.
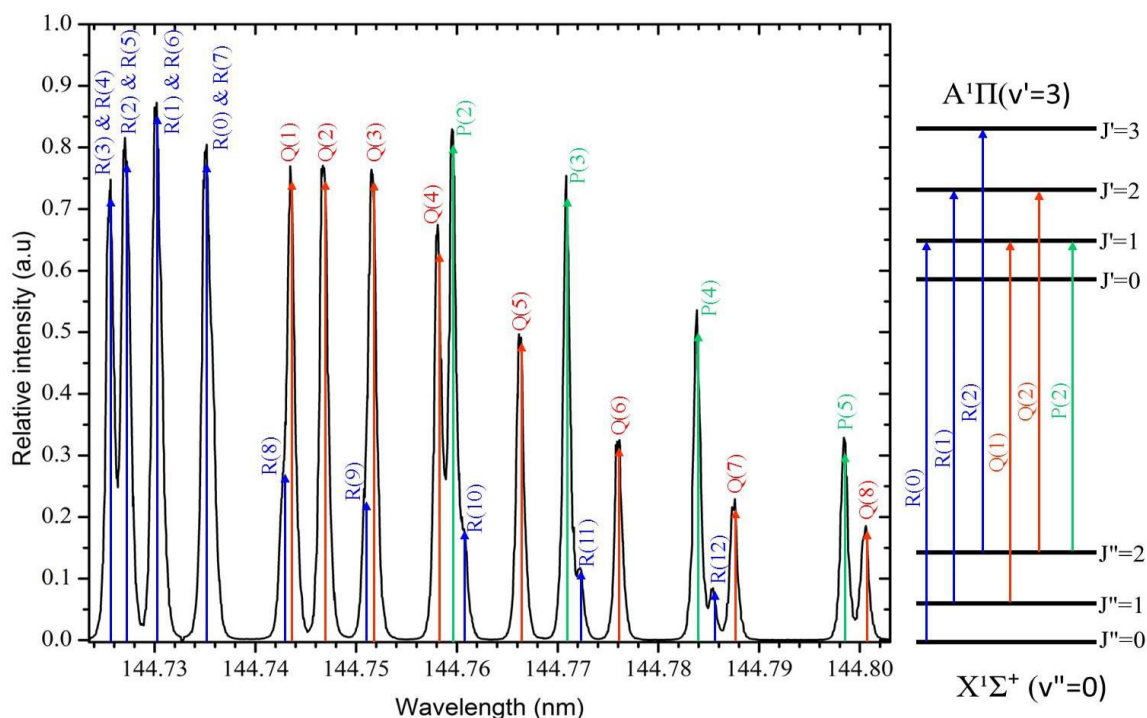
Figure 4.24: Rotational excitation spectrum for $X^1\Sigma^+(v''=0, J''=n) - A^1\Pi(v'=3, J'=n, n\pm1)$ band of CO, with associated branches indicated.

As described in Section 2.2.1.1 the $Q(0)$, $P(1)$ and $P(2)$ transition do not occur as they are forbidden by the fact that the $J''=0$ rotational level does not exist.

Additionally, it can be observed that the R-branch folds back on its self, this is as a result of the spacing between the rotational levels for the $X^1\Sigma^+$ and $A^1\Pi$ electronic transitions of $^{12}C^{16}O$. It is important to note that the $Q(2)$, $Q(5)$ and $Q(6)$ transitions are transitions which do not have any other transition occurring nearby, thus making these transitions ideal for spectral resolution comparison between different spectra.

4.6.1 Rotational excitation spectra analysis

When measuring rotational excitation spectra the wavelength recorded is that of the tuneable dye laser and not that of the generated VUV light. Using the calibration data in Section 4.1.1 it is possible to convert the visible wavelengths to the VUV regime (accurate to 0.0015 nm). This makes it possible to identify the vibronic band and the CO isotope which was excited. It was determined that using the visible calibration that the isotope measured in Figure 4.25 is the $^{12}C^{16}O$ isotope, additionally, it was determined that the $X^1\Sigma^+(v''=0, J''=n) - A^1\Pi(v'=4, J'=n, n \pm 1)$ band was excited.
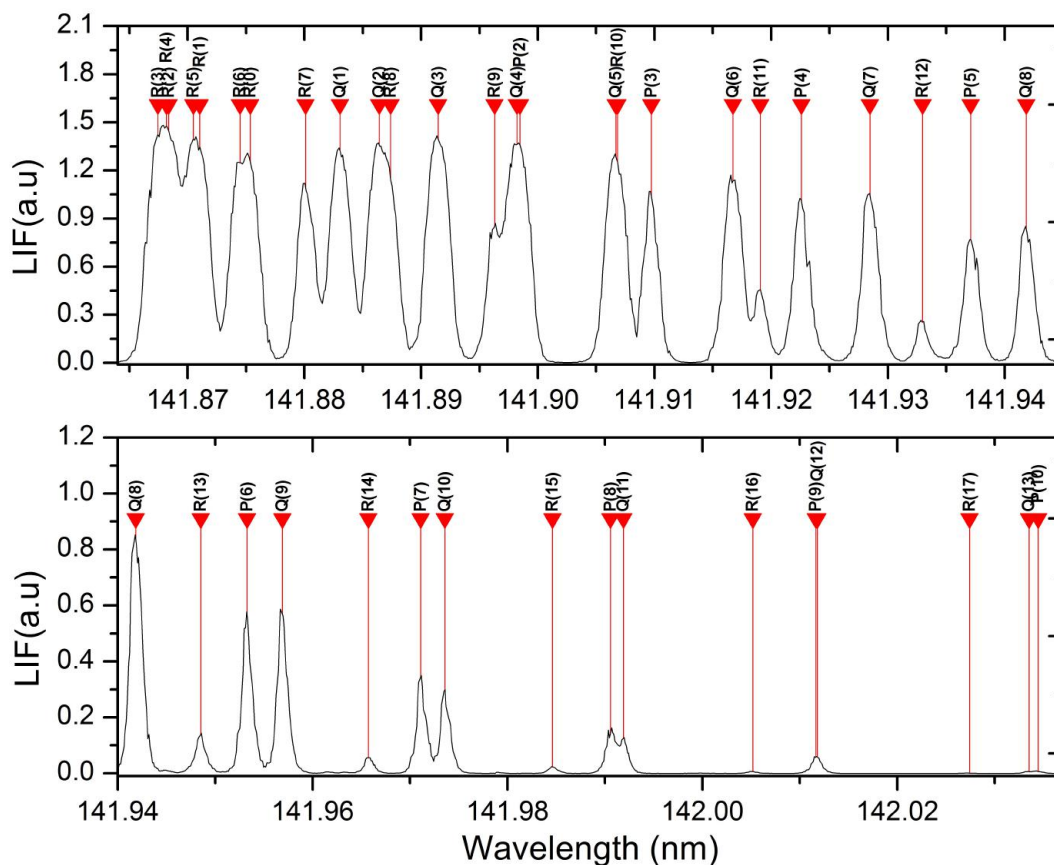
Figure 4.25: Rotational excitation spectra for $X^1\Sigma^+(v''=0) - A^1\Pi(v'=4)$ band of $^{12}C^{16}O$ calibrated using the calibrated visible dye laser wavelengths. The triangles indicate literature wavelengths of the lines.

The VUV wavelengths can be determined more accurately by using the available literature values of the $^{12}C^{16}O$ rovibronic transitions to calibrate the spectra in Figure 4.25. Literature values from Niu et al. [11] were used in this study. The study done by Niu et al. measured the $X^1\Sigma^+(v''=0, J''=n) - A^1\Pi(v'=4, J'=n, n\pm 1)$ band of CO up to the $J''=50$ with an accuracy of $0.01\text{-}0.02\,\text{cm}^{-1}$. Calibration was successfully achieved using these values (Figure 4.26.A).
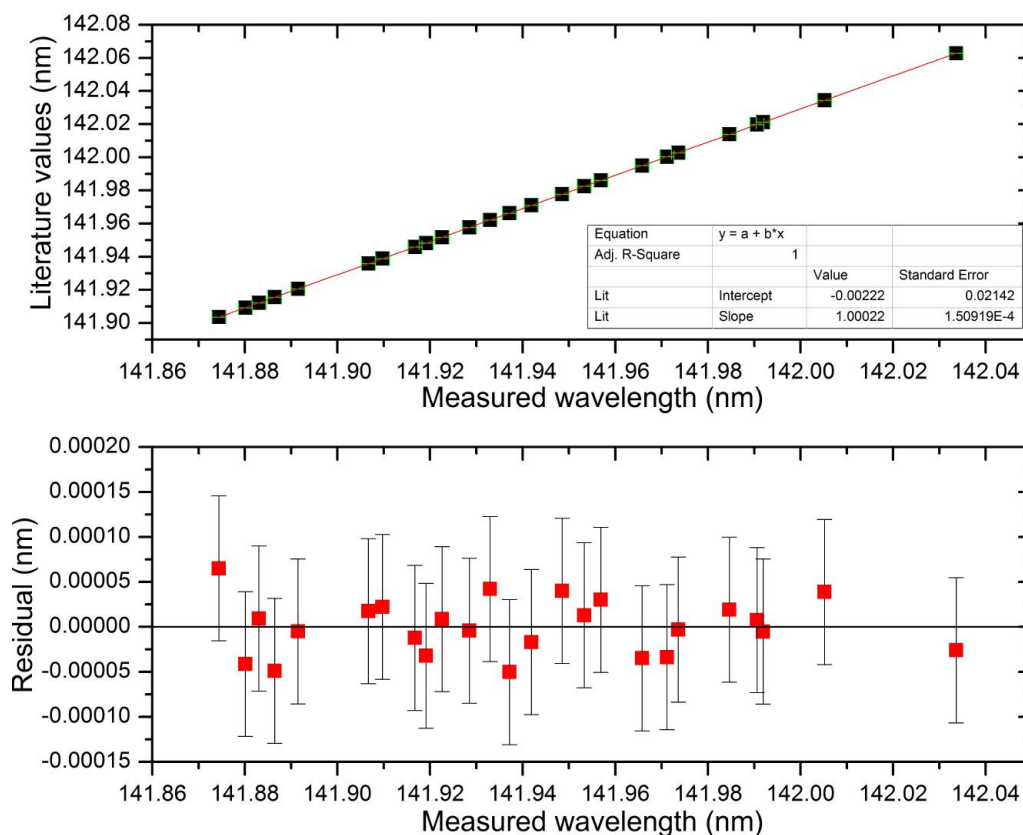
Figure 4.26: Calibration to literature values for the $X^1\Sigma^+(v''=0) - A^1\Pi(v'=4)$ band of $^{12}C^{16}O$ A) linear fit using literature from Niu et al. and B) residual data from linear fit (literature λ - λ calibrated from linear fit).

The residual fit data from Figure 4.26.A is shown in Figure 4.26.B. The $\sim$1 slope of the linear fit shows that the initial calibration using the hollow cathode lamp is in agreement with literature values. The intercept given by the linear fit indicates that calibration using the hollow cathode lamp needs to be shifted by $0.084\,\text{nm}$. This shift is significant in this wavelength region.

Niu et al. states an uncertainty of $0.02\,\text{cm}^{-1}$ of their measured wavelengths, except for "weak or blended" lines. This corresponds to an uncertainty of $\sim$0.04 pm in the wavelength range of our measurements. The standard deviation of the residual data (Figure 4.26.A) of our calibration is $\sim$0.08 pm. Thus, the estimated deviation of the mean is $\frac{standard\,deviation}{\sqrt{number\,of\,datapoints}} = \frac{0.08}{\sqrt{25}} = 0.016\,\text{pm}$. The wavelength uncertainty

for this study was calculated using error propagation which by $\sqrt{(0.04)^2 + (0.016)^2}$ = 0.043 pm. Therefore we take the uncertainty in our measured wavelengths to be 0.043 pm.
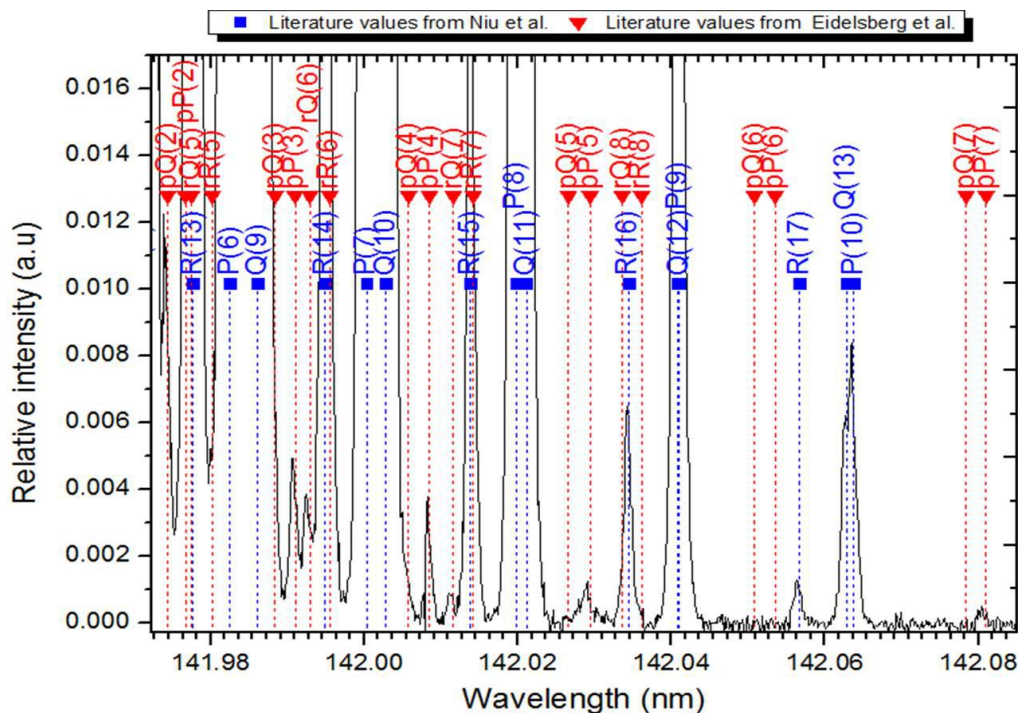
Figure 4.27: Rotational excitation spectrum for $X^1\Sigma^+(v'' = 0) - A^1\Pi(v' = 4)$ band of $^{12}C^{16}O$ with corresponding literature for singlet-singlet and triplet-singlet transitions.

When investigating the spectrum in Figure 4.27 close to the signal noise limit it was discovered that multiple singlet-triplet transitions were recorded. The triplet state which perturbs the singlet state $A^1\Pi(v' = 4)$ is known to be the $a^{'3}\Sigma^+(v' = 14)$ state. The study done by Niu et al. did not record any of these transitions, however, a study done by Eidelsberg et al. [12] has calculated wavelengths for this transition and presented measured wavelengths from Herzberg et al. [38]. The values from Eidelsberg et al. was compared (Table 4.9) to the values measured in this study. From the comparison in Table 4.9, it can be observed that the calculated values given by Eidelsberg et al. (λ_{calc}) are larger than our wavelengths by an average of 0.37 pm. The measured wavelengths from Eidelsberg et al. (λ_{meas}) are larger by 0.33 pm on average. This difference is 4 times larger than the uncertainty in our calibration ($\sim$0.08 pm) and therefore significant. There seems to be a systematic shift of 0.3-0.4 pm between the wavelengths of Niu et al. [11] and Eidelsberg et al. [12]. Niu et al. and Eidelsberg et al. wavelengths can be compared directly for a number of high-J transitions to the $a^{'3}\Sigma^+(v' = 13)$, $e^3\Sigma^-(v' = 4)$ and $d^3\Delta(v' = 8)$ excited states (Table 4.8).

Table 4.8: Wavelength comparison between Niu et al. [11] and Eidelsberg et al. [12] for high-J transitions.

		Values from Niu et al. (cm^{-1})	Values from Eidelsberg et al. (cm^{-1})	Diff. (cm^{-1})	Diff. (pm)
$a'^3\Sigma^+(v'=13)$	$^PP(31)$	68624.61	68607.29	17.32	-36.8
	$^PP(32)$	68568.47	68568.55	-0.08	0.2
	$^RR(29)$	68857.8	68840.46	17.34	-36.6
	$^RR(30)$	68809.19	68809.26	-0.07	0.1
	$^RQ(33)$	68664.38	68651.2	13.18	-28
	$^RQ(34)$	68610.5	68610.07	0.43	-0.9
$e^3\Sigma^-(v'=4)$	$^OP(26)$	67346.78	67346.7	0.08	-0.2
	$^OP(27)$	67298.26	67317.4	-19.14	42.2
	$^QR(23)$	67574.05	67574.12	-0.07	0.2
	$^QR(24)$	67542.09	67541.99	0.10	-0.2
	$^QR(25)$	67501.14	67520.28	-19.14	42
	$^QQ(27)$	67429.16	67428.96	0.20	-0.4
	$^QQ(28)$	67391.5	67391.31	0.19	-0.4
	$^QQ(29)$	67341.85	67361.23	-19.38	42.7
	$^QQ(30)$	67300.6	67337.38	-36.78	81.2
	$^QQ(32)$	67210.86	67290.28	-79.42	175.6
	$^QP(32)$	67212.33	67212.04	0.29	-0.6
	$^QP(33)$	67158.32	67168.73	-10.41	23.1
	$^SR(31)$	67406.56	67416.98	-10.42	22.9
	$^SR(32)$	67369.2	67392.72	-23.52	51.8
$d^3\Delta(v'=8)$	$^SR(25)$	68912.94	68912.78	0.16	-0.3
	$^RQ(26)$	68813.41	68815.51	-2.10	4.4
			Average Diff.	-7.78	17.36

The average difference for all these lines are $17\,pm$ ($8\,cm^{-1}$). We conclude that (1) Niu et al. wavelengths for the forbidden lines have much larger uncertainties than $0.02\,cm^{-1}$ and (2) our wavelengths indicated a constant $\sim0.35\,pm$ wavelength shift between Niu et al. and Eidelsberg et al. data.

Table 4.9: Measured singlet-triplet transitions of $^{12}C^{16}O$ for the $X^1\Sigma^+(v''=0) - a'^3\Sigma^+(v'=14)$ band. Comparison of wavelengths measured in this study (λ') to calculated (λ_{calc}) and measured (λ_{meas}) wavelengths from Eidelsberg et al. [12]. All values are in nm.

Lable	λ'	λ_{calc}	$\lambda_{calc} - \lambda'$	λ_{meas}	$\lambda_{meas} - \lambda'$
$^PP(3)$	141.9907	141.9910	0.32 pm	141.9910	0.32 pm
$^RQ(6)$	141.9925	141.9929	0.44 pm	141.9928	0.34 pm
$^PP(4)$	142.0082	142.0085	0.27 pm	142.0085	0.27 pm
$^PP(5)$	142.0290	142.0294	0.44 pm	142.0294	0.44 pm
$^PQ(2)$	141.9740	141.9744	0.38 pm	141.9744*	0.38 pm
$^RQ(7)$	142.0112	142.0116	0.40 pm	142.0115*	0.30 pm
$^PP(7)$	142.0806	142.0810	0.44 pm	142.0810*	0.44 pm
		Avg	0.38 pm	Avg	0.36 pm

It is of interest to note that the triplet-singlet transition in Table 4.9 was measured without any optimization for triplet-singlet transition as described in Section 3.2.3. If optimization would have been done for triplet-singlet transition it is highly likely that more lines would be measured and, the triplet-singlet transition which occur close to singlet-singlet transition would be resolved.

4.6.2   New technique for measuring VUV intensity during measurements

Whilst measuring rotational excitation spectra the transmitted VUV light is also recorded using PMT 3 in Figure 3.3. The light measured by PMT 3 does not give a true indication of the amount of VUV light generated (in the magnesium vapour during nonlinear conversion) during measurement as the light passes through the CO gas. Even if the VUV light generated in the magnesium vapour does not correspond to an excitation wavelength of CO it can still be affected by the supersonic gas jet. To measure the amount of VUV light generated in the magnesium vapour without interference from the supersonic gas jet it was decided to change the frequency of the pulsed valve from 10 Hz to 5 Hz (Section 3.2.3). This would allow for every second laser pulse to interact with the supersonic gas jet and every other laser pulse would not, thus allowing for an accurate measurement of the amount of VUV light generated during measurements.

In Figure 4.28.A a rotational excitation spectrum can be observed where the pulsed valve frequency is set to 10 Hz whilst, in Figure 4.28.B the pulsed valve frequency is set to 5 Hz. It can firstly be noted that there is a significant increase in the spectral resolution in the 5 Hz spectrum. As mentioned in the preface section

---

*These values are not reported by Eidelsberg et al. [12] in the paper published in 2003, but are reported at `https://molat.obspm.fr/index.php?page=pages/Molecules/CO-Michele/CO.php`. However, the source of the observed values are not given and the wavelength for the $^PP(7)$ line is indicated as obtained by extrapolation. That means that these wavelengths can not be traced back to a peer-reviewed publication.

Figure 4.28: Rotational excitation spectra for $X^1\Sigma^+(v''=0, J''=n) - A^1\Pi(v'=3, J'=n, n\pm1)$ band of CO, with different frequency of the pulsating gas value set to A) 10 Hz and B) 5 Hz.

the only peak that can be used to quantify the spectral resolution increase is $Q(2)$ as it is not mixed with any other transitions. It was determined that the FWHM of the $Q(2)$ line decreased from 0.93 pm to 0.72 pm (a decrease of 21.74%).

It could be argued that the spectrum with the pulsed valve frequency at 10 Hz has the higher spectral resolution when considering the peak separation between the first 2 peaks ($R(3)R(4)$ and $R(2)R(5)$ transition), however, it is important to note that the spectrum measured using the pulsed valve frequency at 10 Hz was measured at a lower temperature than the spectrum using the pulsating gas value frequency at 5 Hz and secondly the first 2 peaks in the spectra are mixed peaks where the first peak is a combination of $R(3)$ and $R(4)$ transitions while the second peak is a combination of $R(2)$ and $R(6)$ transitions.

The cause of the increase in the resolution is not precisely clear however, it was observed that working with the pulsating gas value frequency at 10 Hz causes an increase in the vacuum pressure of the system from 3.5×10^{-6} mbar to 9.0×10^{-6} mbar. When working with the pulsed valve frequency at 5 Hz no change in vacuum pressure was observed.
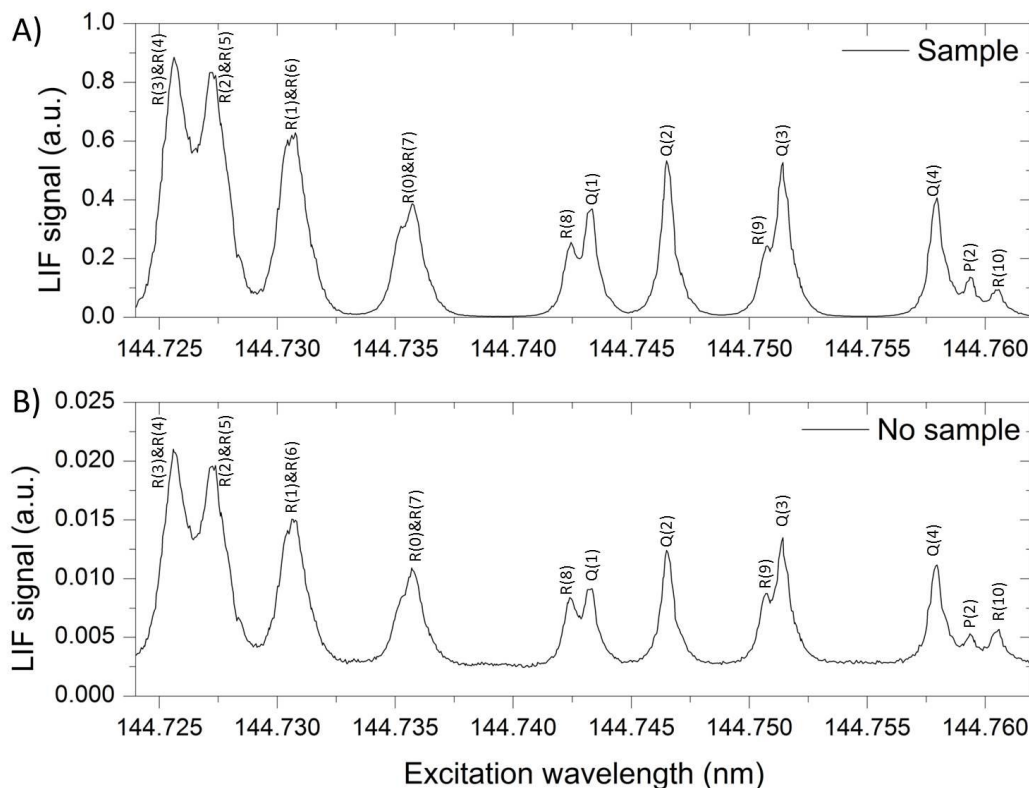
Figure 4.29: Rotational excitation spectra for $X^1\Sigma^+(v''=0, J''=n) - A^1\Pi(v' = 3, J' = n, n \pm 1)$ band of CO, with having the laser and valve pulse A) synchronised and B) not synchronised. Both spectra were taken with the pulsating valve operating at $5\,\text{Hz}$.

The data of the pulsed valve with a frequency of $5\,\text{Hz}$ was plotted in Figures 4.29.A & 4.29.B, where it can be observed that when the gas and laser pulse are not synchronized (laser pulse does not interact with supersonic gas jet) a rotational excitation spectrum was still recorded. It is important to note that the measured intensity of the "no sample" spectrum (of the background gas) is 40 times smaller, compared to when the supersonic gas jet and laser pulse are synchronized. This indicates that there is residual gas in the vacuum system between pulses. Thus, having the pulsed valve frequency at $10\,\text{Hz}$ would result in more residual CO gas in the vacuum system. This residual gas could lead to a reduced spectral resolution, as this gas could interfere with the supersonic gas jet and cause collisional broadening. Thus, all measurements will be done using the pulsed valve at a frequency of $5\,\text{Hz}$, thus reducing the amount of residual gas in the vacuum system between pulses.

At the start of this section the aim of using the pulsed valve at a frequency of $5\,\text{Hz}$ was to measure two spectra simultaneously, where the first would be with the sample gas (supersonic gas jet and laser pulse are synchronized) and second would be without the sample gas (supersonic gas jet and laser pulse are not synchronized), which would lead to a better indication of the true amount of VUV light generated during measurements. This result can be observed in graphs of the transmitted VUV

vs. wavelength in Figure 4.30.A where "sample" indicates when the supersonic gas jet and laser pulse are synchronized and "no sample" indicates when the supersonic gas jet and laser pulse are not synchronized.
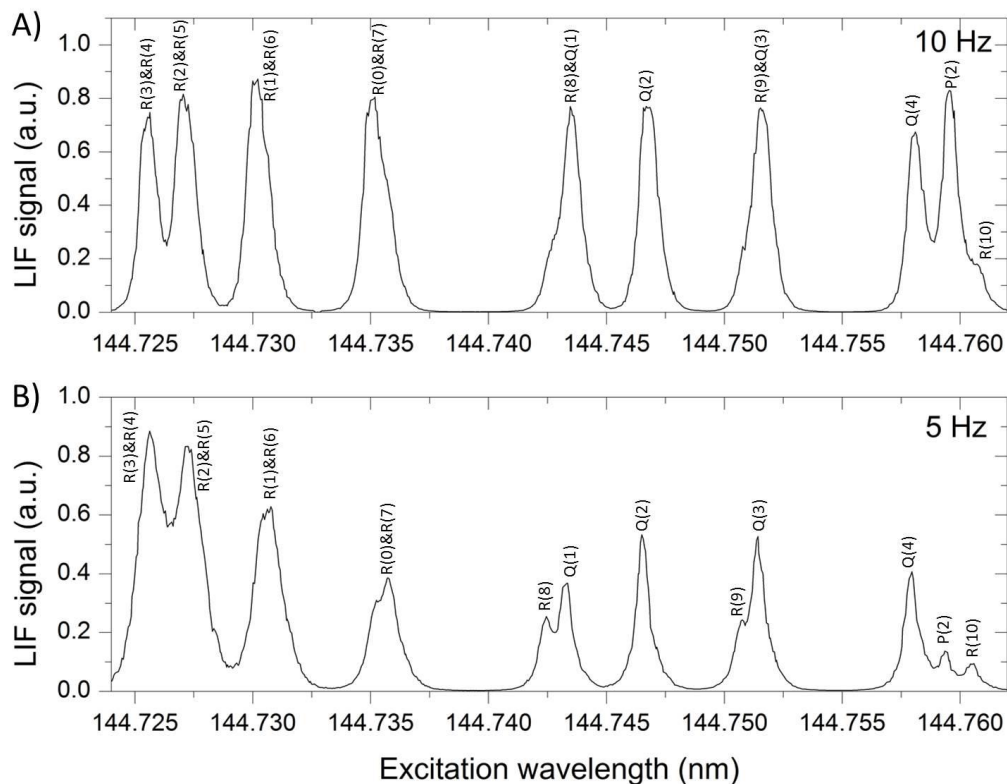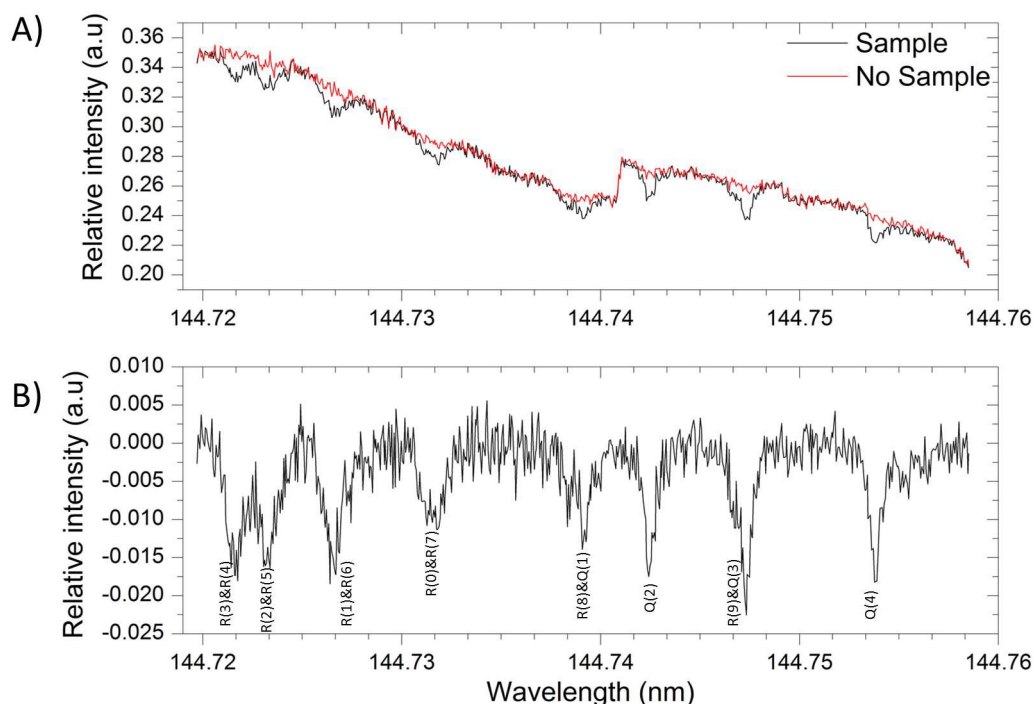

Figure 4.30: Rotational absorption spectra for $X^1\Sigma^+(v'' = 0, J'' = n) - A^1\Pi(v' = 3, J' = n, n \pm 1)$ band of CO, where A) is the transmitted VUV with and without sample and B) is the differences between the spectra in A) corresponding to a rotationally resolved absorption spectrum.

It can firstly be observed that there is a gradual decrease in the amount of VUV light generated during the measurement. This is not uncommon as the dye of the dye laser gets depleted over time resulting in lower intensity. Secondly, it can be observed that there is a significant fluctuation in the VUV intensity around the 144.742 nm region. This could be as a result of a fluctuation in the input energy or a crystal forming and dissolving inside the heat-pipe.

Since these measurements are taken using a pulse to pulse method and the signal pathway is exactly the same for the two measurements the artefacts are present in both spectra. What is meant with signal pathway is that all of the parameters for a single laser pulse are the same except the laser intensity, thus eliminating any longer-term changes which would be observed for measurements not done in this method (for example the position and size of the gate used with the boxcar integrates and PMT voltage could differ, crystals in heat pipe).

This measurement was done using a 60 pulse averaging, thus at each point in the data of 60 pulses were recorded before the wavelength is altered. For a single data point in the spectrum, the data measured would alternate between sample and

no sample for 60 pulses. It is firstly necessary to split the data into two sets where the first data set would only contain data of pulses with the sample gas and second data set would contain only data of pulses without the sample gas. Once the data is split into these two sets, the average is taken over the data collected for a specific wavelength position. Having the recorded data points alter between "sample" and "no sample" allows for more accurate measurement of the intensity of the VUV light compared to measurements done by only firstly recording data with gas sample and then recording data without sample, as it is possible that intensity of the VUV light could change significantly between these measurements.

Since the spectrum in Figure 4.30.A was recorded firstly under the same conditions and the secondly follows the same signal pathway it is possible to use the spectrum recorded containing "no sample" as a baseline for the "sample" spectrum. By subtracting these two sets of data it is possible to eliminate all artefacts caused by the signal processing as well as being able to correct for the decrease in laser intensity as can be observed in Figure 4.30.B. This method of measuring rotational absorption spectra is not ideal as the intensity does fluctuate from pulse to pulse, leading to the noisy signal observed in Figure 4.30.B, however, it is still possible to identify the rotational lines from these spectra.

The advantages of using the technique described in this section is firstly that it gives a clear indication of the amount of VUV light generated during measurements and secondly will also generate baselines for not only the absorption spectra but also for the rotational excitation spectra thus making it possible to eliminate artefacts caused as a result of signal processing. The disadvantage of this technique is that measurements will take twice as long to be able to have the same statistical accuracy as before.

4.6.3 New measuring technique for absorption free rotational excitation spectra

In Section 4.5 the impact of self-absorption on the vibrational spectra was discussed. Self-absorption also influences the measured peak intensity of rotational excitation spectra. It is important to note that the absorption coefficient is different for each excitation line due to differences in the population of the rovibronic levels in the ground electronic state. Accurate thermal information about the supersonic gas jet can be extracted from the rotational excitation spectra if the peak intensities measured is not modified by self-absorption.

The analysis of the fluorescence spectra in Section 4.4 can be used to solve this problem. In the fluorescence spectra, the $A^1\Pi(v' = 3) - X^1\Sigma^+(v'' = 2)$ vibronic band has a large intensity and does not undergo self-absorption. The scanning monochromator can be used as a wavelength filter by fixing the scanning monochromator to the $A^1\Pi(v' = 3) - X^1\Sigma^+(v'' = 2)$ band and by scanning the tuneable dye laser to generated a rotational excitation spectrum. With this method, it is possible to measure two excitation spectra simultaneously, where the first spectrum would be with self-absorption using PMT 1 (Figure 3.3) and second spectrum would be a self-absorption free spectrum measured using PMT 2 which records only the fluorescence in the band selected by the monochromator. Figures 4.31 shows the two spectra.
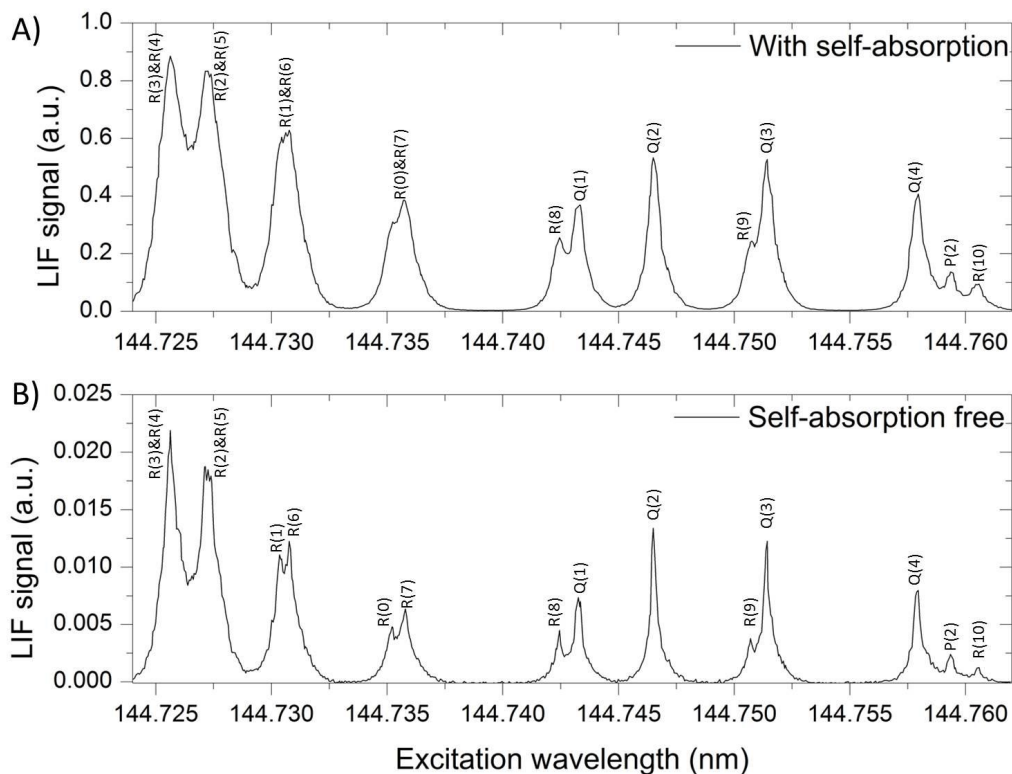
Figure 4.31: Rotational excitation spectra for $X^1\Sigma^+(v''=0, J''=n) - A^1\Pi(v'=3, J'=n, n\pm1)$ band of $^{12}C^{16}O$ A) with self-absorption and B) self-absorption free.

In Figure 4.31 it can firstly be noted that there is a clear spectral resolution increase in the self-absorption free spectrum compared to the spectrum with self-absorption, seen in the decreases of the FWHM of the $Q(2)$ line from $0.73\,\mathrm{pm}$ to $0.42\,\mathrm{pm}$ (43.10% decrease). This can be contributed to the optical properties of the scanning monochromator as the entrance slit of the scanning monochromator is vertical and the entrance slit is imaged onto the exit slit, thus only light from the center part of the supersonic gas jet will be detected. This is ideal as the sides of the supersonic gas jet would undergo some Doppler broadening, as the gas expands to towards the incoming light it would undergo a blueshift and as the gas expands away from the incoming light it would undergo a redshift. Using the scanning monochromator eliminates some of this effect, since the scanning monochromator does not only act as a wavelength filter but also as a spatial filter.

It can also be observed in Figures 4.31 that the relative intensity of the self-absorption free spectrum is 30 times smaller than the spectrum with self-absorption. This reduction in intensity can firstly be contributed to the fact that for the self-absorption free spectrum only the $A^1\Pi(v'=3) - X^1\Sigma^+(v''=2)$ transition is measured, whilst for the spectrum with self-absorption all of the vibrational transitions are measured ($A^1\Pi(v'=3) - X^1\Sigma^+(v''=n)$), thus approximately only 30% of all fluorescence is measured for the self-absorption free spectrum. Secondly, the optical path of the fluorescence for self-absorption free spectrum is 8 times longer than the

spectrum with self-absorption. The self-absorption free rotational excitation spectrum also interacts with 5 more optics than the spectrum with self-absorption, these factors could contribute to the decrease in the fluorescence signal measured for the self-absorption free spectrum.

Since the self-absorption free spectrum and the spectrum containing self-absorption are measured simultaneously, the intensity of VUV light is the exact same for both spectra, for each data point. The number of molecules excited and the amount of fluorescence emitted during de-excitation is also the same for both spectra. With this information, it is possible to compare these two spectra directly without having to use any adjustment factors for the VUV intensity or the fluorescence emission.

It is possible to investigate the amount of self-absorption occurring for individual rotational excitation lines. Since the amount of fluorescence emitted is the same for both spectra during measurements, it is possible to compare the self-absorption free spectrum with the spectrum that contains self-absorption. By dividing the peak intensities of the self-absorption free spectrum by the peaks of the spectrum that is affected by self-absorption, a measure of the degree of self-absorption for each peak is obtained. This is graphed in Figure 4.32.
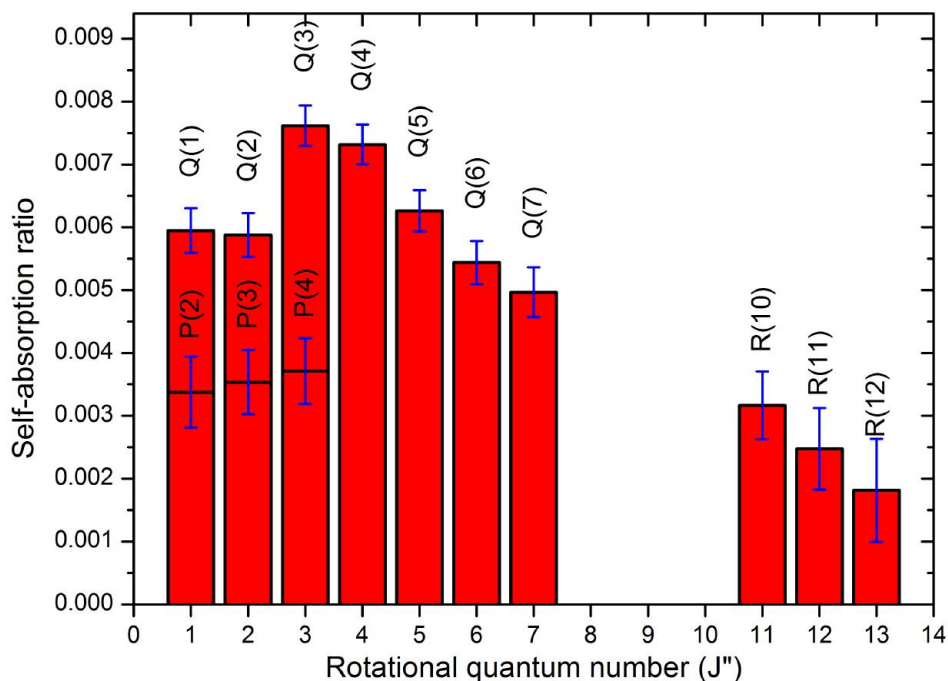
Figure 4.32: Ratio between self-absorption free peak and peak of spectrum affected by self-absorption.

Self-absorption has an effect on the rotationally resolved excitation spectra too, by influencing the relative peak heights. To analyse this the relative population of the rotational levels of the $X^1\Sigma^+(v''=0)$ state must be considered. At typical temperatures in the supersonic gas jet ($\sim$100 K) the rotational population distribution is given by Figure 4.33.
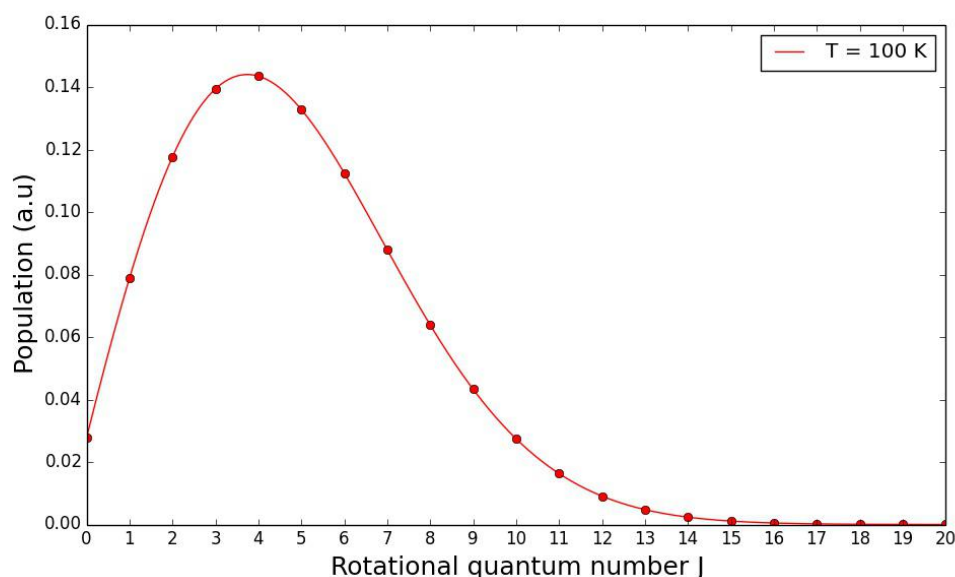
Figure 4.33: Expected Boltzmann distribution for CO sample at a $100\,\mathrm{K}$.

This means that the fluorescence of the molecules that de-excite to final states with $J'' = 3$ and $J'' = 4$ will undergo the most self-absorption, as these states have the largest population. The final states to which a specific excitation transition will de-excite is governed by the selection rules for rovibronic transitions ($\Delta J = 0, \pm 1$) as illustrated by the selected excitation transitions listed in Table 4.10. Note that we assume that there is no rotational relaxation in the excited state before de-excitation, as is observed from the vibrational dynamics.

From Table 4.10 it can be concluded that, for example, the excitation lines $R(0)$, $Q(1)$ and $P(2)$ must be affected by self-absorption to a similar degree as these 3 transitions lead to de-excitation back to the same 3 rotational levels with $J'' = 0, 1, 2$. For that reason, $Q(1)$ and $P(2)$ are plotted in the same column in Figure 4.32. The lines $R(2)$, $Q(3)$ and $P(4)$ lead to the de-excitation to the $J'' = 2, 3, 4$ rotational levels that have the highest population at $100\,\mathrm{K}$ and are therefore affected most by self-absorption as seen in Figure 4.32.

4.6.4   Temperature of supersonic gas jet

Before the self-absorption free rotational excitation spectra can be used to determine the temperature of the supersonic gas jet, it is necessary to determine when in the temporal development of the supersonic gas jet the excitation is occurring. The supersonic gas jet has a temporally changing velocity distribution and gas temperature as the jet is formed. This is of importance since the temperature in the supersonic gas jet would initially be higher (when the valve opens) compared to when the supersonic gas jet has fully formed (valve is open) and higher once again when the pulsed valve is closing. Assuming that the rotational populations are in (partial) thermal equilibrium the rotational temperature of the gas can be calculated directly

Table 4.10: Transition pathways for selected excitation lines.

Excitation transition	Allowed de-excitation transition	Final state of de-excitation (J'' value)
$R(0)$	$R(0)$, $Q(1)$, $P(2)$	0, 1, 2
$R(1)$	$R(1)$, $Q(2)$, $P(3)$	1, 2, 3
$R(2)$	$R(2)$, $Q(3)$, $P(4)$	2, 3, 4
$R(3)$	$R(3)$, $Q(4)$, $P(5)$	3, 4, 5
$R(4)$	$R(4)$, $Q(5)$, $P(6)$	4, 5, 6
$R(5)$	$R(5)$, $Q(6)$, $P(7)$	5, 6, 7
$Q(1)$	$R(0)$, $Q(1)$, $P(2)$	0, 1, 2
$Q(2)$	$R(1)$, $Q(2)$, $P(3)$	1, 2, 3
$Q(3)$	$R(2)$, $Q(3)$, $P(4)$	2, 3, 4
$Q(4)$	$R(3)$, $Q(4)$, $P(5)$	3, 4, 5
$P(2)$	$R(0)$, $Q(1)$, $P(2)$	0, 1, 2
$P(3)$	$R(1)$, $Q(2)$, $P(3)$	1, 2, 3
$P(4)$	$R(2)$, $Q(3)$, $P(4)$	2, 3, 4

from the spectral line intensities. It is expected when exciting the gas in the fully formed supersonic gas jet the population distribution would be concentrated in the lower rotational levels.

It is possible to measure the temporal population profile of the supersonic gas jet by varying the time delay between the pulsed valve and the laser pulse (Figure 3.11). The tuneable dye laser was set to a specific rovibronc excitation wavelength, in this case the $Q(2)$ ($X^1\Sigma^+(v''=0, J''=2) - A^1\Pi(v'=3, J'=2)$) and $P(9)$ ($X^1\Sigma^+(v''=0, J''=9) - A^1\Pi(v'=3, J'=8)$) excitation. These excitation lines were selected to investigate the different population distributions between the lower $J''=2$ and higher $J''=9$ levels. The fluorescence was measured at each value of the time delay as can be observed in Figure 4.34.

In Section 2.2.1.2 the Boltzmann equation was discussed and how the population of rotational level can give an indication of the supersonic gas jet temperature. The relative intensity in Figure 4.34 is an indication of the population for the $J''=2$ and $J''=9$ rotational levels, thus a higher relative intensity indicates a higher population. A higher population in the $J''=2$ rotational level would indicate a colder region in the supersonic gas jet compared to a higher population in the $J''=9$ rotational level. This can also be observed in Figure 2.11 where the Boltzmann distribution was plotted for different rotational temperatures.
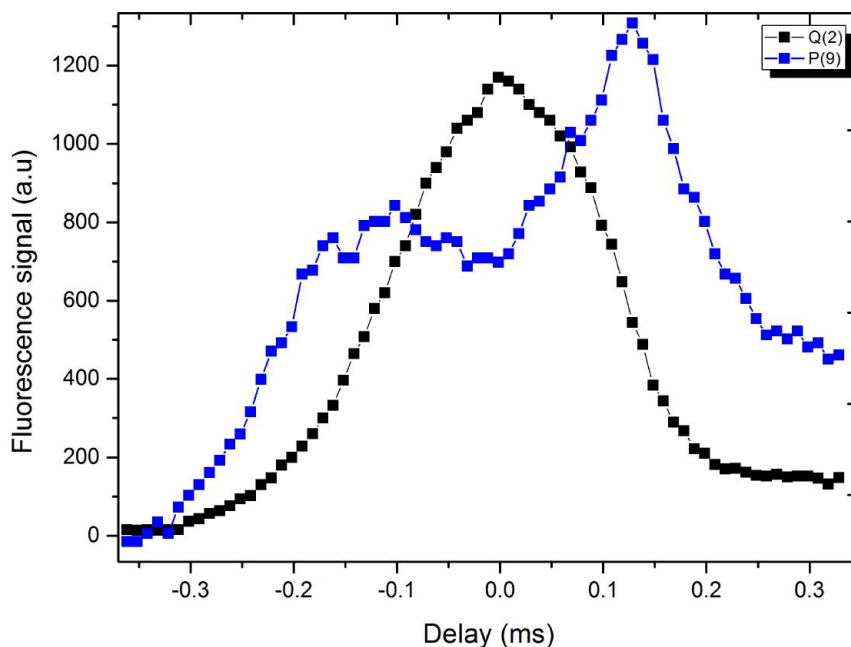
Figure 4.34: Fluorescence of CO following excitation of the $Q(2)$ and $P(9)$ lines of the $A^1\Pi(v' = 3) - X^1\Sigma^+(v'' = 0)$ band for different time delays between the supersonic gas jet and laser pulse.

Time zero in Figure 4.34 refers to the original relative time delay used between the laser pulse and supersonic gas jet for previous measurements. The supersonic gas jet delay scan for the $Q(2)$ excitation line is semi-symmetrical around zero. The relative intensity at -0.3 ms is lower than the signal at 0.3 ms, this is as a result of some gas remaining in the vacuum system after the gas pulse. The signal at 0.3 ms continued at approximately the same intensity up until 0.6 ms. For the $Q(2)$ excitation line the highest intensity was recorded at time 0.

In the supersonic gas jet delay scan for the $P(9)$ excitation line the relative intensity at -0.3 ms is lower than the signal at 0.3 ms, this is once again as a result of gas remaining in the system after the pulse. The background gas would be at a higher temperature compared to the gas in the supersonic gas jet, thus leading to the noticeable difference in the relative intensity between the $Q(2)$ and $P(9)$ excitation lines after the pulse (at 0.3 ms). It was further observed that the relative intensity after 0.3 ms continued up to 0.6 ms. The delay scan of the supersonic gas jet for the $P(9)$ excitation line is not symmetrical around time zero. It can be noted that the peak to the right of time zero is larger than the peak to the left of time zero. This is as a result of the supersonic gas jet being increasingly influenced by the rise in the background gas pressure during the duration of the gas pulse, thus leading to more collision and an increase in the temperature of the sample.

Previous studies done in our laboratory by C.M. Steinmann [23] and A. du Plessis [24] has shown that increasing the pressure of the stagnant CO gas leads to a decrease in the temperature, thus leading to an increase in the population of the lower rotational levels. Additionally, it was observed that when using a monatomic buffer

gas like argon (Ar) and a low percentage of CO gas (0.6%) that the temperature of the supersonic gas jet decreases. However, using such a low percentage of CO gas also leads to a decrease in fluorescence signal thus increase the signal to noise ratio. Using such a low percentage of CO gas would also lead to less self-absorption as the probability of self-absorption would decrease.

With this knowledge, it is possible to optimize the population distribution of the high or low rotational levels, for example, to have higher populations in the lower rotational levels the delay between the laser pulse and gas pulse needs to be set to zero and the pressure of the stagnant sample gas needs to be as high as possible (4 bar in our laboratory). Additionally, a high concentration (99.4% Ar and 0.6% CO) of buffer gas can also be used. To populate the higher rotational levels ($J = 9$) the delay between the laser pulse and gas pulse needs to be set to 0.16 ms and the pressure of the stagnant gas needs to be set as low as possible with no buffer gas. Using a pure CO gas sample would lead to more self-absorption but at the same time would also lead to an increase in the fluorescence signal. It was decided that zero delay between the supersonic gas jet and the laser pulse will be used in order to populate the lower rotational levels of the $X^1\Sigma^+$ state.

In Figures 4.35.A & 4.35.B the rotational excitation spectra can be observed which will be used for temperature calculations. These spectra were measured using pulse value at 5 Hz with a pure CO gas sample at 1.3 bar. Figure 4.35.A shows a spectrum that is affected by self-absorption and was previously the standard method used for measuring rotational excitation spectra in our laboratory. Figure 4.35.B shows a self-absorption free spectrum and was measured using the technique described in Section 4.6.3. It is important to note that only peaks which were clearly distinguishable where selected for the temperature calculations.
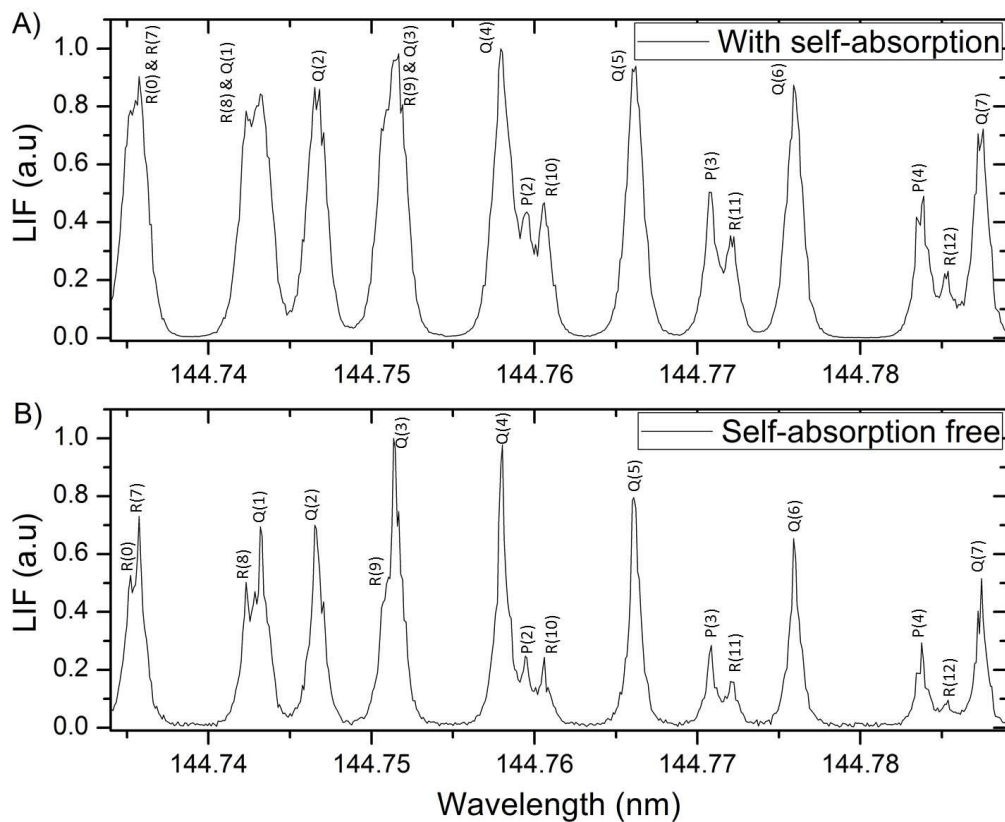
Figure 4.35: Rotational excitation spectra for $X^1\Sigma^+(v''=0, J''=n) - A^1\Pi(v'=3, J'=n, n\pm 1)$ band of $^{12}C^{16}O$, A) with self-absorption and B) self-absorption free.

From Figure 4.35 it can be observed that it is possible to distinguish more peaks in the self-absorption free spectrum compared to the spectrum which is affected by self-absorption. This is as a result of the self-absorption free spectrum having a higher spectral resolution. After all the peak intensities were determined the Hönl London factors given by Equation (2.2.6) were applied. The Boltzmann relation given by Equation (2.2.7) was then used to generated Figures 4.36.A & 4.36.B.
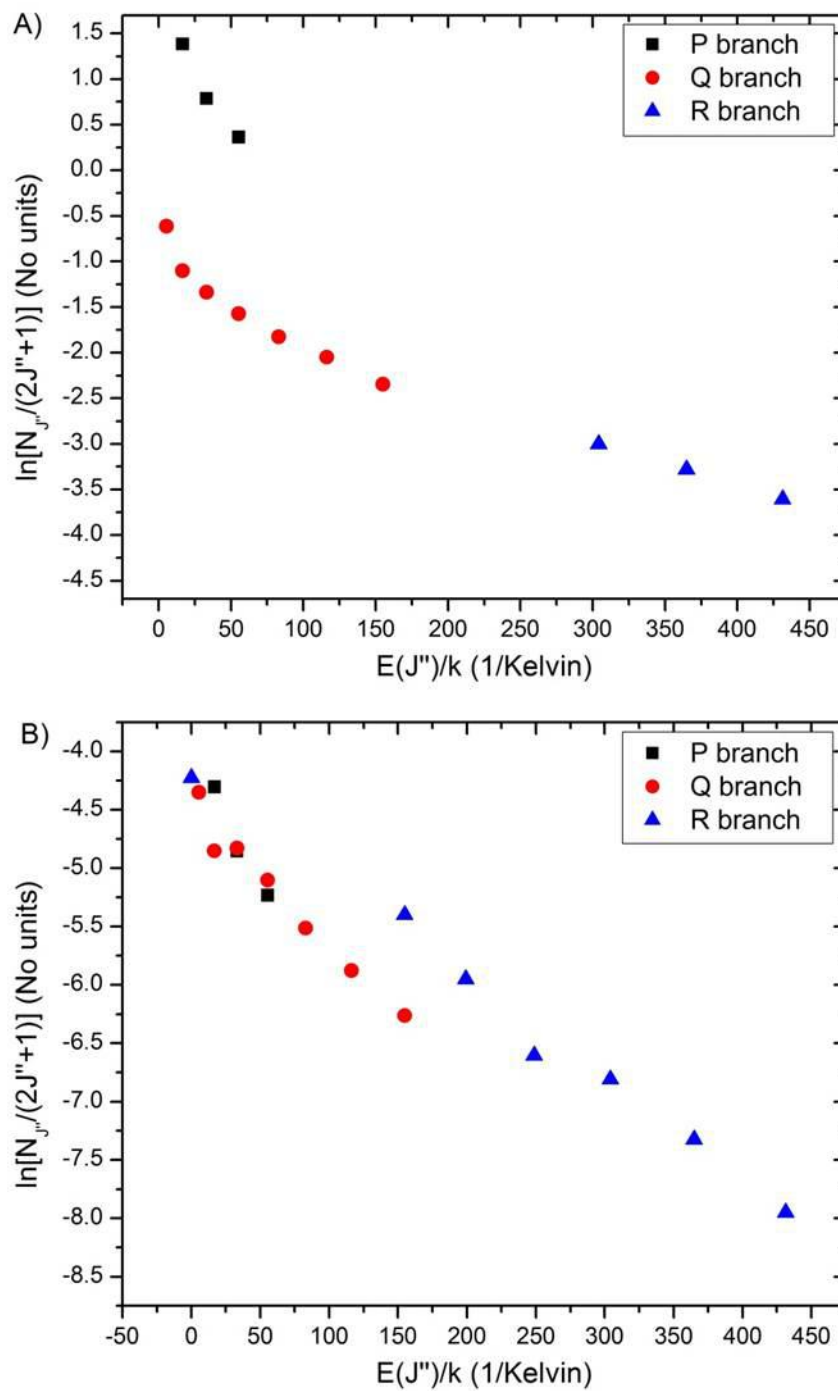
Figure 4.36: Boltzmann plot for different rotational branches using data from A) spectrum affected by self-absorption and B) self-absorption free spectrum.

It can be observed that there exists a significant difference between Figures 4.36.A & 4.36.B. The values in Figure 4.36.A for the different rotational branches are spread

out along the y-axis with different slopes from one another, whilst the values in Figure 4.36.B are closely spaced along the y-axis and the slopes of the individual rotational branches agree with each other.

It is clear from Figure 4.36.A that the different branches can not be joined to one linear line. It can be observed for the Q-branch data that it forms a curve. When fitting a line through the Q-branch the data selected (which J'' numbers are included) will have a large influence on the line's slope and therefore what the apparent temperature would be. For example, if the lowest 4 data points of the Q-branch is used a much larger slope (lower temperature) will be observed compared to using the last 4 data points of the same set of data (Figure 4.37). From Figure 4.37 the a temperature of 56 K was calculated when using the lowest 4 data points of the Q-branch and a temperature of 131 K was calculated when using the last 4 data points of the Q-branch, more than double the temperature calculated when using the lowest 4 data points.
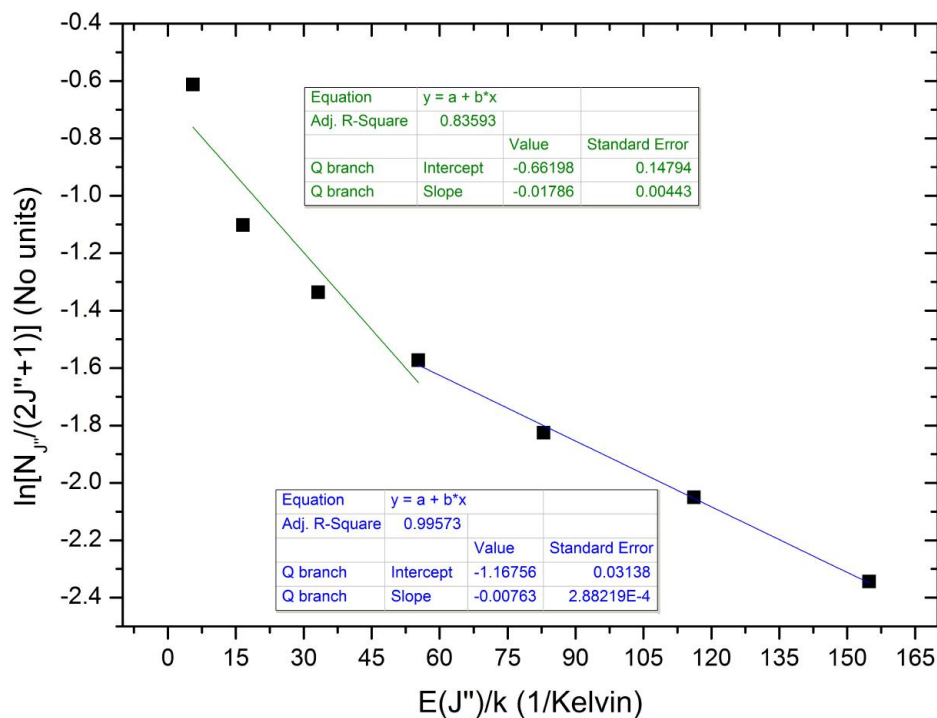
Figure 4.37: Linear fit through Boltzmann plot for the Q-branch using lowest 4 data points (green line) and last 4 data points (blue line).

Thus, it is not possible to determine any thermal information for spectra which are affected by self-absorption. The non-linear behaviour observed in Figure 4.38.A was previously noted in studies done by Steinmann [23] and Smalley et al. [39]. At that time, it was unclear what the cause of the non-linear behave was however, it is now clear that self-absorption was the cause of the non-linearity observed.
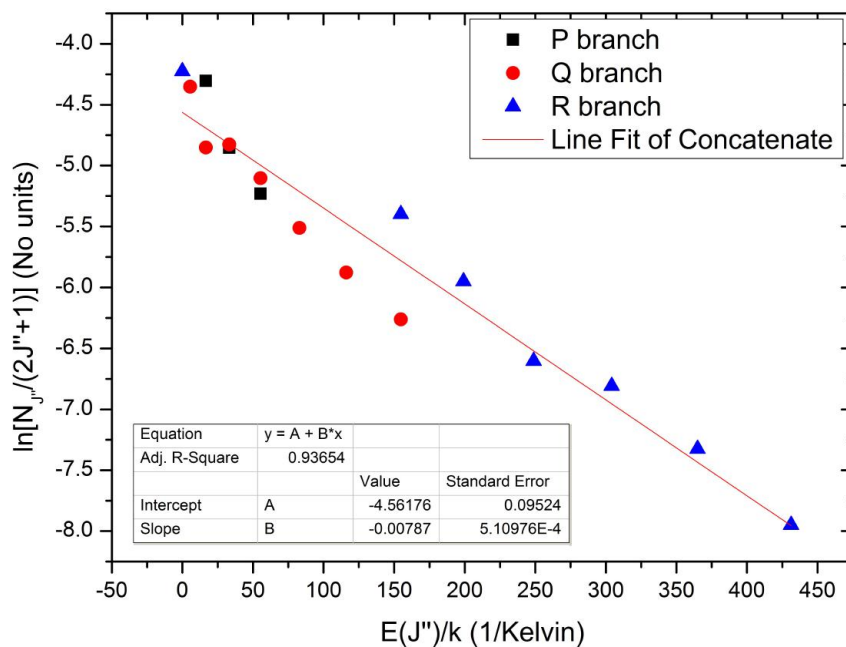
Figure 4.38: Linear fit through Boltzmann plot for different rotational branches using data from self-absorption free spectrum.

From the linear fit in Figure 4.38, it was determined that the temperature of the supersonic gas jet was $127\,\mathrm{K}$ when using data from the self-absorption free spectrum.

The difference in the measured temperatures of the supersonic gas jet can easily be explained when considering the Boltzmann distribution at these temperatures (Figure 4.39).
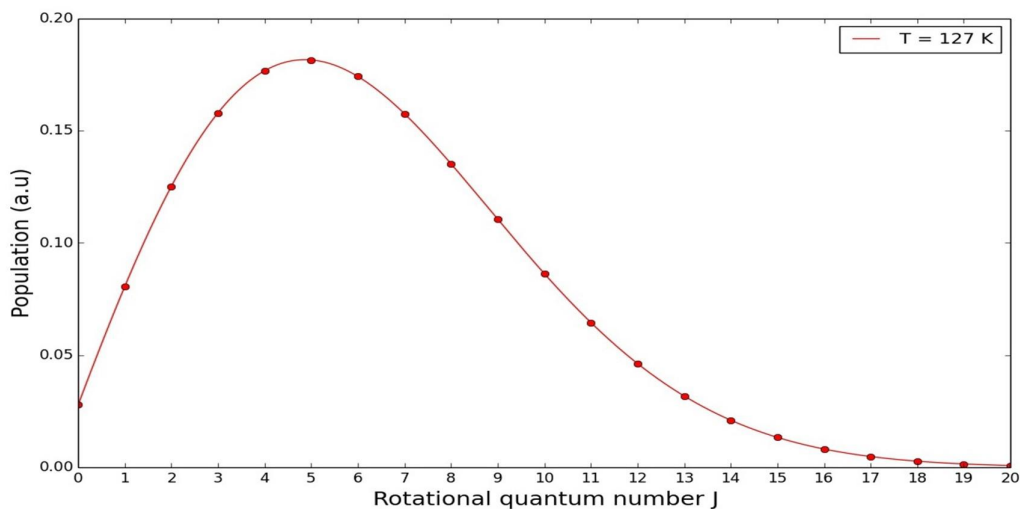
Figure 4.39: Expected Boltzmann distribution for measured temperatures of CO sample.

It can be observed from Figure 4.39 that the 5th rotational level was the highest populated. The amount of self-absorption is proportional to the population of a rotational level, thus the de-excitations returning to the 5th rotational level would be affected more by self-absorption compared to rotational levels with lower populations. In this case, both the lower ($J'' > 5$) and the higher ($J'' < 5$) rotational levels have lower populations than $J'' = 5$. The impact this has on the thermal calculations for the spectrum containing self-absorption is that if only the $J'' \leq 5$ rotational levels are used then the thermal information of the supersonic gas jet would indicate a lower temperature compared to the true temperature of the supersonic gas jet. The opposite is true as well if only the $J'' \geq 5$ rotational levels are used then the thermal information of the supersonic gas jet would indicate a higher temperature compared to the true temperature of the supersonic gas jet.

This was investigated by re-evaluating the data analysis done in Figure 4.38.A. It was found that if the $J'' \leq 5$ rotational levels were used that the temperature of the supersonic gas jet was 70 K and if the $J'' \leq 5$ rotational levels were used that the temperature of the supersonic gas jet was 202 K, this confirms the statements previously mentioned.

The measured rotational temperature was used to do calculations associated with the supersonic gas jet. In Section 2.3 the supersonic gas jet was discussed and the equation which can be used when the translational temperature ($T_\parallel$) is known. As it is not possible to measure the translational temperature in our laboratory, it was necessary to use the rotational temperature (T_r) to determine lower and upper bounds for the equations in Section 2.3. This was achieved by rewriting the equations in Section 2.3 in terms of T_r (Appendix A.4) taking T_r as the upper limit of $T_\parallel$.

Table 4.11: Calculated values of parameters associated with the supersonic gas jet from of the measured rotational temperature of 127 K.

Parameter	Type of limit	Value	Units
M_{eff}	Lower limit	2.56	N/A
Effective speed of sound	N/A	230	m/s
Effective speed of gas	Lower limit	587	m/s
Maximum speed of gas	Upper limit	594	m/s
X_{eff}	Lower limit	0.55	mm
n_{eff}	Upper limit	$0.12n_0$	N/A

In Table 4.11 the calculated parameters of the supersonic gas jet can be observed. These values were calculated by using the equations in Appendix A.4 and a rotational temperature of 127 K. It was possible to calculate the effective speed of the gas in the supersonic gas jet by firstly calculating the effective Mach number (M_{eff}) and secondly calculating the effective speed of sound. As there are no collisions in the silent zone (Figure 2.13) of the supersonic gas jet, the ideal gas approximations

can be used, thus the effective speed of sound was calculated using the ideal gas Equation (A.4.5). Additionally, it was possible to calculate a theoretical upper limit for the effective speed of the gas using the equipartition theorem. Since CO has 3 translational degrees of freedom and 1 rotational degree of freedom (vibration degree of freedom does not contribute at room temperature or lower) this leads to:

$$4\left(\frac{1}{2}kT_0\right) = \frac{1}{2}mv^2,$$ (4.6.1)

where k is Boltzmann constant, T_0 temperature of stagnant gas before expansion, m the mass of CO and v is the speed of the gas. Using Equation (4.6.1) it was determined that upper limit of the speed of the gas was $594\,\text{m/s}$. The speed calculated by the equipartition theorem is higher than that given in Table 4.11, this is because all the thermal energy is not fully converted into translational energy and thus some rotational energy remains.

The lower limit for the effective translational distance from the orifice to the position where the laser pulse will interact with the supersonic gas jet (X_{eff}) was determined to be $0.55\,\text{mm}$. When measuring the true distance between the orifice and the laser pulse it was determined that this distance was $1.4\,\text{mm}$. The difference between the calculated value and the measured value was expected since the value calculated in Table 4.11 is only a lower limit.

It was lastly possible to determine an upper limit for the effective density of the gas interacting with the laser pulses (n_{eff}) in terms of the density of the stagnant gas. It was determined that the density of the gas interacting with the laser pulses is maximally 12% of the density of the stagnant gas.

Chapter 5

Summary and Conclusions

Calibration of dye lasers was successfully achieved using a hollow cathode lamp. This calibration was sufficient to determine the vibronic band and specific isotope of CO which was excited in the VUV region. However, this calibration was not sufficiently accurate to identify the different rotational excitation lines. Using literature values of known CO lines from Niu et al. [11], calibration of rotational excitation spectra was achieved. Upon investigation of the rotational excitation spectra for the $X^1\Sigma^+(v''=0)-A^1\Pi(v'=4)$ excitation band it was found that multiple singlet-triplet transitions of the $X^1\Sigma^+(v''=0)-a'^3\Sigma^+(v'=14)$ band were observed. One of these singlet-triplet transitions ($^PQ(2)$) measured in this study has previously been observed in our laboratory by du Plessis et al. [40]. However, for two of the singlet-triplet transitions, measured wavelengths are not available in peer-reviewed literature.

In this study investigation into two different models for diatomic molecules were done. It was determined that the Dunham coefficients are a more accurate approximation to the energy levels of a diatomic molecule compared to that of the Morse potential. The Morse potential was successfully programmed to calculate the Franck-Condon factors and the r-centroid values for all known transitions of the four isotopes $^{12}C^{16}O$, $^{13}C^{16}O$, $^{12}C^{18}O$ and $^{12}C^{17}O$.

For the first time in our laboratory, a setup to measure the fluorescence spectra of CO upon rovibronic excitation in the VUV region was implemented. The fluorescence spectra of $^{12}C^{16}O$ for $X^1\Sigma^+(v''=0)-A^1\Pi(v'=3)$ and $X^1\Sigma^+(v''=0)-A^1\Pi(v'=4)$ vibronic bands were measured successfully. From these measurements, vibrational constants were determined for the $X^1\Sigma^+$ state. The vibrational constants measured were within 1.8% compared to the values given by Velichko et al. [2] and Huber et al. [10]. Additionally, fluorescence spectra of $^{13}C^{16}O$ and $^{12}C^{18}O$ isotopes were successfully measured for the $X^1\Sigma^+(v''=0)-A^1\Pi(v'=3)$ excitation band. Coefficients for the electronic transition moment (R_e) as function of the r-centroid was successfully determined up to the 3rd order from the fluorescence spectra for the different isotopes.

Two new measuring techniques were successfully developed as part of this study. The first measuring technique developed allows for accurate measurement of the amount of VUV light generated during measurement and creation of a measured baseline. This technique additionally increases the spectral resolution (FWHM at peaks decrease from 0.93 pm to 0.72 pm (21.74%)). The spectral resolution increase

was a result of allowing additional time for background gas to be evacuated out of the vacuum system. The second measuring technique developed allows for self-absorption free rotational excitation measurements by using a scanning monochromator. The scanning monochromator is used as a wavelength filter thus allowing for measurement of the fluorescence in a specific vibronic band during rotational excitation. A spectral resolution increase (FWHM reducing from $0.72\,\text{pm}$ to $0.42\,\text{pm}$ (43.10%)) was observed in the rotational excitation spectra when using this technique. The spectral resolution increase was as a result of the scanning monochromator acting as a spatial filter, thus avoiding detection of light from regions in the supersonic gas jet which are affected by Doppler broadening.

The impact that self-absorption has on the measured rotational temperature of the supersonic gas jet was investigated. It was found that when using spectral information from spectra which are affected by self-absorption that the measured rotational temperature would depend on the amount of self-absorption and the selection of data, thus this rotational temperature can not be determined reliably. Spectral information from spectra which are self-absorption free can be used to determine the rotational temperature of the supersonic gas jet. The rotational temperature of the supersonic gas jet was determined to be $127\,\text{K}$. Using this temperature, it was possible to determine the Boltzmann distribution for the rotational levels. Additionally, values for parameters associated with the supersonic gas jet were calculated.

5.1 Future work

The following future work has the potential to be developed from the preceding thesis. The current experimental layout for vacuum ultraviolet spectroscopy (Section 3.2) could be extended by adding a second pulsed valve, thus allowing for two different gas samples to be measured simultaneously using the vacuum ultraviolet spectroscopy (Figure 5.1).
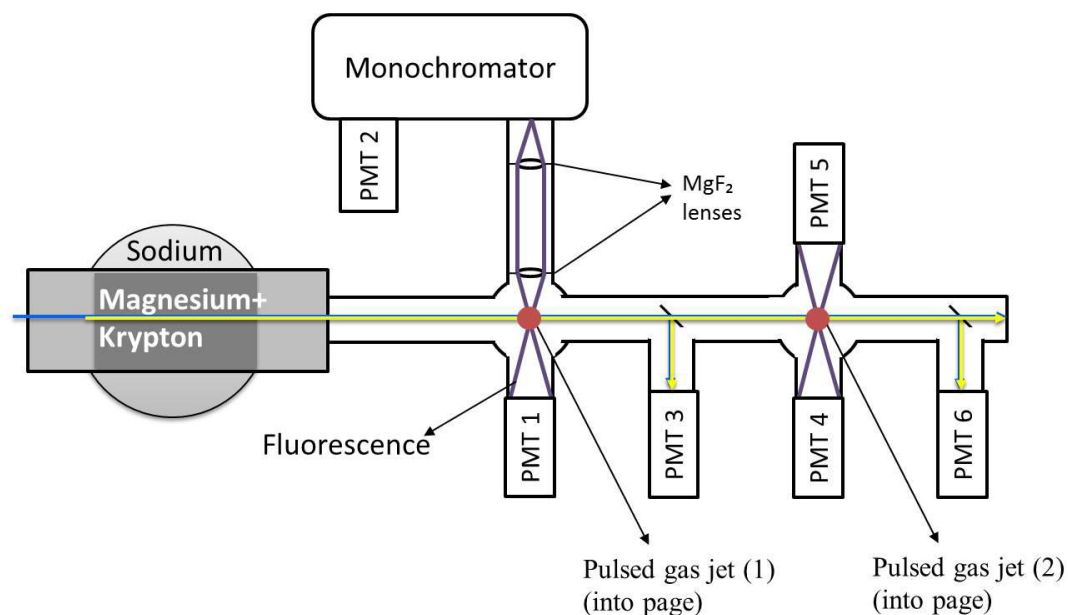
Figure 5.1: Future experimental layout for vacuum ultraviolet spectroscopy. Blue line visible light and Yellow line VUV light.

A possible application of the experimental layout in Figure 5.1 is to analyse a (partially) unknown gas mixture. This can be achieved if some components of the unknown gas mixture are known. The known components will then be used in gas jet (1) whilst the unknown gas mixture is used in gas jet (2). The frequency of the pulsed gas jet (1) will be set to 5 Hz and the frequency of pulsed gas jet (2) will be set to 10 Hz. This will allow recording of the rotational excitation spectra of both gas samples without interference from one another. Additionally, a spectrum will be recorded where the spectrum of pulsed gas jet (1) is subtracted from of the spectrum of pulsed gas jet (2). This spectrum can be used to identify the unknown gas as the spectrum recorded will be of the unknown gas only. This technique can also be applied to two independent gas samples, where the spectrum of a known gas in gas jet (1) can be used to calibrate the spectrum of gas jet (2).

Appendices

Appendix A

Results and tables

A.1 Sellmeier-type dispersion

The Sellmeier-type dispersion coefficients in Table A.1 were used to calculate the index of refraction in Section 3.2.1.

Table A.1: Sellmeier-type dispersion coefficients from [13].

i	λ_i (μm)	A_i (no units)
1	0.04338408	0.48755108
2	0.09461442	0.39875031
3	23.793604	2.3120353

A.2 Full table of results for Mores approximation

In Table A.2 the calculated vibronic transition energies, FCF's and r-centroid values using the Morse potential are given for the $A^1\Pi - X^1\Sigma^+$ band of $^{12}C^{16}O$. Additional calculated values for the vibronic transition energies, FCF's and r-centroid have been calculated for $^{12}C^{16}O$, $^{13}C^{16}O$ and $^{12}C^{18}O$ for the following bands:

101

$$A^1\Pi - a^3\Sigma^+ \qquad A^1\Pi - X^1\Sigma+$$
$$a^3\Sigma^+ - X^1\Sigma^+ \qquad a^3\Pi - A^1\Pi$$
$$a^3\Pi - a^3\Sigma^+ \qquad a^3\Pi - X^1\Sigma^+$$
$$D^1\Delta - A^1\Pi \qquad D^1\Delta - a^3\Sigma^+$$
$$D^1\Delta - a^3\Pi \qquad D^1\Delta - d^3\Delta$$
$$D^1\Delta - e^3\Sigma \qquad D^1\Delta - I^1\Sigma$$
$$D^1\Delta - X^1\Sigma+ \qquad d^3\Delta - A^1\Pi$$
$$d^3\Delta - a^3\Sigma^+ \qquad d^3\Delta - a^3\Pi$$
$$d^3\Delta - X^1\Sigma+ \qquad e^3\Sigma^- - A^1\Pi$$
$$e^3\Sigma - - a^3\Sigma+ \qquad e^3\Sigma^- - a^3\Pi$$
$$e^3\Sigma - - d^3\Delta \qquad e^3\Sigma^- - X^1\Sigma^+$$
$$I^1\Sigma^- - A^1\Pi \qquad I^1\Sigma^- - a^3\Sigma^+$$
$$I^1\Sigma^- - a^3\Pi \qquad I^1\Sigma - - d^3\Delta$$
$$I^1\Sigma - -e^3\Sigma \qquad I^1\Sigma^- - X^1\Sigma^+$$

which can be found at:`http://hdl.handle.net/10019.1/100636`. These values were calculated using the code in Appendix B and vibration constants from Herzberg et al. [10]. These values are discussed in the following sections of the thesis:

- vibronic transition energies in Table 4.3 (as wavelength),

- FCF's in Section 4.3.2, Table 4.3 and Figure 4.17,

- r-centroid values in Figure 4.18.

Table A.2: All calculated values for the $A^1\Pi - X^1\Sigma^+$ band of ^{12}C^{16}O using Morse potential. First row entry: Vibronic energy, Second row entry: Franck-Condon factor, Third row entry: r-centroid value.

$\frac{v'}{v''}$	$A^1\Pi - X^1\Sigma^+$ Vibronic transition energy (cm^{-1}) FCF r-Centroid								
	0	1	2	3	4	5	6	7	8
0	64748.46	62605.22	60488.56	58398.47	56334.97	54298.04	52287.68	50303.91	48346.70
	0.1084	0.2570	0.2849	0.1986	0.0987	0.0375	0.0114	0.0029	0.0006
	1.1816	1.2101	1.2395	1.2693	1.2993	1.3293	1.3591	1.3888	1.4184
1	66227.90	64084.66	61968.00	59877.91	57814.41	55777.48	53767.12	51783.35	49826.14
	0.2023	0.1585	0.0052	0.0679	0.1872	0.1889	0.1159	0.0508	0.0172
	1.1618	1.1890	1.2131	1.2491	1.2781	1.3077	1.3373	1.3668	1.3962
2	67668.54	65525.30	63408.64	61318.55	59255.05	57218.12	55207.76	53223.99	51266.78
	0.2159	0.0187	0.0768	0.1226	0.0110	0.0420	0.1514	0.1706	0.1128
	1.1432	1.1660	1.2002	1.2275	1.2546	1.2876	1.3164	1.3456	1.3748
3	69070.38	66927.14	64810.48	62720.39	60656.89	58619.96	56609.60	54625.83	52668.62
	0.1751	0.0099	0.1396	0.0051	0.0728	0.0972	0.0062	0.0419	0.1391
	1.1257	1.1602	1.1800	1.2012	1.2383	1.2662	1.2933	1.3258	1.3543
4	70433.42	68290.18	66173.52	64083.43	62019.93	59983.00	57972.64	55988.87	54031.66
	0.1210	0.0622	0.0505	0.0367	0.0813	0.0001	0.0814	0.0743	0.0013
	1.1093	1.1384	1.1600	1.1929	1.2178	1.2832	1.2766	1.3049	1.3295
5	71757.66	69614.42	67497.76	65407.67	63344.17	61307.24	59296.88	57313.11	55355.90
	0.0758	0.0996	0.0026	0.0846	0.0065	0.0639	0.0468	0.0080	0.0872
	1.0940	1.1214	1.1287	1.1734	1.1932	1.2298	1.2565	1.2888	1.3152
6	73043.10	70899.86	68783.20	66693.11	64629.61	62592.68	60582.32	58598.55	56641.34
	0.0446	0.1045	0.0100	0.0614	0.0169	0.0636	0.0025	0.0748	0.0184
	1.0798	1.1059	1.1400	1.1551	1.1886	1.2105	1.2477	1.2682	1.2952
7	74289.74	72146.50	70029.84	67939.75	65876.25	63839.32	61828.96	59845.19	57887.98
	0.0253	0.0889	0.0403	0.0179	0.0579	0.0100	0.0518	0.0266	0.0226
	1.0666	1.0916	1.1201	1.1353	1.1691	1.1887	1.2236	1.2489	1.2804
8	75497.58	73354.34	71237.68	69147.59	67084.09	65047.16	63036.80	61053.03	59095.82
	0.0140	0.0669	0.0635	0.0001	0.0603	0.0052	0.0550	0.0026	0.0610
	1.0544	1.0784	1.1049	1.0120	1.1522	1.1896	1.2057	1.2427	1.2621

A.3 r-Centroid approximation of different isotopomers of CO

The polynomial fits used to determine the vibrational constants for ^{12}C^{18}O and ^{13}C^{16}O of the $X^1\Sigma^+$ state can be observed in Figure A.1. The linear fits used determine the r-centroid coefficients for ^{12}C^{18}O and ^{13}C^{16}O of the $A^1\Pi(v' = 3) - X^1\Sigma^+(v'' = n)$ band can additionally be observed in Figure A.1. The results of these Figure A.1 are summarised in Table 4.6.

A.4 Supersonic gas jet equations

The equations in Section 2.3 can be re-written in terms of the rotational temperature since the translational temperature and the rotational temperature have the following relationship $T_\parallel < T_r$. Using this relationship Equation (2.3.3) can be re-written into

the following form:

$$T_r < T_0 \left[1 + \frac{1}{2}(\gamma - 1) M_{eff}^2 \right]^{-1}. \tag{A.4.1}$$

The upper/lower limit of effective Mach number can be determined by making M_{eff} the subject of Equation (A.4.1), which leads to:

$$M_{eff} > \sqrt{\frac{2}{\gamma - 1} \left(\frac{T_0}{T_r} - 1 \right)}. \tag{A.4.2}$$

The effective Mach number from Equation (A.4.2) will give a lower limit, thus the Mach number must be larger than the value given by Equation (A.4.2).

The distance from the orifice where the laser pulse will interact with the supersonic gas jet can also be written in terms of the rotational temperature and is given by:

$$X_{eff} > D \left[\frac{1}{3.26} \sqrt{\frac{2}{\gamma - 1} \left(\frac{T_0}{T_r} - 1 \right)} \right]^{\frac{1}{0.67}}. \tag{A.4.3}$$

The effective distance given by Equation (A.4.3) is a lower limit, thus the effective distance must be larger than the value given by Equation (A.4.3).

Lastly, the effective density can also be re-written in terms of the rotational temperature and is give by:

$$n_{eff} < n_0 \left(\frac{T_r}{T_0} \right)^{\frac{1}{\gamma - 1}}. \tag{A.4.4}$$

The effective density given by Equation (A.4.4) is an upper limit, thus the effective density must be less than the value given by Equation (A.4.4).

The speed of sound in an ideal gas can be calculated using the following equation:

$$\text{Speed of sound} = \sqrt{\frac{\gamma R T_r}{M}}, \tag{A.4.5}$$

where R is the molar gas constant ($8.315 \, \text{J} \, \text{mol}^{-1} \, \text{K}^{-1}$) and M is the molar mass of the gas.
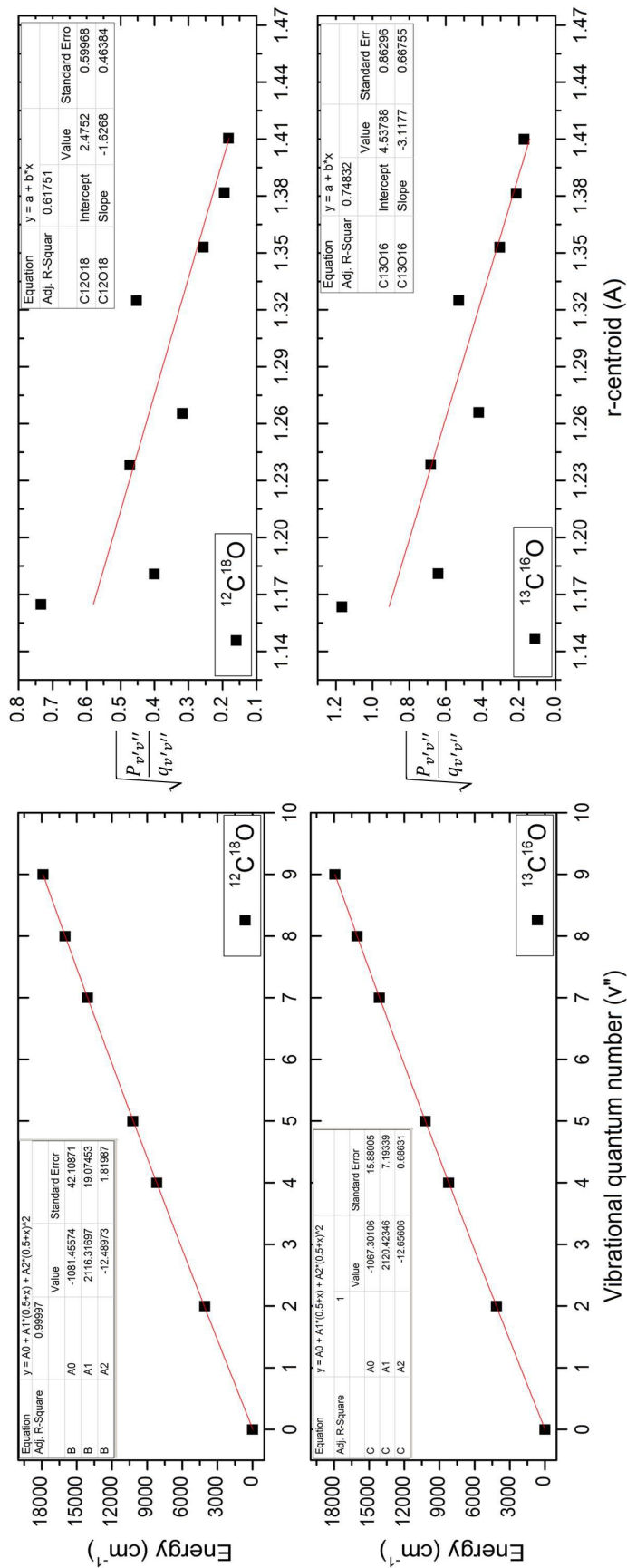
Figure A.1: Vibrational constants and r-centroid fits of different isotopomers of CO for the $A^1\Pi(v'=3) - X^1\Sigma^+ v''=n$ band. Left hand side: Polynomial fits for calculation of vibrational constants for $^{12}C^{18}O$ and $^{13}C^{16}O$. Right hand side: Linear fits for the r-centroid approximation of the electronic transition moment for $^{12}C^{18}O$ and $^{13}C^{16}O$.

Appendix B

Morse potential model of CO: code

This code was used to calculate the potential energy curves and the vibronic wave functions of $^{12}C^{16}O$, $^{12}C^{18}O$ and $^{13}C^{16}O$ as discuses in Sections 2.2.2 & 4.3.

```
Clear["Global*"]
(************** * **Constenst ********** * * * *****)
eVtoCm1 = 8065.54429;
Cm1toJ = 1.98644561 * 10^-23;
eVtoJ = 1.602176532 * 10^-19;
AtomicMassUnit = 1.66053886 * 10^-27;
h = 6.6260693 * 10^-34;
c = 299792458;
ℏ = h/(2π);


Cabon12 = 12.00000000;
Cabon13 = 13.00335440;
Oxigan16 = 15.99491502;
Oxigan18 = 17.9916002;
```

$$ReducedMassC12O16 = \frac{(Cabon12*Oxigan16)}{(Cabon12+Oxigan16)};$$
$$ReducedMassC13O16 = \frac{(Cabon13*Oxigan16)}{(Cabon13+Oxigan16)};$$
$$ReducedMassC12O18 = \frac{(Cabon12*Oxigan18)}{(Cabon12+Oxigan18)};$$

μAll = {ReducedMassC12O16, ReducedMassC13O16, ReducedMassC12O18};

```
(******* * *Selectwhichisotope : Isotope = 1forC12O16********)
Isotope = 1;
```

$$\rho = \sqrt{\frac{\mu All[[1]]}{\mu All[[Isotope]]}};$$

μ = μAll[[Isotope]] * AtomicMassUnit;

106

```
(*********************Constentsforpotantial****** * ***************)
NameFrom = {"X¹Σ⁺ - ","a³Σ⁺ - ","A¹Π - ","a³Π - ","d³Δ - ","e³Σ⁻ - ",
"I¹Σ⁻ - ","D¹Δ - "};
NameTo = {"X¹Σ⁺","a³Σ⁺","A¹Π","a³Π","d³Δ","e³Σ⁻","I¹Σ⁻","D¹Δ"};

(*********************Datafrom[10]****** * ***************)
```

$r_e = \{1.128323, 1.3523, 1.2353, 1.20574, 1.3696, 1.3840, 1.3911, 1.399\};$

$\omega_e = \{\rho 2169.81358, \rho 1228.6, \rho 1518.24, \rho 1743.41, \rho 1171.94,$
$\rho 1117.72, \rho 1092.22, \rho 1094.0\};$

$\omega\chi_e = \{\rho^2 13.28831, \rho^2 10.468, \rho^2 19.4, \rho^2 14.36, \rho^2 10.635,$
$\rho^2 10.686, \rho^2 10.704, \rho^2 10.20\};$

$\text{De}_{eV} = \{\rho^4 11.22609941, \rho^4 4.30462108, \rho^4 3.157732579, \rho^4 5.189832507,$
$\rho^4 3.648173132, \rho^4 3.262564934, \rho^4 3.052069531, \rho^4 3.156662596\};$

$T_e = \{0, 55825.49, 65075.77, 48684.70, 61120.1, 64230.24, 65084.40, 65928\};$

```
(*********************Morse****** * ***************)
```

$\text{WaveFuntionMorse}[r\_, v\_] = \text{Table}[$

$D_e = \text{De}_{eV}[[i]]\text{eVtoCm1};$

$V_o = D_e\text{Cm1toJ};$

$\beta = \left(\omega_e[[i]]\sqrt{\frac{2\pi^2 c\mu}{hD_e}}\right) 10^{-9};$

$\text{cc} = \text{Floor}\left[\sqrt{\frac{(8\mu V_o)}{\beta^2\hbar^2}}10^{-10}\right];$

$y[r\_] = \text{Function}\left[u, \text{cc}e^{-\beta(u-r_e[[i]])}\right][r];$

$s[v\_] = \text{Function}\left[w, \frac{cc}{2} - w - \frac{1}{2}\right][v];$

$\text{NormFactor}[v\_] = \text{Function}\left[w, \sqrt{\frac{\beta 2s[w]}{}}\right][v];$

$\text{WaveFuntions}[r\_, v\_] = \text{Function}[\{u, w\},$

$\text{NormFactor}[w]e^{\frac{-y[u]}{2}}y[u]^{s[w]}\right][r, v], \{i, 1, 8\}];$

```
(*************************************************)
```

$\text{VibrationalEnergyMorse}[v\_] = \text{Table}[$

$\text{VibrationalEnergys}[v\_] = \text{Function}[v, \omega_e[[i]](0.5 + v) -$
$\omega\chi_e[[i]](0.5 + v)^2 + T_e[[i]]][v]$

$, \{i, 1, 8\}];$

```
(*************************************************)
```

$\text{PotentialCurveMorse}[r\_] = \text{Table}[$

$D_e = \text{De}_{eV}[[i]]\text{eVtoCm1};$

$\beta = \left(\omega_e[[i]]\sqrt{\frac{2\pi^2 c\mu}{hD_e}}\right) 10^{-9};$

$\text{PotentialCurves}[r\_] = \text{Function}\left[r, T_e[[i]] + D_e\left(1 - e^{-\beta(r-r_e[[i]])}\right)^2\right][r]$

$, \{i, 1, 8\}];$

```
(*********************Harmonic****** * ***************)
```

```
WaveFuntionHarmonic = Table [α = (4π²cω_e[[i]] μ)/h 10^(-18);
WaveFuntions[r_, v_] = Function[{r, v},
1/√(2^v v!) (α/π)^(1/4) e^(-1/2 α(r−r_e)²) HermiteH [v, √α (r − r_e)]] [r, v],
{i, 1, 8}];
(****************************************************)
VibrationalEnergyHarmonic[v_] = Table[
VibrationalEnergys[v_] = Function [v, ω_e[[i]](0.5 + v) + T_e[[i]]] [v], {i, 1, 8}] ;

(****************************************************)
PotentialCurveHarmonic[r_] = Table[
D_e = De_eV[[i]]eVtoCm1;
β = (ω_e[[i]]√(2π²cμ/hD_e)) 10^(-9);

k = 2β²D_e;

PotentialCurves[r_] = Function [r, T_e[[i]] + 1/2 k (r − r_e[[i]]) ²] [r], {i, 1, 8}] ;

(*FCF, r − centroidandvibrationalenergycalculationsforMorse*)
Table[
NameFrom[[j]]NameTo[[i]]==
MatrixForm[
Table[

{ScientificForm[(NIntegrate[WaveFuntionMorse[r, k][[j]]
WaveFuntionMorse[r, l][[i]], {r, 0, 5.0},
Method → "GaussBerntsenEspelidRule"])^2],

ScientificForm[(NIntegrate[WaveFuntionMorse[r, k][[j]]r
WaveFuntionMorse[r, l][[i]], {r, 0, 5.0},
Method → "GaussBerntsenEspelidRule"]/
(NIntegrate[WaveFuntionMorse[r, k][[j]]
*WaveFuntionMorse[r, l][[i]], {r, 0, 5.0},
Method → "GaussBerntsenEspelidRule"]))],

Abs[VibrationalEnergyMorse[k][[j]]−
VibrationalEnergyMorse[l][[i]]]}, {k, 0, 15}, {l, 0, 15}]],
{i, 1, 7}, {j, i + 1, 8}]


(* Plots for Morse *)
VibrationalLevels = 12;
LowerLimits = {0.9, 1.08, 1, 0.98, 1.1, 1.1, 1.1, 1.1};
UpperLimets = {1.5, 1.87, 1.82, 1.7, 1.93, 2, 2, 2};

WaveFuntionPlot = Table[
```

```
Plot[{Evaluate[{WaveFuntionMorse[r, v][[i]]200+
VibrationalEnergyMorse[v][[i]],
VibrationalEnergyMorse[v][[i]]}/.v → Range[0, VibrationalLevels]],
Evaluate[{VibrationalEnergyMorse[v][[i]]}
/.v → Range[0, VibrationalLevels]]},
{r, LowerLimits[[i]], UpperLimets[[i]]},
Filling->Table[n → {n + (VibrationalLevels + 1)},
{n, 1, VibrationalLevels + 2}]], {i, 1, 8}];

PotentialPlot = Table[Plot[PotentialCurveMorse[r][[i]],
{r, LowerLimits[[i]] + 0.02, UpperLimets[[i]]},
AxesOrigin → {0.9, 0}], {i, 1, 8}];

Show[WaveFuntionPlot, PotentialPlot, PlotRange → {{0.5, 2}, {0, 70000}}]


(********************* ∗ FCF : HarmonicandMorse*********************)
Table[
NameFrom[[j]]NameTo[[i]] ==
MatrixForm[
Table[{ScientificForm[(NIntegrate[WaveFuntionMorse[r, k][[j]]
WaveFuntionHarmonic[r, l][[i]], {r, 0, 5.0},
Method → "GaussBerntsenEspelidRule"])^2]}, {k, 0, 15}, {l, 0, 15}]],
{i, 1, 8}, {j, 1, 8}]

(******************* ∗ Plot : HarmonicandMorse*******************)
PotentialPlotHarmonic = Table[Plot[PotentialCurveHarmonic[r][[i]],
{r, LowerLimits[[i]] + 0.02, UpperLimets[[i]]},
AxesOrigin → {0.9, 0}, PlotStyle → {Red}], {i, 1, 8}];
Show[PotentialPlotHarmonic, PotentialPlot,
PlotRange → {{0.5, 2}, {0, 70000}}]
```

List of References

[1] Krupenie, P.H.: *The Band Spectrum of Carbon Monoxide*. No. no. 5 in NSRDS-NBS. U.S. Department of Commerce, National Bureau of Standards, 1966.

[2] Velichko, T.I., Mikhailenko, S.N. and Tashkun, S.A.: Global Multi-isotopologue fit of measured rotation and vibration-rotation line positions of CO in $X^1\Sigma^+$ state and new set of mass-independent Dunham coefficients. *Journal of Quantitative Spectroscopy and Radiative Transfer*, vol. 113, no. 13, pp. 1643–1655, September 2012. ISSN 00224073.
Available at: http://linkinghub.elsevier.com/retrieve/pii/ S0022407312002294

[3] Farrenq, R., Guelachvili, G., Sauval, A.J., Grevesse, N. and Farmer, C.B.: Improved Dunham coefficients for CO from infrared solar lines of high rotational excitation. *Journal of Molecular Spectroscopy*, vol. 149, no. 2, pp. 375 – 390, 1991. ISSN 0022-2852.
Available at: http://www.sciencedirect.com/science/article/pii/ 002228529190293J

[4] Nicholls, R.W.: Laboratory astrophysics. *Journal of Quantitative Spectroscopy and Radiative Transfer*, vol. 2, no. 4, pp. 433 – 449, 1962. ISSN 0022-4073.
Available at: http://www.sciencedirect.com/science/article/pii/ 0022407362900304

[5] Majedifar, H. and Islampour, R.: Calculation of Franck-Condon Factors for a Number of Band Systems of Diatomic Molecules Using Hua Potential. *Iran. J. Chem. Chem. Eng.*, vol. 31, no. 2, pp. 25–35, 2012.
Available at: http://www.ijcce.ac.ir/article_5986.html

[6] Matsumoto, A. and Iwamoto, K.: Analytical formula for Franck-Condon factors involving the Morse potential. *Journal of Quantitative Spectroscopy and Radiative Transfer*, vol. 50, no. 1, pp. 103 – 109, 1993. ISSN 0022-4073.
Available at: http://www.sciencedirect.com/science/article/pii/ 0022407393901333

[7] DeLeon, R.L.: CO (A-X) electric dipole transition moment. *The Journal of Chemical Physics*, vol. 91, no. 9, pp. 5859–5860, 1989.
Available at: http://dx.doi.org/10.1063/1.455507

110

[8] Field, R.W., Benoist d'Azy, O., Lavollëe, M., Lopez-Delgado, R. and Tramer, A.: Radiative decay rates from deperturbed v=0-7 vibrational levels of CO measured using synchrotron radiation. *The Journal of Chemical Physics*, vol. 78, no. 6, pp. 2838–2846, 1983.
Available at: `http://dx.doi.org/10.1063/1.445271`

[9] Thorlabs: Magnesium Fluoride Plano-Convex Lenses.
Available at: `https://www.thorlabs.com/newgrouppage9.cfm?objectgroup_id=901&pn=LA6007`

[10] Huber, K.P. and Herzberg, G.: *Molecular Spectra and Molecular Structure, IV. Constants of Diatomic Molecules.* Van Nostrand Reinhold Company, 1979.

[11] Niu, M.L., Salumbides, E.J., Heays, A.N., de Oliveira, N., Field, R.W. and Ubachs, W.: Spectroscopy and perturbation analysis of the CO $A^1\Pi$-$X^1\Sigma^+$ (2,0), (3,0) and (4,0) bands. *Molecular Physics*, vol. 114, no. 5, pp. 627–636, 2016.
Available at: `http://dx.doi.org/10.1080/00268976.2015.1108472`

[12] Eidelsberg, M. and Rostas, F.: An Atlas of the Intersystem Transitions of CO. *The Astrophysical Journal Supplement Series*, vol. 145, no. 1, p. 89, 2003.
Available at: `http://stacks.iop.org/0067-0049/145/i=1/a=89`

[13] Dodge, M.J.: Refractive properties of magnesium fluoride. *Appl. Opt.*, vol. 23, no. 12, pp. 1980–1985, Jun 1984.
Available at: `http://ao.osa.org/abstract.cfm?URI=ao-23-12-1980`

[14] Morton, D.C. and Noreau, L.: A compilation of electronic transitions in the CO molecule and the interpretation of some puzzling interstellar absorption features. *The astrophysical journal supplement series*, vol. 95, pp. 301–343, 1994.

[15] Du Plessis, A., Rohwer, E.G. and Steenkamp, C.M.: Investigation of four carbon monoxide isotopomers in natural abundance by laser-induced fluorescence in a supersonic jet. *Journal of Molecular Spectroscopy*, vol. 243, no. 2, pp. 124 – 133, 2007. ISSN 0022-2852. PRAHA2006, The 19th International Conference on High Resolution Molecular Spectroscopy.
Available at: `http://www.sciencedirect.com/science/article/pii/S0022285207000264`

[16] Dickenson, G.D., Nortje, A.C., Steenkamp, C.M., Rohwer, E.G. and du Plessis, A.: Accurate Laboratory Wavelengths of the $e^3\Sigma^{-1}(v' = 5) - X^1\Sigma^+(v'' = 0)$ Band of $^{12}C^{16}O$. *The Astrophysical Journal Letters*, vol. 714, no. 2, p. L268, 2010.
Available at: `http://stacks.iop.org/2041-8205/714/i=2/a=L268`

[17] Du Plessis, A., Rohwer, E.G. and Steenkamp, C.M.: Accurate Laboratory Wavelengths of the $A^1\Pi(v' = 0 - 5) - X^1\Sigma^+(v'' = 0)$ Vibronic Bands of $^{12}C^{17}O$ and $^{12}C^{18}O$. *The Astrophysical Journal Supplement Series*, vol. 165, no. 1, p. 432, 2006.
Available at: `http://stacks.iop.org/0067-0049/165/i=1/a=432`

[18] Steinmann, C.M., du Plessis, A. and Rohwer, E.G.: High-resolution vacuum ultraviolet laser spectroscopy of molecules in a free supersonic jet : in search of rare CO isotopomers and CO-Ar van der Waals molecules. *South African Journal of Science*, vol. 101, no. 1-2, pp. 87–88, 2005.
Available at: `http://journals.co.za/content/sajsci/101/1-2/EJC96347`

[19] Dickenson, G.D.: *Development of a Tuneable Laser Source in the Vacuum Ultraviolet and its Applications to Spectroscopy.* Master's thesis, Stellenbosch University, 2008.
Available at: `http://hdl.handle.net/10019.1/1827`

[20] Boyd, R.W.: *Nonlinear Optics.* Academic Press, 2007.

[21] Nortje, A.C.: *Development and application of tunable VUV laser sources.* Master's thesis, Stellenbosch University, 2013.
Available at: `http://hdl.handle.net/10019.1/80302`

[22] Steenkamp, D.C.M.: Nonlinear Optics, February 2013. Lecture Notes for Honours in Nonlinear Optics course (Unpublished).

[23] Steinmann, C.M.: *Vacuum ultraviolet laser spectroscopy of CO molecules in a supersonic jet.* Ph.D. thesis, University of Stellenbosch, 2003.
Available at: `http://hdl.handle.net/10019.1/53709`

[24] Du Plessis, A.: *Laser Spectroscopy of the Fourth Positive System of Carbon Monoxide Isotopomers.* Ph.D. thesis, University of Stellenbosch, 2006.
Available at: `http://hdl.handle.net/10019.1/1219`

[25] Bitto, H., Chen, I. and Moore, C.B.: Rotational state distribution of CO photofragments from triplet ketene. *The Journal of Chemical Physics*, vol. 85, no. 9, pp. 5101–5106, 1986.
Available at: `http://scitation.aip.org/content/aip/journal/jcp/85/9/10.1063/1.451702`

[26] Dong, S.: *Factorization Method in Quantum Mechanics*, vol. 150 of *The Fundamental Theories of Physics.* Springer, 2007.

[27] Herzberg, G.: *Molecular Spectra and Molecular Structure, I. Diatomic Molecules.* No. v. 1 in Prentice-Hall physics series. D. van Nostrand company, inc., 1939.

[28] Dunham, J.L.: The Energy Levels of a Rotating Vibrator. *Physical Review*, vol. 41, pp. 721–731, 1932.
Available at: `https://doi.org/10.1103/PhysRev.41.721`

[29] Fraser, P.A.: A method of determining the electronic transition moment for diatomic molecules. *Canadian Journal of Physics*, vol. 32, pp. 515–521, 1954.
Available at: `http://dx.doi.org/10.1139/p54-054`

[30] Noda, C. and Zare, R.N.: Relation between classical and Quantum formulations of the Franck-Condon Principle: The generailzed r-Centroid approximation. *Journal of molecular spectroscopy*, vol. 95, pp. 254–270, 1982.
Available at: http://dx.doi.org/10.1016/0022-2852(82)90126-6

[31] Koperski, J. and Fry, E.S.: Molecules in the cold environment of a supersonic free-jet beam: from spectroscopy of neutral-neutral interactions to a test of Bell's inequality. *Journal of Physics B: Atomic, Molecular and Optical Physics*, vol. 39, no. 19, p. S1125, 2006.
Available at: http://stacks.iop.org/0953-4075/39/i=19/a=S22

[32] Lubman, D.M., Rettner, C.T. and Zare, R.N.: How isolated are molecules in a molecular beam? *The Journal of Physical Chemistry*, vol. 86, pp. 1129–1135, 1982.
Available at: http://dx.doi.org/10.1021/j100396a017

[33] Kudryavtsev, Y., Ferrer, R., Huyse, M., den Bergh, P.V. and Van Duppen, P.: The in-gas-jet laser ion source: Resonance ionization spectroscopy of radioactive atoms in supersonic gas jets. *Nuclear Instruments and Methods in Physics Research Section B: Beam Interactions with Materials and Atoms*, vol. 297, pp. 7–22, 2013. ISSN 0168-583X.
Available at: http://www.sciencedirect.com/science/article/pii/S0168583X12007525

[34] McGrath: McPherson 218 vacuum UV monochromator. November 2013.
Available at: http://www.emcgrath.com/catalog/images/LAB/Instruments/LBH097-2.jpg

[35] Bruyn, A.D.: Automation, characterisation and application of a monochromator for UV and Vacuum UV. Honours Research project (unpublished), 2014.

[36] Ashworth, S.H. and Brown, J.M.: An Atlas of Optogalvanic Transitions in Neon. Report ral-91-069, Rutherford Appleton Laboratory, 1991.

[37] Malitson, I.H.: Interspecimen Comparison of the Refractive Index of Fused Silica. *J. Opt. Soc. Am.*, vol. 55, no. 10, pp. 1205–1209, Oct 1965.
Available at: http://www.osapublishing.org/abstract.cfm?URI=josa-55-10-1205

[38] Herzberg, G. and Hugo, T.J.: Forbidden transitions in diatomic molecules: IV. The $a'^3\Sigma^+ \leftarrow X^1\Sigma^+$ and $e^3\Sigma^- \leftarrow X^1\Sigma^+$ absorption bands of carbon monoxide. *Canadian Journal of Physics*, vol. 33, no. 12, pp. 757–772, 1955.
Available at: http://dx.doi.org/10.1139/p55-091

[39] Smalley, R.E., Levy, D.H. and Wharton, L.: The fluorescence excitation spectrum of the HeI_2 van der Waals complex. *The Journal of Chemical Physics*, vol. 64, no. 8, pp. 3266–3276, 1976.
Available at: http://scitation.aip.org/content/aip/journal/jcp/64/8/10.1063/1.432667

[40] Du Plessis, A., Rohwer, E.G. and Steenkamp, C.M.: Investigation of four carbon monoxide isotopomers in natural abundance by laser-induced fluorescence in a supersonic jet. *Journal of Molecular Spectroscopy*, vol. 243, pp. 124–133, 2007. ISSN 00222852.
Available at: http://dx.doi.org/10.1016/j.jms.2007.01.009